

MINIMAL MODELS IN CARDIAC DYNAMICS

A Dissertation
Presented to
The Academic Faculty

By

Diandian Chen

In Partial Fulfillment
of the Requirements for the Degree
Doctor of Philosophy in the
School of Physics

Georgia Institute of Technology

August 2019

Copyright © Diandian Chen 2019

MINIMAL MODELS IN CARDIAC DYNAMICS

Approved by:

Professor Flavio H. Fenton, Advisor
School of Physics
Georgia Institute of Technology

Professor Roman Grigoriev
School of Physics
Georgia Institute of Technology

Professor Kurt Wiesenfeld
School of Physics
Georgia Institute of Technology

Dr. Richard A. Gray
Center for Device and Radiological
Health
Food and Drug Administration

Professor Yohannes Shiferaw
School of Physics
California State University

Date Approved: March 25, 2019

Of all things, I liked books best.

Nikola Tesla

This thesis is dedicated to my family, grandparents, extended family and best friends. It was impossible without you.

ACKNOWLEDGEMENTS

First and foremost, I would like to thank my advisor Professor Flavio H. Fenton for his support, guidance, and warmth. I have matured quite a bit in this journey and he has played a role in my growth. I would also like to thank Dr. Richard Gray of the FDA, Professor Yohannes Shiferaw, and Professor Roman Grigoriev for working with and most of all teaching me throughout the years. Thank you for your patience and generosity. I would also like to thank Professor Kurt Wiesenfeld for being part of my thesis committee as well. Thank you all for your time. A further thanks to my lab colleagues, especially Yanyan Ji and Andrea Welsh. It has been a long journey, but it was a privilege to see all of us grow. Lastly but most of all, I would like to thank my family and friends. Their support meant the world to me and I would not be here without them.

TABLE OF CONTENTS

Acknowledgments	v
List of Figures	xi
Chapter 1: Introduction and Motivation	1
1.1 Chapter I: Introduction to the Heart	2
1.1.1 Important properties	6
1.1.2 Modeling the Electrical System	8
1.1.3 Instability of the Electrical System	12
1.1.4 Abnormal Pulse Formation	12
1.1.5 Reentry	14
1.1.6 Alternans to Arrhythmia	15
1.2 Some open Questions in Cardiac Research	18
1.2.1 Phenomenological vs. Complex Models	18
1.2.2 APD Alternans	19
1.2.3 Spiral Waves as a Path to Arrhythmia	19
1.2.4 Calcium Alternans	20
1.3 Acronyms	22
Chapter 2: Action Potential Amplitude Alternans	23

2.1	Minimal Model for APA Alternans	24
2.1.1	Formulation of Model	24
2.1.2	Derivation of the APA Map	27
2.1.3	Confirmation of the Stability Condition Through Numerical Analysis	30
2.1.4	Physiological Connection with Parameters	32
2.2	Discussion	33
Chapter 3: Take-Off Potential		35
3.1	Cause of Low TOP	36
3.2	Time constant adjustment	37
3.3	Discussion	41
Chapter 4: Excito-Oscillatory Behavior		43
4.1	Experimental Evidence	44
4.2	Model in Tissue Simulations	45
4.3	Model Equations	47
4.4	Phase Space Analysis of Excito-Oscillatory behavior	48
4.4.1	Ubiquity of 3 fixed points and Excito-Oscillatory behavior	50
4.5	Elevated Take-off Potential	51
4.6	Tail-ignition	53
4.7	Multistability	56
4.8	Chaotic Nature of our Model	59
4.8.1	Homoclinic Tangle	59
4.9	Solutions in a Traveling Wave	62

4.9.1	Hopf Bifurcation of Traveling Wave Solution	64
4.10	Future Work	67
4.11	Applications to Ohara-Rudy Human Ventricular Model	68
4.12	Discussion	69
Chapter 5:	Calcium Alternans	70
5.1	Calcium Release Unit and Calcium Cycling	71
5.1.1	Calcium Sparks	73
5.2	3 Important Properties for Calcium Alternans	74
5.2.1	Randomness	74
5.2.2	Recruitment	74
5.2.3	CRU Refractoriness	75
5.3	Mechanisms of Calcium Alternans	75
5.3.1	Release-Load Mechanism of alternans	75
5.3.2	Calcium Release Unit Refractoriness	77
5.3.3	Bidirectional Coupling	78
5.4	Calcium Modeling	79
5.4.1	Luo-Rudy model	80
5.4.2	The Shiferaw model	80
5.4.3	The Nivala model	81
5.4.4	Minimal Model of Calcium Alternans	82
5.4.5	Model Equations	83
5.5	Variables	85

5.5.1	C_{cyto} [uM/L]	85
5.5.2	C_{sr} [uM/L][v_{sr}/v_{cyto}]	85
5.5.3	r [dimensionless]	85
5.5.4	q [dimensionless]	86
5.5.5	n [dimensionless]	88
5.5.6	f gate [dimensionless]	89
5.6	Derivations of equations	89
5.6.1	Currents	89
5.6.2	Release current	89
5.6.3	Uptake current	89
5.6.4	Sodium Calcium Exchanger	90
5.6.5	L-Type Calcium current	93
5.7	Results	95
5.7.1	Alternans from Q	96
5.7.2	Alternans from R	100
5.7.3	Driven Alternans from Bidirectional Coupling	105
5.7.4	Application to Experimental Data	107
5.8	Limitations	114
5.8.1	Spark Lifetime	115
5.8.2	Buffers	115
5.8.3	Total calcium variation	115
5.8.4	Contraction	115
5.8.5	Reduction in Compartmentalization	116

5.9 Customization of Calcium Modeling	117
Chapter 6: Conclusion	118
6.1 Action Potential Amplitude Alternans	118
6.2 Take-off Potential	119
6.3 Excito-Oscillatory Behavior	119
6.4 Minimal Calcium Alternans Model	120
6.5 Limitations	120
6.6 Future Work	121
Appendix A: Contributions in Experiment and Simulations	123
Appendix B: Numerical Methods and Simulations	124
Appendix C: Poincaré section analysis	131
Appendix D: Chapter 5: Calcium model parameters	133
D.1 alternans from Q	133
D.2 alternans from R	135
D.3 alternans for cat atrium	136
D.4 alternans rabbit ventricles	138
References	148

LIST OF FIGURES

1.1	Figure shows a schematic diagram of the human heart and its electrical conduction system. Regular stimulus originates from the Sino-Atrial(SA node, then propagates to the ventricles through the AV node [7].	2
1.2	Top image: A schematic diagram of an action potential with all 4 phases and the active currents in each phase. Middle panel: this section plots the currents that affect the action potential shape in time series. In ward currents increase the voltage, and outward currents decrease the voltage. Bottom image: A typical ECG signal for a beat, where P wave is the excitation of atria, QRS is the wavefront across the ventricles, and the T wave is the repolarization of the ventricles.[8]	4
1.3	Image plots an example, scaled diagram of the action potential(black), calcium transient release(red) and contraction(dashed lines) in time series[13]. Note the time difference in calcium release and onset of AP	6
1.4	Schematic diagram of cable theory and the currents in the cable theory, $I(x)$ and I_m , the axial and transmembrane currents.	9
1.5	Schematic diagram of the cable theory resistors and capacitors, where c_m and c_m are the membrane parameters and r_l is the axial resistance.	9
1.6	A summary diagram of the basic pathways towards arrhythmia[19]. Reentry and abnormal pulse form the two main mechanisms, with multiple causes leading to each.	12
1.7	[22]Image shows examples of the early-afterdepolarizations(EAD) and Delayed afterdepolarizations(DADs) in a cardiomyocyte action potential time series.EADs are extra excitations in phase 2 or phase 3 of the action potential, and DADs are excitations during early phase 4.	13
1.8	Image captures a snapshot of a simulation of cardiac tissue demonstrating a typical spiral wave on the left panel. Orange is areas of depolarization while black are areas of rest. On the right, the spiral wave breakup and tissue enters chaos[23]	14

1.9	Image demonstrates an example of an accessory pathway for excitation that leads to reentry. This syndrome is termed the Wolfe-Parkinson-White syndrome, where an extraneous connection between the ventricles and atria exists[28]. As a result, the excitation in the ventricles return to the atria through the accessory pathway and re-excites the tissue	15
1.10	[32]The top image shows the definitions of the APD and DI according a period, or PCL. The bottom image is the APD return map for two different types of behaviors depending on the slope of the APD restitution function of DI. If the slope is greater than 1, then the system will have alternans(right). If not, the system will have a steady value of APD and DI(left)	17
1.11	[33]Image demonstrating a cardiac tissue simulation showing spatially discordant alternans. In certain areas the cellular action potential signal, shown in the right, alternans long short, and in other areas alternates short long. This causes a gradient of behavior, show in the left, such that if an ectopic beat at b occurred, it would propagate laterally, then curl in causing reentry.	18
1.12	Image depicts a snapshot of our laboratory's experimental rabbit ventricle data during VF. The yellow spots indicate excitation, while blue indicates rest. Most notably, there are not many distinct spiral wave branches.	20
2.1	Top panel plots experimental rabbit APD alternans in time series. Middle panel show rabbit ventricles in VF with distinct amplitude alternans. Bottom panel is the Fenton-Karma model in time series showing VF in tissue simulations[40] In these plots, data in time series demonstrates that APD alternans can be stable and that amplitude alternans are more correlated to VF.	23
2.2	Image shows a typical signal from our two variable model. The x axis is time in milliseconds, and the y axis is voltage in time series(solid line) and h gate value(dotted line, scaled). This signal is demonstrating APA alternation due to the h gate alternating[40].	26
2.3	Figure visualizes the three important relationships we extracted from observations of the 2 variable model: h gate and DI, h gate and amplitude, and amplitude and APD[40].Top image shows that the h gate value at the end of a beat is proportional to the DI, the second image shows that the amplitude of a beat is proportional to the h h gate value of the previous beat, and the last bottom image shows that the APD and APA are directly related.	27

2.4	Top: Amplitude versus h gate restitution curve and period curves, solid and dashed line respectively, for five different periods (320,340,360,380, and 400 ms). Bottom: A cobweb diagram for a period with a stable fixed point (450ms dashed) and for a period with alternans (368ms solid line)[40]. . . .	30
2.5	Image demonstrates the S1S2 pacing protocol[29]. The S1 is the first beat shown in the plot, and the S2 are the following beats. Depending on the timing of the second action potential, the S2 beat's shape and amplitude will vary. The longer the DI after the S1, the larger the APA and APD of the S2	31
2.6	A pseudo-ECG of our model in cable when amplitude alternans occur[40]. ECG shows distinct QRS alternans.	34
3.1	[50]Image shows Fenton-Karma four variable model in VF in top panel and experimental data showing VF in the bottom panel. A distinct difference is the lack of variation in the model's take off potential even during VF. The FK model is fit to experimental restitution curves and matches in frequency to the VF time series, but shows qualitatively unrealistic VF due to the variation in TOP	36
3.2	[50]Time constants functions for the j gate of Noble and BR model. Solid lines are the original time constant values with a dependence on voltage. Dashed lines are the shifted time constant functions fitted with modified equations.	38
3.3	Plot demonstrates the sodium current response as a function of time. The peak of the j gate time constant is shifted and the resulting sodium response are plotted in time against the original sodium response in black[50]. Image demonstrates that the modified time constant equations can increase the sodium response to allow the system to fire earlier in time	39
3.4	Image depicting comparison of modified Noble model with the original Noble model. Left panel is original, right panel is the modified result with an elevation of 11.5mV in TOP[50].	40
3.5	Image comparison of modified BR model. Red time series line is modified BR model and dashed black line is original BR model. Modifications results in 14mV elevation in TOP[50].	40
3.6	[50]Modified Noble model with j gate of time constant shifted. Initially paced at 500ms and then rapidly paced at 60ms to mimic VF, the take off potential is raised significantly indicating our success in raising TOP. . . .	41

4.1	Tissue simulation of our bubbly model with 500x500 grid size time integrated 2000ms. Tissue is initially paced from left bottom corner at 99.5ms.	43
4.2	Top left image: spiral wave breakup in a tissue simulation[54]. Top right image: the bubbly model in a tissue simulation. Bottom image: experimental rabbit ventricle data showing more bubble-like oscillations than distinct spiral wavelets.	44
4.3	Progression of our bubbly model from steady state to chaos. Top left image: tissue is paced steadily from corner. Bottom left image: a wave ignites in the backwards direction, covering site of stimulus. Top right: subsequent waves eventually ignite forward and backward covering the tissue in curved stripes. Bottom right image: eventually stripes curve and round out, and bubble-like oscillations occur.	45
4.4	Image of our model with recording at a site in tissue simulation recorded in time series. TOP varies significantly and the time series is chaotic.	46
4.5	Phase space plot of a trajectory of our model from a signal from a location in tissue simulation. Y axis is h gate variable, and the x axis is voltage variable. System shows small amplitude and large amplitude oscillations. .	47
4.6	Image of the phase space and nullclines of our model, h gate versus voltage. The black line is the voltage equation nullcline, and the purple line is the h gate nullcline. The points circled in green are the fixed points of the system, including a stable rest, saddle, and unstable oscillatory fixed point.	49
4.7	The trajectory of the system when initialized near the unstable oscillatory fixed point. This trajectory occurs with no stimulus, and it proceeds to recover, then self-excite once.	49
4.8	Tissue simulation of the Gray-Scott model with specific set of parameters. Dynamics show similar qualities to our bubbly model[59]. Simulations begins with an excitation from the left bottom corner	51
4.9	[50]An image showing Fenton-Karma four variable model in VF in above panel and experimental data showing VF in the bottom panel. A distinct difference is the lack of variation in the model's take off potential even during VF.	52
4.10	Top panel: left image is of tissue simulation of BR model in VF, right image is the electrical signal recorded at a site showing low take-off potential. Right image is of Ten-Tusscher tissue simulation in VF, the electrical signal is recorded at a site and shows low take off potential.	52

4.11	Solid line is the voltage and dashed line is the slow variable in FN model when simulated in tissue and undergoing chaos. The nullclines adjusted such that 3 fixed points exists[60].	53
4.12	Our model in cable form with the x axis as position and y axis as voltage and h variable scaled. Image shows the conditions before tail-ignition. The focus is on the position between 100 and 500.	54
4.13	Our model in cable form with the x axis as position and y axis as voltage and h variable scaled. Image shows the conditions 10 ms after tail-ignition. The voltage signal between position 10 and 500 fires without a pacing stimulus.	54
4.14	Image shows time snapshots of the Gray-Scott model paced in with a steady rate from corner. Initial pulse propagates[59], After initial pulse propagates, the waveback tail-ignites, similar to bubbly model[59].	55
4.15	Initial condition of our cable, where the two variables are assymmetrically profiled, thus resulting in chaotic solutions in the cable. This style of initial conditions is the same style of initial conditions as Cytrynbaum et.al.[61].	56
4.16	Time progression plot of the our model in cable form with the Cytrybaum initial conditions. Yellow lines indicate the voltage value at cable position. At the first time interval, the system produces two waves in opposite directions. In the second time interval, the wavebacks ignite, and by the third time interval chaos ensues.	57
4.17	Initial condition of our cable, where the two variables are more symmetrically profiled, thus resulting in steady action potential solutions in the cable. This style of initial conditions is the same style of initial conditions as Cytrynbaum et.al.[61].	58
4.18	Our model's time progression in a cable with the same parameter values as previous trial except with symmetrical initial conditions. At the first time interval two waves propagate into opposite directions and by the second interval, they are sufficiently apart and non-interacting . No wavebacks take place, and the solutions remain steady traveling waves.	58
4.19	Our model paced model at single cell with $T = 18\text{ms}$. The image shows the voltage values in time series. A notable characteristic is the varying TOP, chaotic behavior time, very similar to voltage time series recorded in tissue simulations.	59
4.20	Our model in single cell is paced at different periods. The resulting APD is plotted against the corresponding period. Model shows multiple regions where the APD value becomes chaotic.	60

4.21	Panel A and B: periodic orbits in our paced single cell system, at 18ms, found through Newton root search with the top being a 3 cycle and the bottom being a 1 cycle. Panel C: the periodic orbits plotted in phase space.	61
4.22	Poincaré section plot of a periodic orbit and its stable and unstable manifolds. Green arrow indicates the periodic orbit on the section, the magenta line is the stable manifold and black line is unstable manifold. Black arrow indicates a second periodic orbit on the Poincaré section.	62
4.23	Figure shows the voltage versus position plot of the calculated traveling wave solution. Cable has 3500 discrete units with $dx = 0.00125\text{cm}$	63
4.24	Figure shows the voltage time series of the calculated traveling wave solution with cable size at 3500 discrete units and $dt = 0.001\text{ms}$. Image demonstrates the stability of the solution in time. Solution form persists without instability.	64
4.25	Image visualizes the voltage versus position of the calculated solution. Cable size is 3400 discrete units at $dx = 0.00125\text{cm}$. Y axis is the voltage, and the x axis is the position.	65
4.26	Plot shows time series of the action potential of a location in the cable with domain size 3400. $Dx = 0.00125\text{cm}$, $dt = 0.001\text{ms}$ Pulse evolves from stable traveling wave to a relative periodic orbit.	66
4.27	Image is of a schematic bifurcation diagram of the spatial solutions of our model in a cable form. Y axis is the velocity of a solution, and x axis the inverse of the length. Initially at relatively larger cable lengths, the solution is a pair of traveling waves. After the cable lengths decrease to a certain threshold, the traveling solution becomes unstable and evolves into an RPO.	67
4.28	Image shows a progression in time of the O'hara-Rudy model of human ventricles with I_{kr} current at 78 percent of full magnitude. The progression of the model in tissue from left to right echoes similar characteristics as our model, the tail propagation and bubbles like oscillations[36]. The system is paced from the left bottom corner. Image 1 shows a wave that is moving in the forward direction towards the upper right hand corner. Image 2 shows the same wave firing in the reverse direction. Bottom panel is a signal recorded at site in tissue simulation. Data courtesy of Dr. Abouzar Kaboudian.	68

5.1	[62]Panel A is a detailed diagram of the contractile system in a cardiomyocyte, showing sections of the SR and T-tubules, alongside myofibrils that contract for the heart to pump blood. Panel B visualizes the T-tubules structure in a rat ventricle, showing the intricate and three dimensional structure. Panel C is a schematic diagram of the local calcium release unit. Panel D is an example time series of the action potential and calcium release amplitude, showing the approximate time scales for each event.	70
5.2	Illustration of spark phenomena through a line scan of a cardiomyocyte that is producing calcium sparks. Bright yellow and red spots represent these local excitations while the rest of the system is at rest [69].	73
5.3	Figure depicts the highly nonlinear release-load relationship that is a mechanism for calcium transient alternans. The y axis is the calcium transient amplitude and the x axis is the SR calcium load before the release. For a larger SR load, the following release current will be exponentially larger[45].	76
5.4	Experimental evidence from Diaz et. al. shows the relationship between cytoplasmic calcium release amplitude and SR load before large and small release beats. Before a large release, it has been shown that the load is large. On the other hand, before a small cytoplasmic calcium release, the SR load is measured to be small[45].	77
5.5	[73][78]Experimental data of SR calcium concentration demonstrating that alternans in calcium cycling can occur despite lack of alternans in the loading value before the next release. Y axis is SR calcium content, and x axis is time in seconds.	77
5.6	[79]An illustration of the bidirectional coupling between voltage and calcium systems. Voltage affects the calcium through the graded release mechanism. If the system has a longer DI, the L-type calcium current will be larger, the calcium release will be correspondingly increased. Calcium couples and influences the APD of voltage through the transmembrane calcium currents. If the calcium transient is large in amplitude, the L-type calcium current will be inactivated earlier calcium sensitive gates. On the other hand, if the calcium transient is large, the sodium calcium exchanger will remove a calcium ion for 3 sodium ions, which increases the inward current and thus the APD.	79
5.7	[62] A diagram of the markovian style of modeling in Nivala 2012. LCC variable(A) and RyR(B) transition between various states with certain rates. The k's indicate transition rates, while "C" and "O" indicate closed and open states for the gating variables.	81

5.8	Schematic diagram of our two compartment model. The two compartments are the sarcoplasmic reticulum(SR) and cytoplasm(CYTO). The currents that affect each compartment are also visualized above. Uptake and release contribute to the SR calcium concentration, and the L-type calcium current and Sodium calcium exchanger affect the cytoplasmic calcium transient concentration.	82
5.9	Plot demonstrating the steady state of the r gate variable, R_{∞} , versus C_{sr} for our model. At high SR content, the r gate has a higher probability of recovering to its resting values, indicating that a large portion of the CRUs are available to fire.	86
5.10	Plot visualizing the steady state of the q gate variable of our model and its dependence on the SR calcium concentration. The relationship is determined by 3 piecewise linear functions. This relationship is a major source of the nonlinear relationship between calcium release into the cytoplasm and SR load.	87
5.11	Equation 49 in plotted form. The value of equation versus voltage can be fitted with a line.	92
5.12	Comparison of sodium calcium exchanger current. Top: LR sodium calcium exchanger current and bottom: our models sodium calcium exchanger current[80].	92
5.13	Time series plot showing comparison of L-type calcium currents of the Shiferaw 2003 model and our minimal calcium model.[65] Top: Image of Shiferaw L-type calcium current. Bottom: Image of our simplified L-type calcium current. Both models' L-type calcium current has shark peaks and a small late current.	95
5.14	Image visualizes the clamped voltage waveform used in both scenarios of calcium alternans and no calcium alternans. Clamped waveform demonstrates that voltage does not contain the source of alternans and is not necessary for calcium transient to alternate independently.	96
5.15	Time series plot illustrating the r gate of the system in the previous two scenarios of both alternans and no alternans in cytoplasmic calcium concentration. The r gate recovers fully to the value of 1 before each beat, indicating that it is not the source of alternans.	97
5.16	Figure depicts the cytoplasmic calcium concentrations plotted in time series showing distinct alternans due to q gate steady state's nonlinear dependence on SR calcium concentration. For this scenario, both the peak and the end-diastolic calcium values alternate.	98

5.17	Image depicts the Q gate steady state relationship with SR calcium concentration. 3 piecewise functions contribute to the shape of the relationship. If the relationship is nonlinear, as shown in the image, the resulting calcium transient is capable of producing alternans.	98
5.18	Image depicts the Q gate steady state relationship with SR calcium concentration. 1 linear function determines the shape of the relationship. If the relationship is linear, as shown in the image, the resulting calcium transient is incapable of producing alternans.	99
5.19	Cytoplasmic calcium concentration plotted in time series. The calcium transient is not alternating, due to the manipulations in the q gate equations.	100
5.20	Cytoplasmic calcium concentration in time series, showing no alternans due to r gate dynamics.	101
5.21	R gate variable in the corresponding time series to figure 5.22 showing no alternans.	102
5.22	Cytoplasmic calcium concentration in time series showing alternans due to r gate dynamics. For this scenario, the peak of the cytoplasmic calcium concentration is alternating significantly, but the end-diastolic value is alternating relatively less.	103
5.23	R gate variable in time series showing distinct alternans, indicating that it is the cause of alternans. Figure corresponds to cytoplasmic calcium concentration plot in figure 5.22	103
5.24	Q gate variable in the corresponding time series to figure 5.22, showing relatively less variation in value before each beat than the r gate variable time series in figure 5.23	104
5.25	Image above depicts two different types of cytoplasmic calcium alternans in time series in two different animals, rabbit ventricle and cat atrium tissue. The resting calcium value after each beat varies in rabbit ventricle, but not in cat atrium, giving evidence of different sources for calcium alternans. . .	105
5.26	Figure plots the clamped action potential waveform in time series that is coupled to our minimal calcium model. The action potential is tuned to have alternans every other beat and in turn produces alternans in calcium transient.	106

5.27	Plot demonstrating the resulting cytoplasmic calcium concentration corresponding to 5.26. Y axis is cytoplasmic calcium concentration and x axis is time. The calcium system is tuned to be incapable of alternans independently, but the voltage system drives the calcium system to alternans nonetheless.	106
5.28	Laboratory experimental voltage and cytoplasmic calcium cat atrium time series. Voltage is in red in top panel and calcium is in green bottom panel. The voltage system is not visibly showing alternans, but the calcium transient is demonstrating alternans in peak amplitude.	107
5.29	Our model tuned to mimic experimental cat atrium data in figure 5.28. Top panel is voltage in red and bottom panel is cytoplasmic calcium concentration in green. Note, like the cat atrium data, the voltage system is not alternating visibly but the calcium transient is alternating in peak amplitude. The end-diastolic calcium level is not changing significantly.	108
5.30	Figures gives experimental laboratory data of rabbit ventricles showing simultaneous voltage and cytoplasmic calcium signals in time series. Red line is the voltage time series and Green line is the calcium time series. Calcium shows distinct alternans in both peak and end-diastolic values, while voltage shows relatively less alternans.	109
5.31	We plot the single cell paced system's voltage(red) and cytoplasmic calcium concentration(green) in time series. Voltage is clamped to a periodic action potential waveform, and cytoplasmic calcium persists in alternans mode due to q gate parameters.	110
5.32	Image gives plot in time series showing our model in single cell with the q gate manipulated such that the calcium cycling system produces alternans. Red line is voltage system in time series and green line is cytoplasmic calcium concentration in time series. Because we adjusted the steady state of the q gate such that dependence on the cytoplasmic calcium concentration is nonlinear, the resulting cytoplasmic calcium concentration and voltage system are both alternating.	111
5.33	Image gives plot in time series showing our model in single cell with the q gate rendering system incapable of alternans. Red line is voltage system in time series and green line is cytoplasmic calcium concentration in time series. Because we adjusted the steady state of the q gate such that dependence on the cytoplasmic calcium concentration is linear, the resulting cytoplasmic calcium concentration and voltage system are not alternating.	112

- 5.34 Image illustrates a time series plot, in single cell, of voltage signal in red and calcium transient in green. The cytoplasmic calcium system is clamped to a steady form and coupled to the voltage system. The result shows no alternans in the electrical system. 113
- 5.35 Image visualizes a plot of voltage time series before and after clamping the calcium cycling system. The green signal is the voltage system when the cytoplasmic calcium is clamped and is not alternating, and the red signal is the voltage system when cytoplasmic calcium is clamped. This comparison gives evidence to the fact that the calcium system is the source of instability. 114
- 5.36 Plot illustrates the sodium calcium exchanger current in time series from Shiferaw 2003 model due to the compartmentalization of spaces[65]. Because the concentration rise in the submembrane space is sharp and the sodium-calcium exchanger equation is dependent on its value, the shape of the resulting time series differs from our model. 116

SUMMARY

Cardiac Arrhythmia is a leading cause of death in the western industrialized world. To date, multiple pathways to examine and treat this disease exist. In this thesis, we focus on computational modeling and nonlinear analysis of cardiac dynamics. While a variety of cardiac models exist, we examine minimal models that produce phenomenological properties of cardiac dynamics. The usefulness of such models is that they are intuitively easy to understand and manipulated.

From our results, we first demonstrate the usefulness of minimal models by using a two variable model to produce a novel technique to predict the onset of instability. By reducing current models to a minimal version, we show through graphical and nonlinear methods that action potential amplitude alternans is of equal importance to action potential duration alternans. By further reduction of the two-variable model through fitting to simple equations, we show that phenomenological models can reproduce results that better fit experimental data. Moreover, not only can our constructed minimal model produce common phenomena, they can also demonstrate novel dynamics with the adjustment of a small group of parameters. To further expand the usefulness of minimal models, in the last chapter, I construct a minimal model of not only voltage but also the calcium cycling system. Overall, while mathematically complex models are useful and necessary, in this thesis, we present an alternative perspective to study arrhythmia.

CHAPTER 1

INTRODUCTION AND MOTIVATION

Sudden cardiac death(SCD) is the leading cause of natural death in the western world [1]. Claiming more than 300,000 lives per year, it constitutes half of all heart disease deaths[2]. Unlike heart attacks, which are known as myocardial infarction and is the loss of oxygenated blood to the heart tissue, SCD occurs when the electrical system of the heart malfunctions due to arrhythmia. Unfortunately, while in some cases victims has symptoms prior to SCD, many of the cases do not. Thus, it is of utmost importance to detect, target, and prevent cardiac electrical dysfunction.

SCD is preceded by untreated ventricular fibrillation, VF, in a significant portion of cases[3]. In a healthy human heart the electrical signal propagates in coordinated waves which produces coordinated contraction, while VF occurs when the electrical system is uncoordinated, which in turn results in uncoordinated contraction that if left untreated will lead to cardiac death within minutes. While advancement in this field has changed significantly in the past decades, the underlying mechanisms of VF are still poorly understood.

As a whole, arrhythmia is treated through multiple techniques such as drug therapies, implantable defibrillators, and ablation[4][5][6]. Correspondingly, mammalian experiments and computational models are also methods of understanding the underlying mechanisms that do not require invasive surgery on humans subjects. Alongside computational modeling, nonlinear dynamics analysis is used to probe and investigate the excitable nonlinear nature of the cardiac systems. In this thesis, we apply computational methods and nonlinear dynamics to construct and analyze minimal models of cardiac dynamics based on laboratory experimental data.

The outline of this thesis is as follows: In section I, we describe the state of current models and highlight important properties such as cable equation and mechanisms for ar-

rhythmia. In Section II, we introduced a novel framework to predict arrhythmia by examining the action potential amplitude(APA). In section III, we investigate a drawback in current cardiac models and propose a solution. In section IV, we introduce a minimal model with novel dynamics that provides an alternate route to fibrillation. In the last section, we construct a minimal model for the calcium system of the heart and fit to experimental data.

1.1 Chapter I: Introduction to the Heart

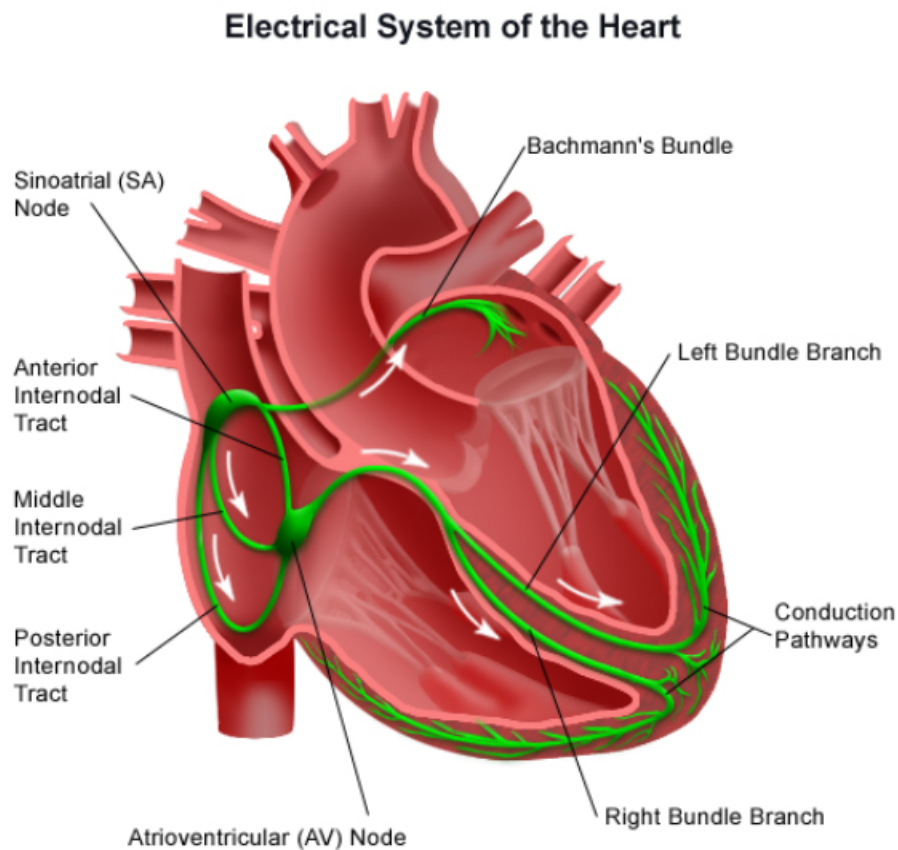


Figure 1.1: Figure shows a schematic diagram of the human heart and its electrical conduction system. Regular stimulus originates from the Sino-Atrial(SA node, then propagates to the ventricles through the AV node [7].

The human heart has four chambers, consisting of two atria and two ventricles, as shown in figure 1.1. In normal contraction conditions, the atria fill with blood, release it into the

ventricles, and then the ventricles pump the blood into the body. This cycle initiates with an electrical stimulus at the pacemaking site, the sinoatrial node(SA node), shown in the top left corner of the image 1.1. The signal spreads through the atria which elicits its contraction, then after a delay, to the AV node and to the purkinje fibers. The purkinje fibers are modified cardiomyocytes that conduct the electrical signal to the ventricles, which contracts and pump the blood into the body. This contraction stage is termed the systole, while the following rest stage is diastole. After systole, the muscles rest to recover its previous stage and prepare for the next contraction. As a whole structure, the heart's electrical signal is detected through the ECG. In the figure 1.2 in the bottom panel, we plot a typical ECG in a normal beating heart. The P wave marks the excitation of the atria, and the QRS wave corresponds to the ventricular excitation and contraction. The T-wave is the duration of ventricular repolarization. The time duration between the segments and the amplitudes can give insight to the observer about the major dysfunction of the heart.

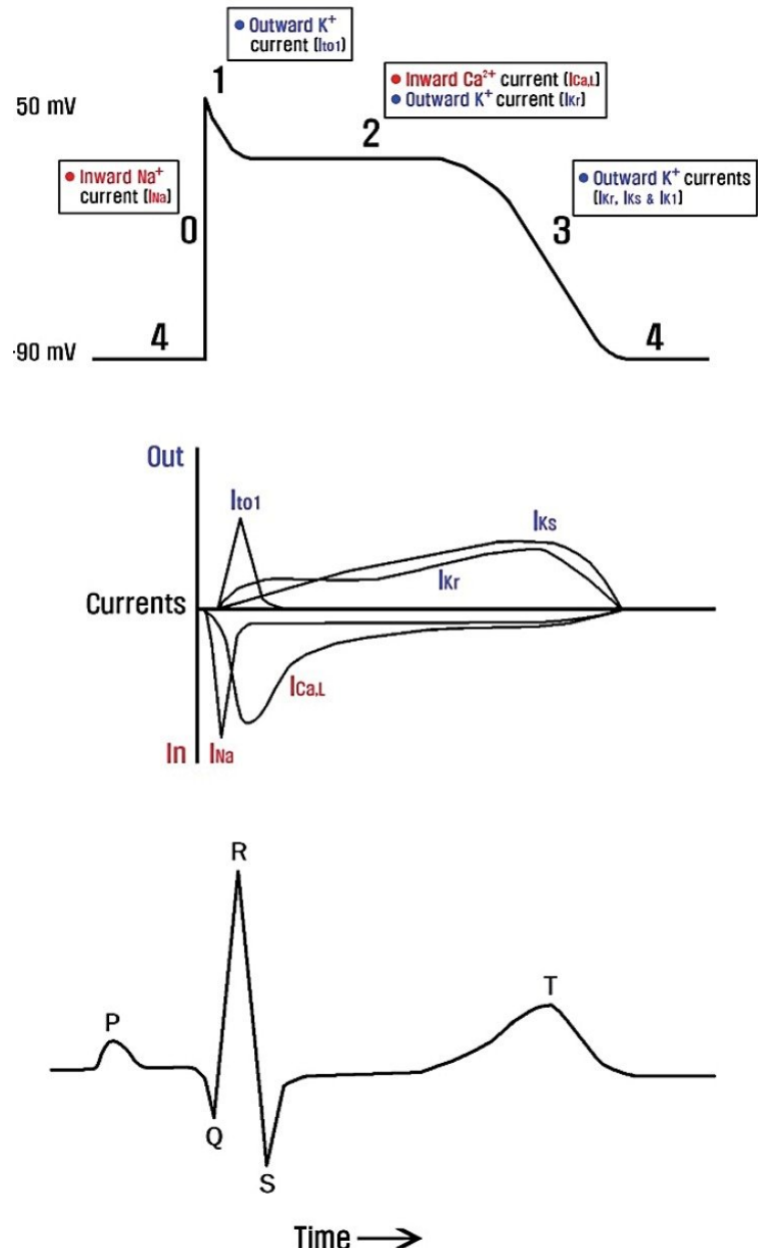


Figure 1.2: Top image: A schematic diagram of an action potential with all 4 phases and the active currents in each phase. Middle panel: this section plots the currents that affect the action potential shape in time series. In ward currents increase the voltage, and outward currents decrease the voltage. Bottom image: A typical ECG signal for a beat, where P wave is the excitation of atria, QRS is the wavefront across the ventricles, and the T wave is the repolarization of the ventricles.[8]

At the cellular level, or at the cardiac myocyte, each cell's electrical signal is termed the action potential(AP), shown in the figure 1.2. The action potential(AP) is a nonlinear

all-or-none electrical cellular response to an external stimulus. Normal myocytes are typically at rest, near -85mV [9]. Between the intracellular and extracellular medium, there is a difference of concentration in sodium, calcium, and potassium ions to allow for fast signaling. When the stimulus elevates the voltage to threshold, the inward fast current, sodium, sharply raises the AP to a high voltage[10].

The action potential, shown in the figure 1.2, has 4 distinct phases. Phase 4 is when the cell at resting potential and the heart is at diastole. Phase 0, lasting less than 2ms, is when stimulus current in a myocyte raises the potential such that the cell has a fast influx of mostly sodium. Phase 1 is when the potassium channels opens and sodium close. Phase 2 is when the slow current, most notably the calcium current enters and the outward flux of potassium balance out, defining this stage as the plateau. Next, in phase 3 the calcium current attenuates and the potassium returns the system's transmembrane voltage to rest in phase 4[11].

The contraction of the heart follow calcium release, which follows the action potential[12]. As the transmembrane voltage rise, the L-type transmembrane calcium current enters the cell, raising the internal calcium concentration. In ventricles, huge stores of calcium are induced to release by the L-type calcium current. This large gain in internal calcium activates the contractile machinery of the cardiomyocyte. In the figure 1.3, the timing of AP and contraction is shown. Unless under arrhythmogenic conditions, the heart will not spontaneously contract.

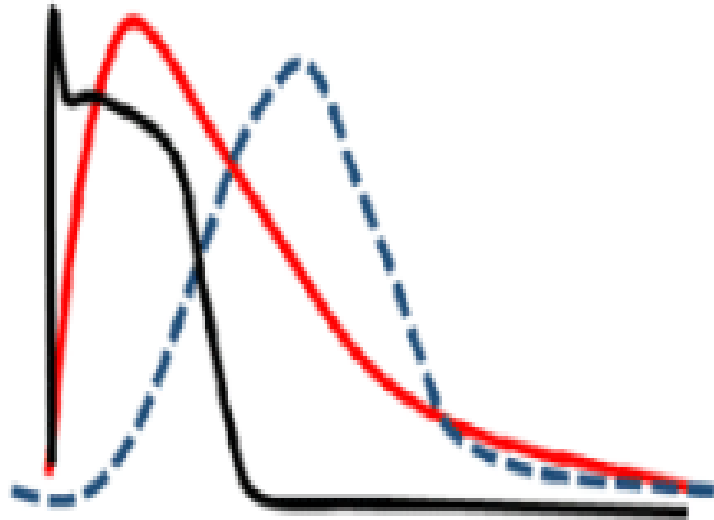


Figure 1.3: Image plots an example, scaled diagram of the action potential(black), calcium transient release(red) and contraction(dashed lines) in time series[13]. Note the time difference in calcium release and onset of AP

1.1.1 Important properties

All-or-none

The firing of the action potential is independent of amplitude of stimulus current, thus leading to the all-or-none terminology. Rather, the Action potential amplitude(APA) is dependent on the state of recovery of its ionic channels. The more the system has been allowed to recover, the larger the subsequent currents. If the stimulus is strong enough such that the inward currents is larger than the outward flux, the myocyte will fire with a sharper upstroke.

Conductivity

The heart is an excitable medium capable of conducting electrical signal to onset contraction. Each myocyte is connected to its neighbors through gap junctions, termed connexons, where ionic current is passed. A signal from a pacemaker site can spread and induce con-

traction if the source is strong enough[14].

Refractoriness

Subsequent to an excitation, cardiac myocytes enter an absolute refractory period, ARP, where an action potential is impossible to elicit. The subsequent period to the ARP is the relative refractory period, RRP, where excitation is possible if a stronger than usual stimulus is applied due to the partial recovery of the sodium channels. The refractory periods allow the system to rest and refill the atria with blood. In addition, refractory periods prevent the electrical wave from conduction in multiple directions.

Automaticity

Automaticity is the property in which a cardiac myocyte can spontaneously self excite. The Sino-atrial(SA) node of the heart contains this property. Latent pacemakers such as the atrioventricular(AV) node and purkinje fibers can self-excite, but under normal conditions are overdriven by the SA node[15].

Contractibility

Contractibility is the ability of a myocyte to contract after an action potential response. Action potentials precipitate calcium release in ventricular myocytes, which induces contraction. Acutely regulated coordination between the voltage and contraction is vital[12].

Nernst/Reversal Potential

The majority of ionic currents are composed by sodium, potassium, and calcium. Due to selective membrane channels that allow one type of ion through, each ion has an equilibrium potential given by the Nernst potential that drives the flux through the membrane. The Nernst, or reversal, potential is the transmembrane voltage value at which the net flow of an ion is zero across the membrane, due to a balance of concentration difference and electrical

difference. For a myocyte with multiple ions, the reversal potential can be computed using the Goldman-Hodgkin-Katz equation.

1.1.2 Modeling the Electrical System

Cardiomyocytes use ionic gradients as a source of fast signalling[16]. By separating different species of ions across the membrane, cells can be induced to change the transmembrane voltage value quickly as a signaling mechanism. Physiologically, the cardiac myocyte membrane is composed of two layers of lipids which are hydrophobic at the tail ends and hydrophilic at the heads. Adjacent cells are connected through gap junctions in which ionic current flows through[17][16].

As the SA node stimulates the heart, signals conduct along the atrial and ventricular myocytes by changing the transmembrane voltage difference. If sufficient, the stimulus raises the transmembrane voltage of a myocyte to a threshold, then depolarizes due to the fast release of the sodium current. As a cell's neighbor depolarizes, the voltage gradient between the two leads to diffusion of electric current from the higher voltage to low. Gap junctions, or connexons, allow for these ions to pass[14].

As an approximation, the myocyte and its neighbors can be abstracted as resistors and capacitors in series and result in an equation known as the cable equation[18]. The cell bilipid membrane acts as a capacitor, while the ionic channels dynamics behave like resistors with voltage dependent resistance.

The monodomain cable theory equation is derived in this manner. First, an assumption is made which is that the extracellular fluid is grounded at 0V and essentially constant as position varies. The membrane is approximated as a 1 dimensional cable with the transmembrane voltage conducting from one section to adjacent sections. Thus, the two types of currents that pass are the transmembrane currents, I_m across the membrane, and the axial currents, $I(x)$ along the cable, in figure 1.4[16].

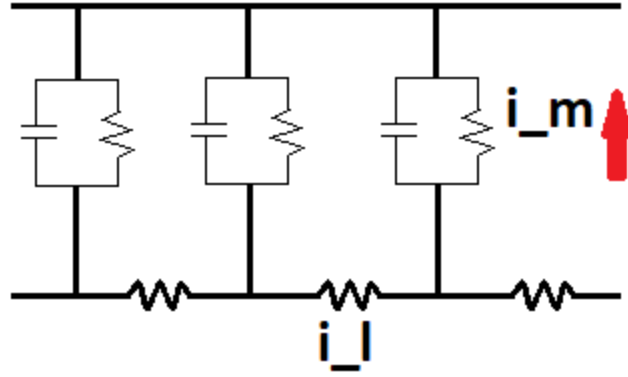


Figure 1.4: Schematic diagram of cable theory and the currents in the cable theory, $I(x)$ and I_m , the axial and transmembrane currents.

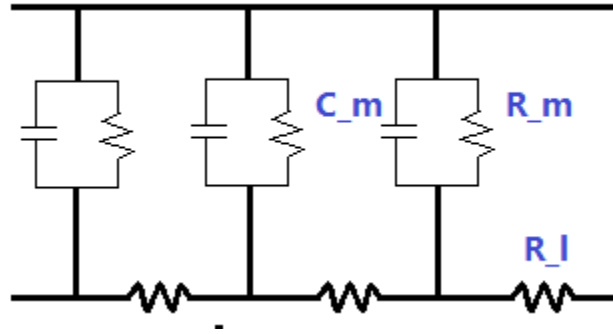


Figure 1.5: Schematic diagram of the cable theory resistors and capacitors, where c_m and c_m are the membrane parameters and r_l is the axial resistance.

Intracellularly in the axial direction, the currents that travel through ionic medium are termed i_l . Through the membrane, the currents are designated as I_m . To calculate the currents, it is necessary to obtain the capacitance and resistance along the membrane. The resistance and capacitance value of a cell can be calculated by obtaining the specific resistance and specific capacitance, R_m , C_m , and ρ_l , which have units of Ωm^2 , F/m^2 , and Ωm respectively. But since we are approximating the membrane as a 1 dimensional cable, the values are divided by units of area to be redefined as a resistance and capacitance per

length[16].

$$\begin{aligned}
 r_m &= \frac{R_m}{2\pi a} \\
 c_m &= \frac{C_m}{2\pi a} \\
 r_l &= \frac{\rho_l}{\pi a^2}
 \end{aligned} \tag{1.1}$$

a is the radius of the cable.

To derive the cable equation, first, we consider the axial voltage at two positions $x + dx$ and x . The voltage at x is $V(x)$ and at $x + dx$ is $V(x + dx)$. The voltage drop between the two is equal to the resistance multiplied by the current.

$$\begin{aligned}
 V(x + dx) - V(x) &= -i_l r_l \Delta x \\
 \frac{V(x + dx) - V(x)}{\Delta x} &= -i_l r_l \\
 \frac{dV}{dx} &= -i_l r_l \\
 \frac{1}{r_l} \frac{dV}{dx} &= -i_l
 \end{aligned} \tag{1.2}$$

The negative sign in front of the current is due to the fact that positive current flows towards negative potentials. Next, the axial current value will change if there is transmembrane current moving in or out. Thus, between two positions x and $x + dx$, the current change by position is equal to the total amount of I_m [16]. If the rate of change of axial current is i_m , or current leaked out per distance unit dx , then

$$\begin{aligned}
 i_l(x + dx) - i_l(x) &= -i_m \Delta x \\
 \frac{i_l(x + dx) - i_l(x)}{\Delta x} &= -i_m \\
 \frac{di_l}{dx} &= -i_m
 \end{aligned} \tag{1.3}$$

Since i_m is equal to the current through the transmembrane resistor and the membrane capacitor, we can replace it with the capacitive current and the ionic currents, where c_m is

the membrane capacitance.

$$\begin{aligned}
i_m &= i_c + i_{ion} \\
i_c &= c_m \frac{dV}{dt} \\
i_m &= c_m \frac{dV}{dt} + i_{ion} \\
-\frac{di_l}{dx} &= c_m \frac{dV}{dt} + i_{ion}
\end{aligned} \tag{1.4}$$

By replacing the equation for $-\frac{di_l}{dx}$, we come to the cable equation, shown below. i_{ion} are the currents of sodium, potassium, and calcium that pass through the membrane.

$$\begin{aligned}
\frac{1}{r_l} \frac{dV^2}{dx^2} &= c_m \frac{dV}{dt} + i_{ion} \\
-c_m \frac{dV}{dt} &= -\frac{1}{r_l} \frac{dV^2}{dx^2} + i_{ion} \\
c_m \frac{dV}{dt} &= \frac{1}{r_l} \frac{dV^2}{dx^2} - i_{ion}
\end{aligned} \tag{1.5}$$

$$c_m \frac{dV}{dt} = \frac{1}{r_l} \frac{dV^2}{dx^2} - i_{ion} \tag{1.6}$$

By dividing the equation with c_m , we obtain the more popular form

$$\frac{dV}{dt} = \frac{1}{r_l c_m} \frac{dV^2}{dx^2} - \frac{i_{ion}}{c_m} \tag{1.7}$$

C_m is usually given with a value of 1 and the factors in front of the second partial derivative are combined into the letter D.

$$\frac{dV}{dt} = D \frac{dV^2}{dx^2} - i_{ion} \tag{1.8}$$

The equation above is the commonly used form for the cable equation.

1.1.3 Instability of the Electrical System

Research in the past decades have targeted multiple mechanisms as a pathway towards VF.

In figure 1.6, we summarize the main types of mechanisms towards arrhythmia [19].

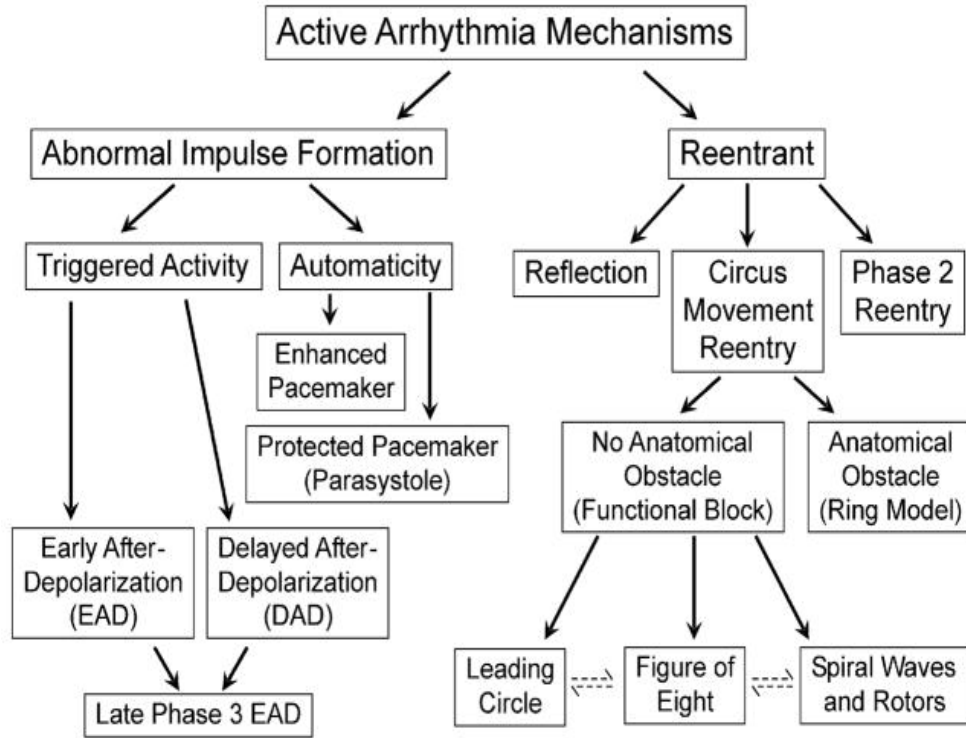


Figure 1.6: A summary diagram of the basic pathways towards arrhythmia[19]. Reentry and abnormal pulse form the two main mechanisms, with multiple causes leading to each.

1.1.4 Abnormal Pulse Formation

Abnormal pulse formation is the appearance of an ectopic stimulus that deviates from normal SA node activity, shown in the left branch in figure 1.6. In regular conditions, the automaticity of the SA node overdrives other pacemakers[19]. While other self-exciting tissue such as the AV node and the purkinje fibers can spontaneously stimulate surrounding tissue, under normal conditions this behavior is latent[19]. In irregular conditions, a common mechanism by which the SA node dominance is disrupted is due to irregular expression of potassium channels[19]. When extracellular potassium is increased, the resting membrane

potential increases and influx currents are stronger against repolarizing currents. Secondly, if latent pacemaker is surrounded by diseased tissue, signaling from the SA node can be blocked. The SA node typically overdrives other pacemakers, but when it is prevented by dysfunctional tissue, the latent pacemakers can produce abnormal pulses[19].

A second mechanism for increased ectopic pulses is through triggered activity, most commonly known afterdepolarizations[20][21]. Triggered activity is defined as superfluous depolarizations following a previous depolarization to stimulus. Depending on the timing of triggered activity, it can be named Early after-depolarizations or Delayed after-depolarizations, in phase 2, and phase 3 of the AP respectively. If a group of adjacent cells of sufficient size produce triggered activity, the surrounding tissue can be depolarized, deviating the tissue from normal pacemaker activity[20]. Conditions that lead to EADs and DADs are LQT syndrome, calcium system malfunction, and late sodium channel activity. In the ECG, triggered activity can induce Torsade de Pointes and Polymorphic Ventricular Tachycardia[20].

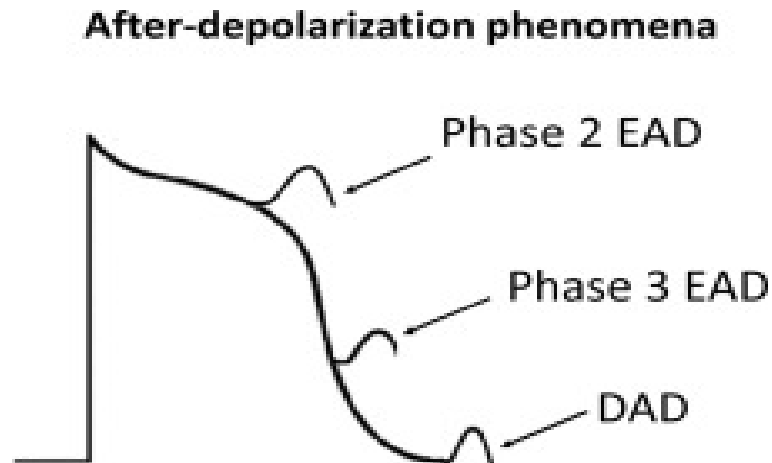


Figure 1.7: [22]Image shows examples of the early-afterdepolarizations(EAD) and Delayed after-depolarizations(DADs) in a cardiomyocyte action potential time series.EADs are extra excitations in phase 2 or phase 3 of the action potential, and DADs are excitations during early phase 4.

1.1.5 Reentry

Reentry, depicted in the right branch of 1.6, is the phenomena when the same stimulus re-excites the tissue. It differs from triggered activity in that the triggered activity follows a stimulus, whereas reentry is the re-excitation from the same stimulus. A widely studied phenomena of reentry is the spiral wave, a rotating electrical wave that overdrives the SA node, sending tissue into tachycardia, shown in figure 1.8.

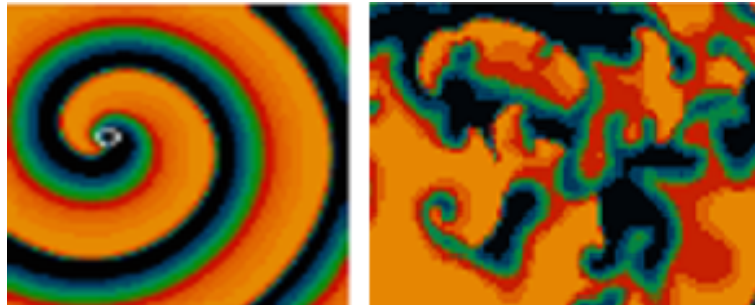


Figure 1.8: Image captures a snapshot of a simulation of cardiac tissue demonstrating a typical spiral wave on the left panel. Orange is areas of depolarization while black are areas of rest. On the right, the spiral wave breakup and tissue enters chaos[23]

Since cardiac tissue is three dimensional, the analog of the spiral wave in a heart is the rotor. While a single rotor can be stable and not immediately fatal, spiral wave breakup(SWB) is critical. When a single spiral wave breakups into multiple waves, the heart no longer contracts in a coordinated fashion and will quiver in place , and sudden cardiac death can result[24][25][26][27]. Due to the intricate complexities of the heart, multiple pathways to spiral waves can exist. An ectopic pulse in the correct substrate can induce a wave that propagates in a circular motion. On the other hand, conduction block in a region of diseased tissue can cause the adjacent excitation to propagate by curling into the blocked region after recovery. Anatomical objects such as atria or vessels can provide regions of block as well. Moreover, accessory pathways shown in conditions such as Wolff-Parkinson-White syndrome,in figure 1.9, can produce signals that disturb the SA node's dominance. For the WPW syndrome, an extra pathway between the atria and ven-

tricles creates a circular pathway for the stimulus to re-excite the ventricles, as shown in figure 1.9.

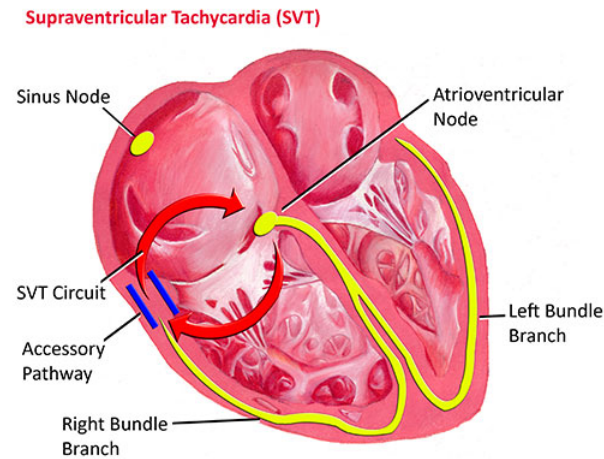


Figure 1.9: Image demonstrates an example of an accessory pathway for excitation that leads to reentry. This syndrome is termed the Wolfe-Parkinson-White syndrome, where an extraneous connection between the ventricles and atria exists[28]. As a result, the excitation in the ventricles return to the atria through the accessory pathway and re-excites the tissue

1.1.6 Alternans to Arrhythmia

Described in the seminal paper by Nolasco and Dahlen in 1968, the authors provided an conceptually insightful method to analyze a type of instability known as action potential duration alternans[29][30]. Action Potential Duration, APD, is the duration in which the action potential remains above a voltage threshold, and the diastolic interval, DI, is the time of recovery. The two time variables have a direct coupled relationship because the longer the system has to recover, or in other words a longer DI, more excited the system will be due to the recovery of the currents and have a larger APD[29][30]. In a typical normal heart with a constant pacing length, the APD and DI are relatively constant beat to beat. APD and DI relationship can be experimentally measured in different cardiac tissues[31]. Given such a relationship between the two, we can predict the onset of the alternans through period doubling bifurcation and graphically visualize different states. For instability analysis, two functions are necessary to iterate forward in discrete time given an

initial pacing length and APD or DI[30]. The first function is the restitution relationship, which relates DI_n to APD_{n+1} , indicating that for a larger previous DI, a larger APD will follow. Here, we examine the simplest relationship, which is a monotonically increasing function, but it should be noted that the relationship can be non-monotonic as well. The second function is the period, T , relationship, where the DI and APD of the same beat are related. In the return diagram, the two functions are shown, with the first function being the restitution function and the second being the period function.

$$\begin{aligned} APD_{n+1} &= R(DI_n) \\ T_n &= APD_n + DI_n \end{aligned} \tag{1.9}$$

Given a DI at beat n , we can predict the subsequent APD_{n+1} using the restitution, then the DI for beat $n+1$ using the period function, then the APD for beat $n+2$, etc. This forward iteration can be plotted in a return map in figure 1.10. When plotted, the crossing of the two functions is an equilibrium state. Bifurcation analysis indicates that by linearizing around the fixed point, we can predict that when the local slope of the restitution function has a magnitude greater than 1, then the fixed point will descend into alternans[30][29]. In the return map, two common behaviors are shown as well. If the system is at a normal state, the iteration forward converge to a fixed point value that indicates constant APD and DI. If the system is in alternans mode, the APD and DI value switch between two sets of points.

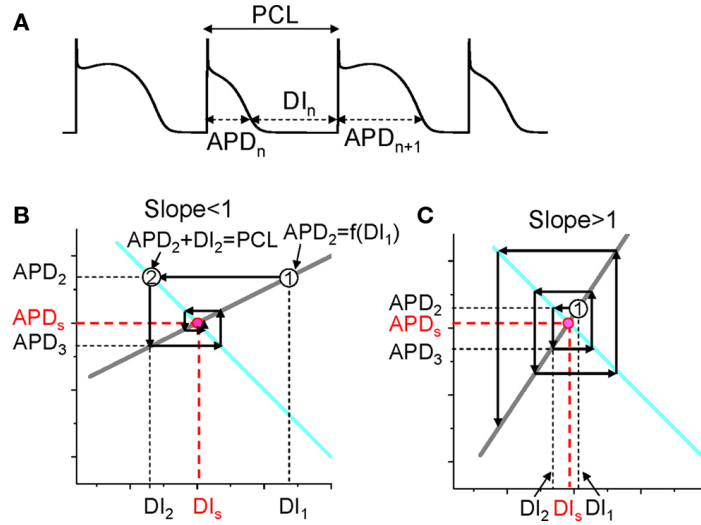


Figure 1.10: [32]The top image shows the definitions of the APD and DI according a period, or PCL. The bottom image is the APD return map for two different types of behaviors depending on the slope of the APD restitution function of DI. If the slope is greater than 1, then the system will have alternans(right). If not, the system will have a steady value of APD and DI(left)

The danger in alternans lies not just in its irregularity but also in its spatial effects. The most arrhythmogenic type of alternans are that which lead to dispersion of behavior in space[31][33][34]. When the tissue is uniformly in the alternans state, or spatially concordant alternans, the whole tissue may alternate, but the contraction is still coordinated. On the other hand, if spatially discordant alternans, or SDA, occurs, there is a gradient of recovery between adjacent tissue[33], shown in figure 1.12. If a well timed ectopic beat appear at location B in the figure, it would encounter unrecovered tissue in one direction and not the other. Thus, the beat would propagate laterally. While in the meantime, the adjacent tissue would recover, and the lateral beat may curl around induce reentry[33].

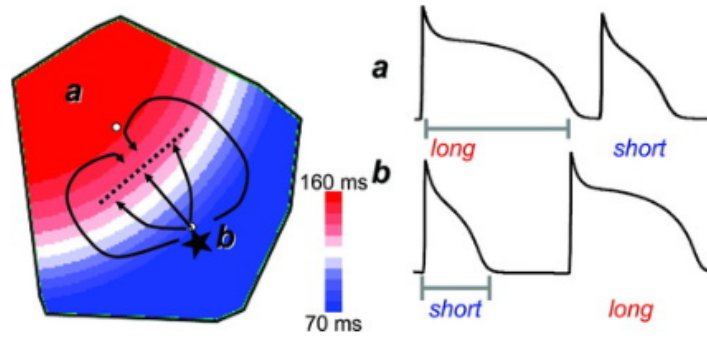


Figure 1.11: [33]Image demonstrating a cardiac tissue simulation showing spatially discordant alternans. In certain areas the cellular action potential signal, shown in the right, alternates long short, and in other areas alternates short long. This causes a gradient of behavior, show in the left, such that if an ectopic beat at *b* occurred, it would propagate laterally, then curl in causing reentry.

1.2 Some open Questions in Cardiac Research

1.2.1 Phenomenological vs. Complex Models

A spectrum of perspectives exists on the topic of modeling the cardiac system. As a whole, the heart is an intricately complex system with a myriad of ionic currents, proteins, and structure. Models within the community such as Ten-Tusscher and O'hara-Rudy endeavor to reconstructed realistic dynamics of the heart[35][36]. Unfortunately, such models have hundreds of dynamical equations and often more than 20 state variables, which renders simulations of thousands of cells simultaneously difficult. On the other hand, minimal models such as Beeler-Reuter, Noble, Fenton-Karma, and Fitzhugh-Nagumo have less than 10 variables[17][37][38][15]. In addition, they can be relatively easily fitted to experimental plots and mimic behavior such as spiral waves and alternans. Unfortunately, such simplicity also means that many of the underlying dynamics are condensed into single variables. For simulations that produce the effects of drugs on the system, especially, such simple models are less useful than complex models. Using cardiac modeling to solve problems often requires an understanding of the specificity of the problem itself, whether it requires a particular ionic current or simply needs a general type of phenomena.

1.2.2 APD Alternans

APD alternans is a widely accepted path towards instability. However, experimental data have shown that even when the APD restitution function has a flat shape, alternans can occur[39][40][41]. Calcium cycling has been nominated as the source of instability because of its coupling to the APD. However, we observe in experimental laboratory data that even without the calcium cycling system, VF can occur if amplitude alternans appear[40][41]. Amplitude of action potentials are important because of its effects on conduction block. Because conduction block can often lead to reentry and alternans increase the likelihood of conduction block, previously, APD alternans were studied to examine the conditions such phenomena. However, conduction block occurs when the amplitude of the AP is too small, and not only the APD. Moreover, literature search reveals that amplitude alternans are more correlated to VF than APD alternans[41]. Other sources of instability must be examined to gain a wider understanding of the path towards to arrhythmia.

1.2.3 Spiral Waves as a Path to Arrhythmia

Spiral wave breakup is a highly studied path towards arrhythmia. The induction, persistence and breakup of spiral waves are acutely examined in cardiac research. However, distinct spiral waves branches do not persist for long in experimental data. In a manuscript by Gray published in 2008, the author notes that an underlying excitable and oscillatory nature in cardiac models produce chaotic patterns such as circular target waves. Even if the tissue begins with a spiral waves, the shape of the wave destabilizes into target patterns and general chaotic behavior. In fact, hearts in VF show more globular oscillations rather than distinct spiral wave shapes. In our lab, we produce experimental data that do not conform to the typical VF simulations of spiral wave breakup.

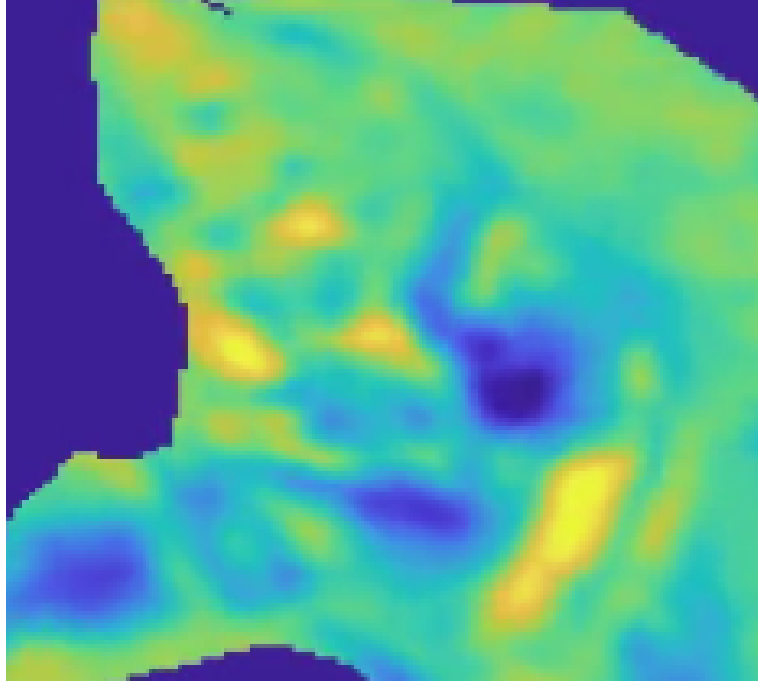


Figure 1.12: Image depicts a snapshot of our laboratory’s experimental rabbit ventricle data during VF. The yellow spots indicate excitation, while blue indicates rest. Most notably, there are not many distinct spiral wave branches.

1.2.4 Calcium Alternans

While APD alternans were previously accepted as a path towards arrhythmia, current research indicates that APD can alternate even if the restitution function is flattened[40][39][33]. A source of instability can originate from the calcium cycling system due to its nonlinear bidirectional coupling to the voltage system. The calcium system can produce alternans like that of the voltage system and is more complex spatially, even within one cardiac cell. While a single cell can be considered as a single voltage unit, the calcium system within one cell is composed of hundreds of calcium units. Thus, increases in the complexity of calcium models can exponentially increase the difficulty of simulations in tissue. In selecting the correct model for cardiac simulations, it is difficult to capture every ionic current dynamic and also have a computationally inexpensive simulations. While many calcium models exist that reproduce fine details of cardiac dynamics, minimal calcium models are

lesser in number. Moreover, some minimal models do not capture the major aspects of calcium cycling system, such as graded release from sparks, and the major sources of calcium alternans. To further calcium cycling research and simulation, an updated minimal calcium model must be constructed.

1.3 Acronyms

AP=Action Potential

APA=Action Potential Amplitude

APD=Action Potential Duration

BR =Beeler-Reuter

CICR=Calcium Induced Calcium Release

DI=Diastolic Interval

ECG=Electrocardiogram

I_{ca} =L-Type calcium current

I_{naca} =Sodium-calcium exchanger current

JSR=Junctional Sarcoplasmic Reticulum

LR=Luo-Rudy

NSR=Network Sarcoplasmic Reticulum, or bulk SR.

Ryr=Ryanodine receptors

SA=Sinoatrial

SCD=Sudden Cardiac Death

SDA=spatially discordant alternans

SR=Sarcoplasmic Reticulum

SWB=Spiral Wave Breakup

VF=Ventricular Fibrillation

CHAPTER 2

ACTION POTENTIAL AMPLITUDE ALTERNANS

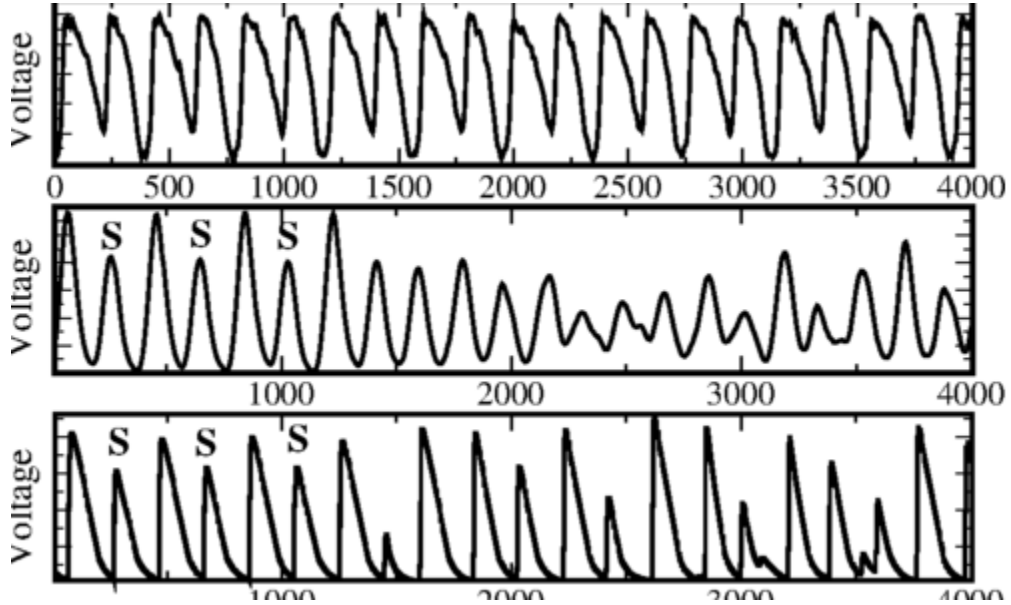


Figure 2.1: Top panel plots experimental rabbit APD alternans in time series. Middle panel show rabbit ventricles in VF with distinct amplitude alternans. Bottom panel is the Fenton-Karma model in time series showing VF in tissue simulations[40] In these plots, data in time series demonstrates that APD alternans can be stable and that amplitude alternans are more correlated to VF.

..

While APD alternans analysis is intuitive, its predictive power often falls short[41]. In reality, many factors exert influence on the APD, such ionic memory and calcium dynamics, and alternans can commonly occur even when the restitution function is flat[42][43][44][45]. Moreover, experimentally, one can record large APD differences from beat to beat without degeneration into VF in figure 2.1. In this section, we introduce another perspective in targeting the precursors to arrhythmia by examining the action potential amplitude(APA) rather than only the APD. From experimental data, we observe that in the second panel in figure 2.1, VF follows when there are significant alternans in amplitude of action potential.

Other experimental data from literature demonstrate that T-wave alternans, the ECG manifestation of APD alternans, is a relatively poor indicator of VF [41][46]. Rather, recent literature have shown that amplitude is more critical[41]. Furthermore, conduction block, a mechanism for reentry, is not possible if the amplitude is too small. Pure APD alternans with no amplitude alternans will have less chance of conduction block.

2.1 Minimal Model for APA Alternans

To study action potential amplitude, we construct a minimal model to reproduce experimental data. We use the Beeler-Reuter rabbit ventricle model as a basis and reduce to the minimum number of variable to unmask APA alternans[47]. In addition, we make simplifications in equation form for ease of manipulation.

2.1.1 Formulation of Model

Many cardiac models' ionic currents are typically structured the Hodgkin-Huxley form[48]. Using Ohm's law, the currents for a specific ion, such as sodium, is equal to the transmembrane voltage divided by the resistance[47].

$$I_{na} = G(V - E_{na}) \quad (2.1)$$

Where the e_{na} is the Nernst equilibrium potential of the sodium ion, V is the transmembrane voltage, and g is inverse of resistance[47].

G is formulated to represent the likelihood of ionic gating channels opening and closing, mimicking resistance in a wire. In real life, the sodium protein channels have complex stochastic dynamics that can be modeled with markovian style equations[49]. As a simplification, Hodgkin-Huxley models abstract the channel as an object with multiple gates that open and close with time dependence. In the sodium current, 3 gates are generally used, m the activation gate, and h and j the inactivation gates. Each gate variable represents the

proportion of the gates that are opened. Thus, the model's equation for the sodium channel is non-zero when the 3 types of gates have non-zero values[49].

$$I_{na} = g_{na}m^3hj(V - E_{na}) \quad (2.2)$$

The style of the gating equations are as follows:

$$\frac{dh}{dt} = \alpha_h(1 - h) - \beta_h h \quad (2.3)$$

the α value is a rate constant that determines the proportions of closed h gates that will fire per discrete unit of time. The β value is a rate constant that determines the proportions of open gates. In certain formulations, the dynamical h variable equation can be rearranged as:

$$\begin{aligned} h_{\infty} &= \alpha_h / (\alpha_h + \beta_h) \\ \tau_h &= 1 / (\alpha_h + \beta_h) \\ \frac{dh}{dt} &= (h_{\infty} - h) / \tau_h \end{aligned} \quad (2.4)$$

In the restructured gating equation, the h_{∞} is a steady state value that the system approaches with the time constant τ_h

In our construction of an APA model, we delete the Beeler-Reuter currents that do not have a direct effect on the amplitude, including the calcium currents and extraneous potassium currents. As a further simplification, we construct the potassium current so that it is voltage dependent only and has no time dependence, thus reducing the phase space of our model[40]. What remains are the standard currents for depolarizing and repolarizing, which are the sodium and potassium currents. In the sodium current, while there are three types of time dependent gates, the m activation gates time constants are relatively small, so we make this gating variable time independent. Finally, we remove the j gate in the sodium channel equations since only one gate is necessary to close the current at high voltage

values. The resulting model is shown in equation ?? and plotted in 2.2. It has two time dependent variables Voltage, v and h gate, h , and two currents sodium and potassium. Both variables are plotted in scale, and we observe that amplitude alternans occur after a pacing threshold. See supplementary of Chen 2017 et.al. for model details.

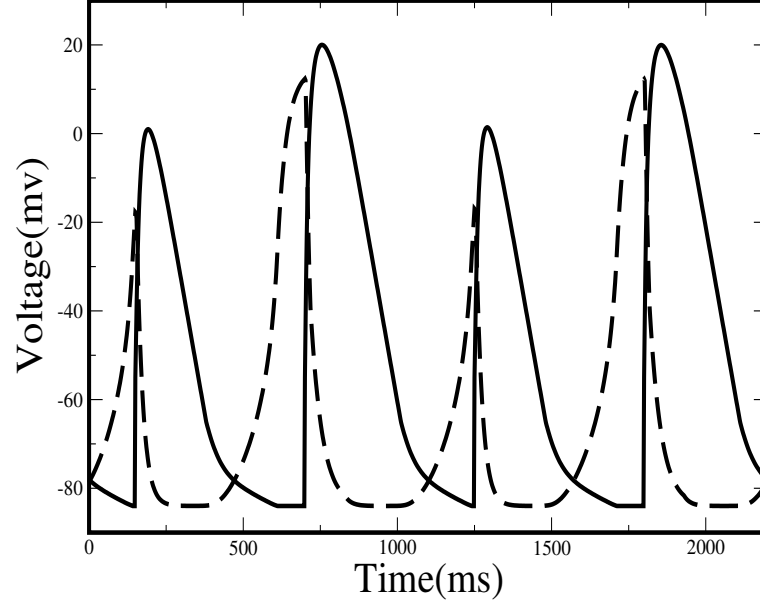


Figure 2.2: Image shows a typical signal from our two variable model. The x axis is time in milliseconds, and the y axis is voltage in time series (solid line) and h gate value (dotted line, scaled). This signal is demonstrating APA alternation due to the h gate alternating [40].

$$\begin{aligned} \frac{\partial V}{\partial t} &= D \frac{\partial^2 V}{\partial x^2} - g_{na} m_{\infty}^3 h (V - E_{na}) - I_k \\ \frac{\partial h}{\partial t} &= \frac{h_{\infty} - h}{\tau_h} \end{aligned} \quad (2.5)$$

2.1.2 Derivation of the APA Map

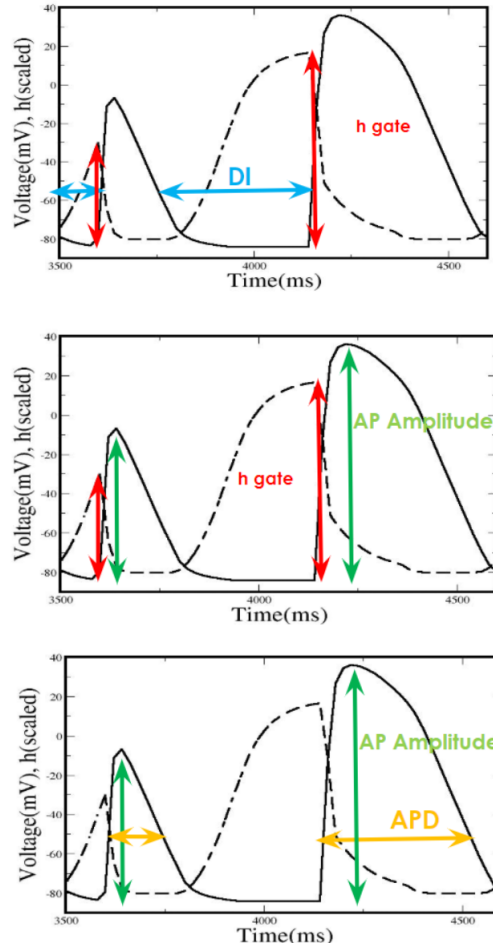


Figure 2.3: Figure visualizes the three important relationships we extracted from observations of the 2 variable model: h gate and DI, h gate and amplitude, and amplitude and APD[40]. Top image shows that the h gate value at the end of a beat is proportional to the DI, the second image shows that the amplitude of a beat is proportional to the h h gate value of the previous beat, and the last bottom image shows that the APD and APA are directly related.

From the minimal model of amplitude alternans, we extract three key relationships among the state variables of the system when simulated in a single cell. In our two variable model, the amplitude is determined by the sodium current strength, which is related to how much the h gate recovers at the end of the previous beat. Thus, the APA at beat $n+1$ is proportional to h variable by end of beat n , as indicated in figure 2.3[40]. The h variable is proportional

to the DI of the same beat because the longer the cell has time to recover, the larger the h variable at the end of that beat, shown by arrows in figure 2.3 . For the same beat, the larger the amplitude, the longer it takes for the cell to recover to rest. The three relations are summarized below, with n being the pacing index. The functions L , F , and G are abstract functions that relate variables. In simulation, we will numerically calculate these function relationships[40].

$$DI_n = L(h_n) \quad (2.6)$$

$$APA_{n+1} = F(h_n) \quad (2.7)$$

$$APD_n = G(APA_n) \quad (2.8)$$

With these three relationships above, we can define the APA return map, analogous to the APD return map. Firstly, we note that the APD map is defined by a restitution function and a period function[29].

$$APD_{n+1} = R(DI_n) \quad (2.9)$$

$$APD_n + DI_n = T(\text{constant}). \quad (2.10)$$

Because the 3 relationships we observe relate APD, DI, h , and APA, we can take the relationship from the APD period function and replace DI and APD with h and APA[40].

First, the APD period function rewritten as:

$$T = G(APA_n) + L(h_n). \quad (2.11)$$

Then, we rearrange the equation to this form.

$$APA_n = G^{-1}(T - L(h_n)) = Y(h_n, T), \quad (2.12)$$

Next, since APD is directly related to APA, and DI is directly related to h, the APD restitution function can be rewritten as an APA restitution function

$$APD_n = G(APA_n) \quad (2.13)$$

$$APA_{n+1} = F(h_n) \quad (2.14)$$

Now, given the full APA restitution map, with the restitution function and the period function, we can analyze the fixed point.

The period function can be rearranged to the following form.

$$Y(h_{n+1}, T) = F(h_n). \quad (2.15)$$

By inverting the period function, we can obtain the following form for the period function[40].

$$h_{n+1} = Y^{-1}(F(h_n), T). \quad (2.16)$$

Now, given the return map, we linearize around the fixed point h^* .

$$\left. \frac{\delta h_{n+1}}{\delta h_n} \right|_{h^*} = \left(\frac{\delta Y^{-1}(F(h_n), T)}{\delta F(h_n)} \right) \left(\frac{\delta F(h_n)}{\delta h_n} \right) \Big|_{h^*} = \frac{\left. \frac{\delta F}{\delta h_n} \right|_{h^*}}{\left. \frac{\delta Y}{\delta h_n} \right|_{h^*}} \quad (2.17)$$

By interpreting the equation above, we see that the stability of the fixed point is the ratio of two derivatives of the function F and Y[40].

$$1 \leq \left| \frac{\text{slope of APA restitution function}}{\text{slope of period function}} \right| \Big|_{h^*} \equiv |\rho|. \quad (2.18)$$

This equation indicates that the stability of the fixed point is the ratio of the slope of the two functions around the fixed point. If this ratio is larger than 1 in magnitude, amplitude alternans will occur[40].

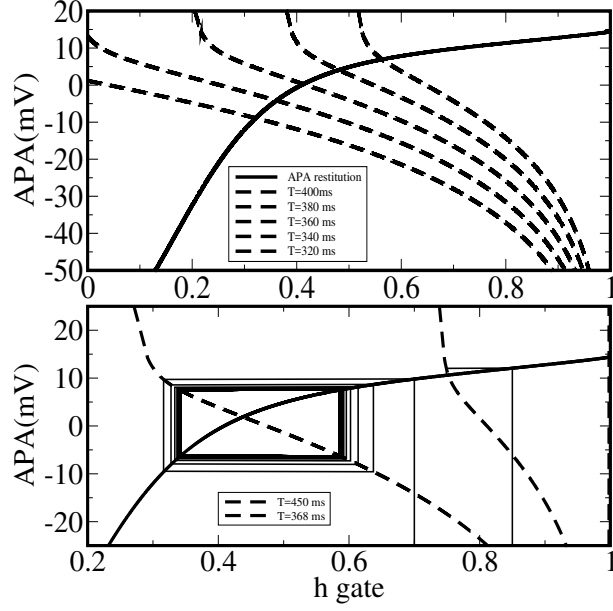


Figure 2.4: Top: Amplitude versus h gate restitution curve and period curves, solid and dashed line respectively, for five different periods (320,340,360,380, and 400 ms). Bottom: A cobweb diagram for a period with a stable fixed point (450ms dashed) and for a period with alternans (368ms solid line)[40].

2.1.3 Confirmation of the Stability Condition Through Numerical Analysis

Using these two functions, we plot a return map analogous to that of the APD[29][30]. Through the S1S2 protocol, we calculate approximate relationships between DI, APD, APA, and h to fit the abstract functions L, G, and F.

The protocol is as follows: By taking our model, we pace the system at a relatively long period, 500ms. This produces a steady train of pulses with steady APDs, which we term S1 pulses. After 20 paces, we pace the system with a decreased period. This produces a smaller DI, APD, h gate, and APA for the subsequent S2 pulse that is proportionate to the second period T. See figure 2.5 for details.

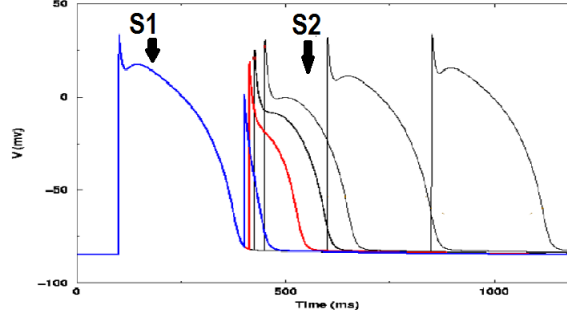


Figure 2.5: Image demonstrates the S1S2 pacing protocol[29]. The S1 is the first beat shown in the plot, and the S2 are the following beats. Depending on the timing of the second action potential, the S2 beat's shape and amplitude will vary. The longer the DI after the S1, the larger the APA and APD of the S2

We apply this protocol for many periods to construct a set of data between DI, APD, h variable, and APA to visualize the relationships between the state variables.

Next, we numerically calculate the APA return map functions and plot in the figure 2.4[40]. For both the APD and APA maps, we have a restitution function and a period function. A key difference between the two is qualitative shape. The period function for the APA return map is curved rather than a diagonal line[29]. In addition, as the period increases, the slope around the fixed point increases for the period function as well, whereas for the APD return map the period relationship shifts but maintains a slope of 1. Since the amplitude alternans occur at lower periods, this properties corroborates the ratio condition.

In figure 2.4, we demonstrate two different dynamics in our model using the APA return map. When paced slowly with a high period, the period function have a large slope at the fixed point, which leads to a lower ratio for the stability condition. When iterating forward in a cobweb diagram, the dynamics converge to a fixed point. On the other hand, if the period is small, the intersection between the functions have a larger ratio. The slope of the period function is small, so the ratio is large. If we iterate forward in discrete time, the APA alternates between two values every beat[40].

2.1.4 Physiological Connection with Parameters

While numerical calculations confirm the validity of our equations, we proceeded to gain a deeper understanding of the equation by connecting it to physiological parameters and deriving explicit instability conditions instead of numerically fitting to L, G, and F functions. First, we approximated the relationships with simple functions such as logarithmic and linear equations. The relationship between DI and h gate is exponential in nature while APD vs APA and APA vs h are more linear. In addition, local to the fixed point, these functions can fit the linearized neighborhood dynamics well. Now, the equations have parameters, seen below.

$$APA_{n+1} = \beta h_n + B_1 \quad (2.19)$$

$$APD_n = \alpha APA_n + C_1 \quad (2.20)$$

$$h = 1 - ae^{-DI/\tau_h} \quad (2.21)$$

By inserting these relationships through the stability condition, we now have a stability equation with explicit parameters.

$$\rho = \beta\alpha(1 - h^*)/\tau_h. \quad (2.22)$$

From the equation above, we deduce that if the combination of the parameters are such that the variable ρ is greater than 1 in magnitude, then amplitude alternans will occur. By examining the model and looking at the instability equation, we can extract information about the factors that increase amplitude alternans. The parameter β is related to the maximum excitability parameter of the sodium channel current, G_{na} . What this implies is that the more excitable, the more likely for amplitude alternans. The α is related to the magnitude of the potassium current, which returns the cell to its resting state. If the current is low in magnitude, then the amplitude alternans are more likely to occur. The τ is the time

constant of the h gate, which indicates that the smaller the time constant, the more likely the alternans. The h^* is related to the period of pacing, and through observation we note that the faster the stimulus, the more likelihood of amplitude alternans occurrence.

2.2 Discussion

In this project, we present a novel method to examine the instability of AP. From laboratory experimental data and literature, we note that APD alternans does not necessarily guarantee conduction block, rather APA alternans is more correlated to arrhythmia. From the BR model, we construct a minimal two variable model to unmask APA alternans. By observing the dynamics, we extract three relationships between DI, APD, h , and amplitude of voltage. From the APD return map, we replace APD and DI with h and amplitude and derive the APA alternans return map. Furthermore, we connected the APA map to physiological parameters and formulated an equation that predicts on the onset of APA alternans.

A possible use for our analysis may be as follows. Using a Pseudo ECG protocol, we simulate our model in a cable and calculate its ECG. The result, in figure 2.6, shows distinct QRS alternans. Since the QRS wave is a whole heart visualization of the spreading the wave front, a smaller amplitude wave front will result in a lower voltage difference between the ends of the heart tissue. This result suggests that in the future detection of QRS wave alternans may be a possible marker of arrhythmia.

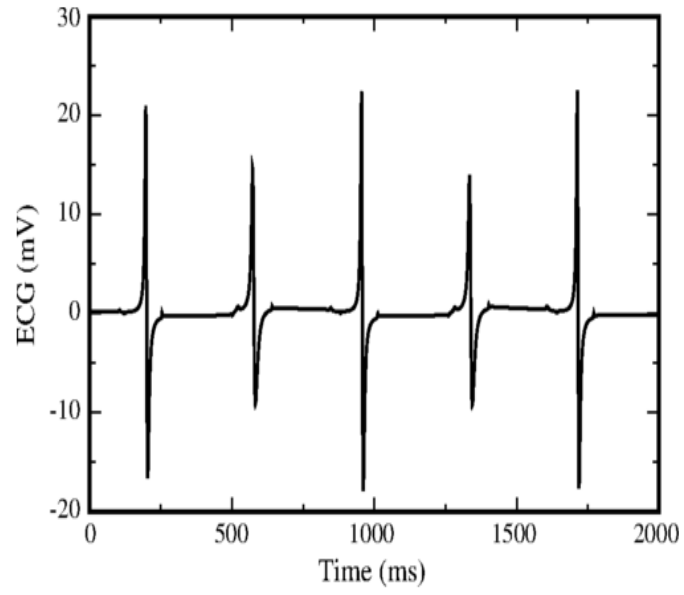


Figure 2.6: A pseudo-ECG of our model in cable when amplitude alternans occur[40]. ECG shows distinct QRS alternans.

CHAPTER 3

TAKE-OFF POTENTIAL

Current cardiac models, which number to more than 50, vary in number of variables and style of equations[15]. Models with minimal amount of variables capture the most salient dynamics phenomenologically. The advantage to such reduction is that the dynamics can be much more easily understood, manipulated, and simulated. However, its limitation is that it does not accurately reflect the detailed ionic dynamics of the real system. On the other hand, complex models can reproduce specific ionic movements, yet they are computationally expensive and difficult to analyze[15]. A particular phenomena which cardiac models aspire to reproduce is fibrillation, when the electrical signal in hearts becomes chaotic and can lead to SCD. Certain aspects such as the APD and DI, and amplitude all vary dramatically during VF, and most cardiac models reproduce these qualities when modeled spatially extended system. However, a characteristic that many models do not capture is the take-off potential, also known as the highest value at which the action potential can excite, variation of the action potential during VF, shown in figure 3.1 in the top panel[50]. During regular heart rhythm, the action potential recovers to resting state before re-exciting. When paced faster however, the take-off potential will slowly rise, and during fibrillation especially, the take off potential of the electrical signal varies significantly[51][52]. In simulations of a significant portion of models in fibrillation, the action potential almost always returns to rest, even during fibrillation. This restricts the complexity of solutions in phase space. By allowing for large and small amplitude oscillations, we countenance for richer dynamics in phase space. In this section, we constructed methods to increase take off potential using typical cardiac minimal models.

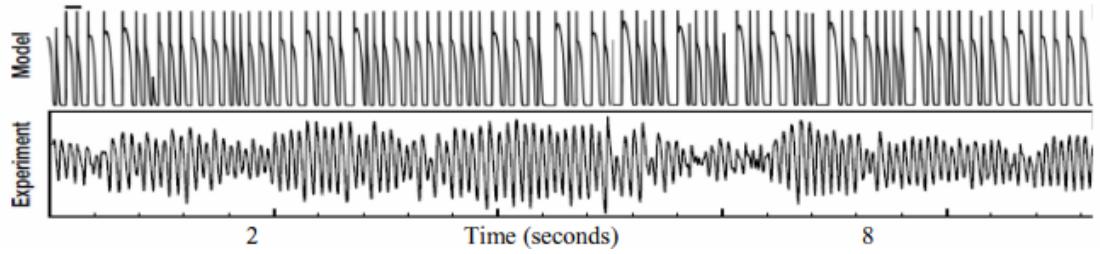


Figure 3.1: [50]Image shows Fenton-Karma four variable model in VF in top panel and experimental data showing VF in the bottom panel. A distinct difference is the lack of variation in the model's take off potential even during VF. The FK model is fit to experimental restitution curves and matches in frequency to the VF time series, but shows qualitatively unrealistic VF due to the variation in TOP

In this project, we focus on Hodgkin-Huxley model equations of commonly used models such as Noble, Luo-Rudy, and Beeler-Reuter models[47][37][53]. We target a source of the low take-off potential, and simplify and adjust the models' equations to ameliorate this issue.

3.1 Cause of Low TOP

For the sodium current to depolarize the cell, the values of the gating variables must all be non-zero and large enough for the sodium current to overcome the repolarizing potassium current.

$$I_{na} = g_{na}m^3hj(V - E_{na}) \quad (3.1)$$

After the stimulus induces response from the sodium current, the inactivation gates, h and j, close quickly at high voltage by dropping to 0, which inactivates the sodium current, hence the reason for their names. As the action potential value drops during phase 3, the inactivation gates slowly recover to a larger value to prepare for the next firing. The time constant of the gating variables determines how fast these gates recover, and only when they recover sufficiently can the system fire again. From observations of the simplified models, we note that the h gate and especially the j gate have large time constants, which

increases the recovery duration for the cell to fire again. Since the action potential drops during recovery, the longer the recovery duration necessary for sodium current to fire, the lower the potential before excitation. Therefore, with the Luo-Rudy, noble, and Beeler-reuter models, we adjust the j gate and its time constants to change the TOP.

3.2 Time constant adjustment

Each gating variable m, h, and j are time dependent functions that recover with time constant τ . In the equation below, we demonstrate a fitting of the Beeler-Reuter rabbit ventricular j gate variable time constant[47].

$$\begin{aligned} \frac{dj}{dt} &= \frac{j_{\infty} - j}{\tau_j} \\ \tau_j &= \frac{1}{\frac{0.055e^{-0.25(v+78)}}{e^{-0.2(v+78)}+1} + \frac{0.3}{e^{-0.1(v+32)}+1}} \end{aligned} \quad (3.2)$$

The time constant equations for the gating variables are complex functions, shown in 3.2. This complexity makes it difficult to understand the role of the h and j gate in the take potential and adjust its values for our purposes. To address this issue, we reduce the complexity by fitting the original time constant equations to simpler forms. The time constant of the j gate is voltage dependent, and its typical shape when plotted against voltage is an asymmetrical gaussian-like form. To simplify the equations, we use two hyperbolic tangents posed in opposite directions to fit in piecewise form to the asymmetrical gaussian shape of the time constant equation plot, shown in figure 3.2. The original time constant and our simpler form are also displayed in 3.2.

$$\begin{aligned} \tau_i^- &= \tau_0^- [\delta^- - \tanh(a^-(V_m - V_i^-))]/2 \\ \tau_i^+ &= \tau_0^+ [\delta^+ + \tanh(a^+(V_m - V_i^+))]/2 \end{aligned} \quad (3.3)$$

τ_i^- is the time constant function for V_m above a threshold voltage. τ_0, δ, V_i and a represent the amplitude, asymptotic value, inflection and steepness respectively.

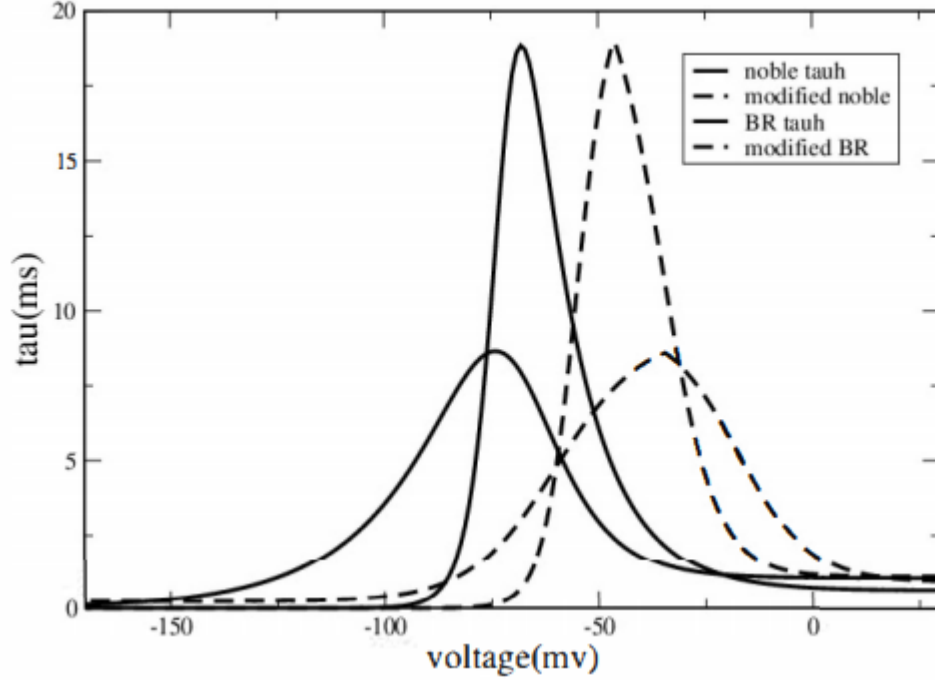


Figure 3.2: [50] Time constants functions for the j gate of Noble and BR model. Solid lines are the original time constant values with a dependence on voltage. Dashed lines are the shifted time constant functions fitted with modified equations.

With the simplified equations for the time constant, the parameter space is significantly reduced. Moreover, we can relatively easily adjust the shape of the time constant by changing its parameters. As an initial exploratory test, we shifted each of the parameters to see the effect on the take off potential. The piecewise equations were manipulated to have different widths, amplitude, and asymmetry in the gaussian form. Overall, the adjustment that created the most change in TOP was the shifting voltage dependence of the time constant equations[50].

In the figure 3.3, we compare the difference between the Luo-Rudy model and the modified Luo-Rudy model. In the modified LR equations, we shifted the j gate time constant equation's peak to the right from the value of -66mV to -60, -51, -36mV. The plot depicts the sodium current response as a function of time. As the peak of the time constant is shifted, the occurrence of inward sodium flux happens earlier, which allows for a higher take-off potential because the system is less recovered.

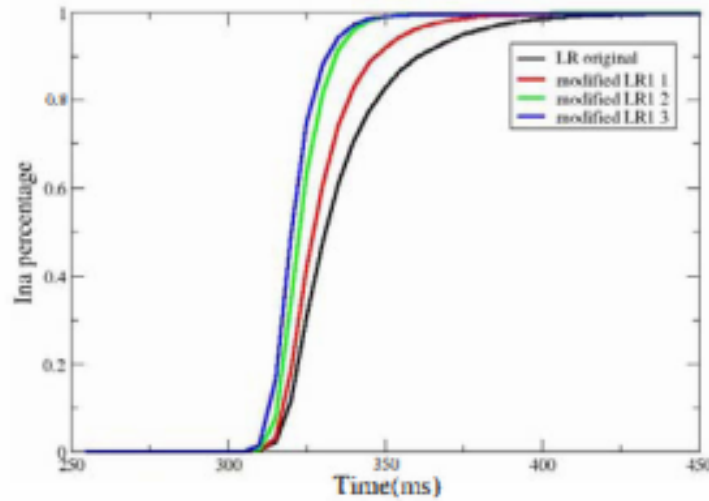


Figure 3.3: Plot demonstrates the sodium current response as a function of time. The peak of the j gate time constant is shifted and the resulting sodium response are plotted in time against the original sodium response in black[50]. Image demonstrates that the modified time constant equations can increase the sodium response to allow the system to fire earlier in time

Next, we modify the Beeler-Reuter and Noble model in cable form. The results are shown in 3.4 and 3.5. For the BR model, we carry simulations in cables of 500 cell elements and for the Noble we use a cable of 100 cell elements. The stimulus site is at the first 10 elements, and we recorded the action potential at various sites along the cable. To highlight the effect the time constant shift and reduce complexity in analysis, we eliminate the j gate and use the h gate for inactivation for BR and Noble. We shift the peak of h gate time constant by 40 mV and observe the highest take-off potential value for both models. For the Noble model, the take off potential is elevated by 11.5mV, and for the BR model, the take off potential increases by 14mV.

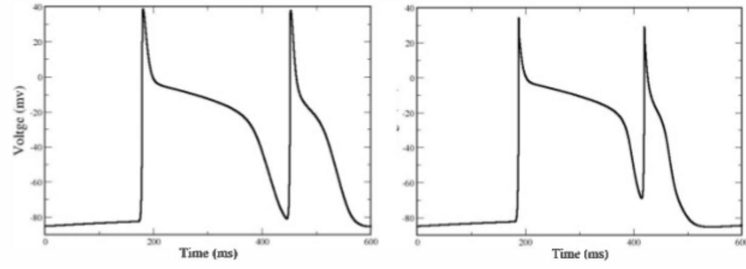


Figure 3.4: Image depicting comparison of modified Noble model with the original Noble model. Left panel is original, right panel is the modified result with an elevation of 11.5mV in TOP[50].

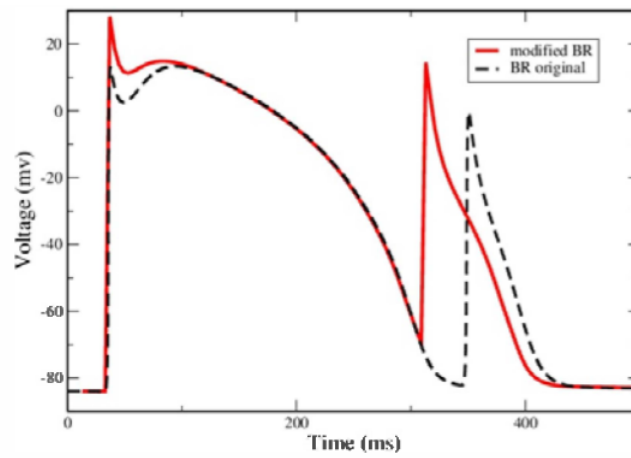


Figure 3.5: Image comparison of modified BR model. Red time series line is modified BR model and dashed black line is original BR model. Modifications results in 14mV elevation in TOP[50].

Finally, in the figure 3.6, we pace the modified noble model with the changed j gate very quickly to imitate fibrillation dynamics. Pacing at 500ms initially and rapidly at 60ms, the take off potential elevates for 14mV for many beats, and then shift back to normal resting potential, demonstrating the success in raising the TOP with the adjust of j gate time constant[50].

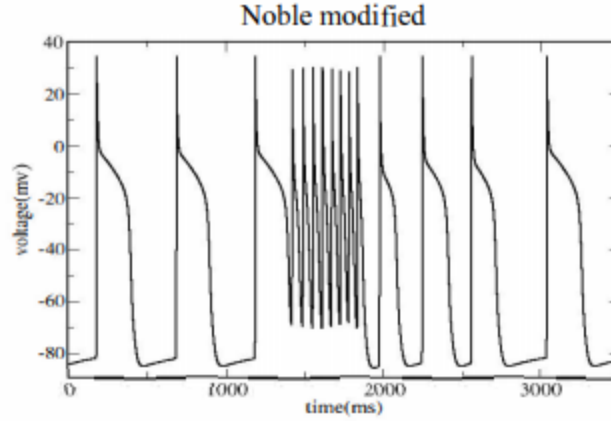


Figure 3.6: [50]Modified Noble model with j gate of time constant shifted. Initially paced at 500ms and then rapidly paced at 60ms to mimic VF, the take off potential is raised significantly indicating our success in raising TOP.

3.3 Discussion

We target the slowly recovering j gate of the sodium current as the culprit in a model's low take off potential due to its relatively slow recovery time. We simplify the complex equations of the gating variable to piecewise hyperbolic tangents to easily manipulate the asymmetric gaussian shape of the voltage dependent time constant equations. By adjusting the parameters of the equations, we manipulated the model equations to result in high take off potentials by shifting the dependence on voltage. The results are shown the above sections for Luo-Rudy, BR, and Noble models. The hyperbolic tangent function suited our purposes for fitting and simplifying the equations, but it should be noted that other types of simplified functions can be explored. We are successful in adjusting the TOP, but a greater insight is that simplified equations, including hyperbolic tangents, polynomials, and exponentials can and should be used to reduce cardiac models while still retaining key characteristics and possibly reproducing added phenomena such as high TOP. Cardiac modeling has advanced research by providing for non-invasive studies, but certain aspects of its equations are unnecessarily complex to use as an analysis tool.

A limitation to this simplification is that we are changing the derivation of the model

equations. The original noble model arrives at the time constant and steady state equations by using first rate chemical kinetics, which designate the probability of a gate opening as α and closing as β . The time constant equation is therefore coupled to the steady state equation since they both depend on these probability rates. In this project, we decouple the equations, thereby making the model more phenomenological. We successfully reproduce the dynamics, but the underlying mathematics are less physiologically based. In the subsequent project, we utilize this technique to produce a novel, 2 variable model with unseen cardiac dynamics that lead to fibrillation.

CHAPTER 4

EXCITO-OSCILLATORY BEHAVIOR

In this section, we introduce a cardiac-derived model with novel dynamics in space. Our model's behavior deviates from cardiac researchers' focus on spiral wave and breakup, alternans, and ectopic pulses[19]. We introduce a route to fibrillation without the need of SWB. Rather, our model has both excitable and oscillatory behavior and produces oscillations in tissue that resemble boiling water "bubbles", whose appearance sustains chaotic behavior, shown in figure 4.1. In the sections below, we highlight the notable characteristics of our bubbly model, probe and interpret its dynamics, and connect it to cardiac dynamics.

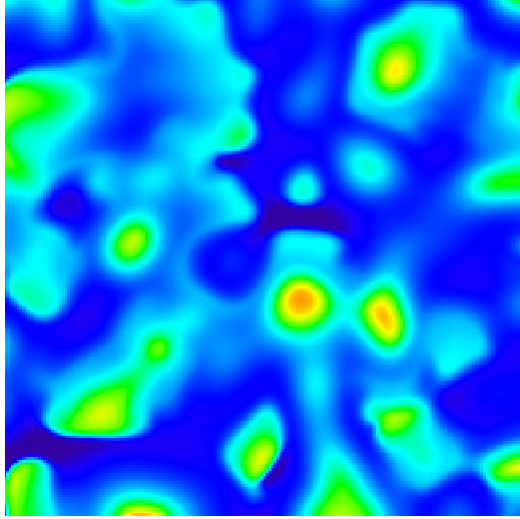


Figure 4.1: Tissue simulation of our bubbly model with 500x500 grid size time integrated 2000ms. Tissue is initially paced from left bottom corner at 99.5ms.

4.1 Experimental Evidence

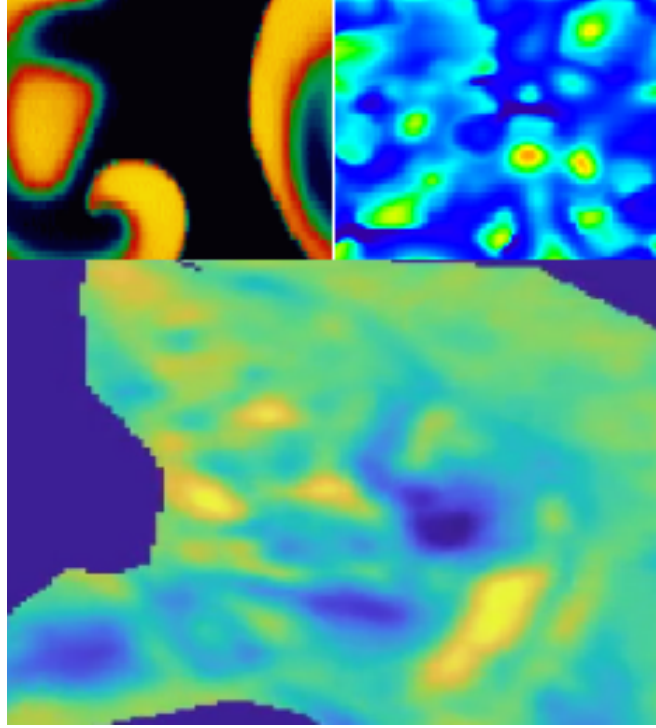


Figure 4.2: Top left image: spiral wave breakup in a tissue simulation[54]. Top right image: the bubbly model in a tissue simulation. Bottom image: experimental rabbit ventricle data showing more bubble-like oscillations than distinct spiral wavelets.

Spiral wave breakup, SWB, is an ubiquitously accepted mechanism for fibrillation in the cardiac community[55][26]. However, in certain cases, the cardiac simulations leading to SWB does not qualitatively mimic realistic behavior. During fibrillation in experiments, tissue excitation can be sporadic and be globular in shape rather than more distinctly wave-like curls, as shown in laboratory experimental data in figure 4.2. In the figure, we snapshot experimental rabbit ventricular data on the bottom, with the yellow color denoting regions of excitement. The shape and movement of the patterns of excitation for this case is qualitatively less similar to spiral wave breakup, in the top left of the figure, than our bubbly model, top right.

4.2 Model in Tissue Simulations

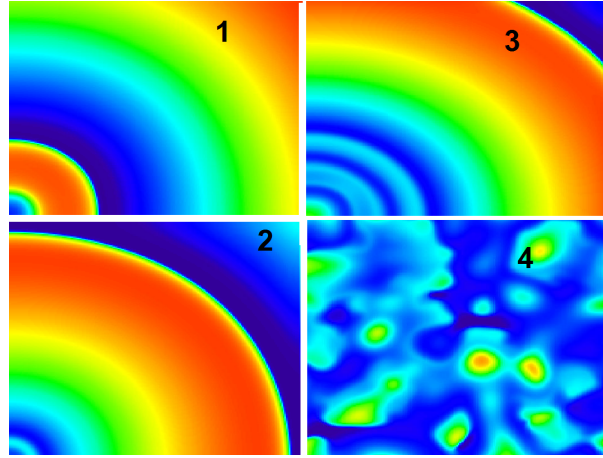


Figure 4.3: Progression of our bubbly model from steady state to chaos. Top left image: tissue is paced steadily from corner. Bottom left image: a wave ignites in the backwards direction, covering site of stimulus. Top right: subsequent waves eventually ignite forward and backward covering the tissue in curved stripes. Bottom right image: eventually stripes curve and round out, and bubble-like oscillations occur.

In figure 4.3, we begin with a two dimensional grid of size 500x500 and a steady pacing stimulus of 99.5ms, the model initially produces a series of traveling wave solutions. As the period decreases, at first the initial sets of waves are normal traveling solutions, in section 1 of figure. After the first two pulses in this simulation, the subsequent traveling wave ignites in the reverse direction, which we term tail-ignition. This type of reentry is differs from circular reentry in that no conduction block or dispersion of refractoriness is necessary, and no distinct spiral wave movement persists. Following the first tail-ignition, subsequent waves propagate in both forward and backward directions and submerge the entire grid with cells in various state of recovery(2). In time, the diffusion effects round out the curvature of small wavelets and circular spots of oscillation appear, which we term "bubbles"(4). When voltage is recorded at position [140,140], the AP is pictured in figure 4.4:

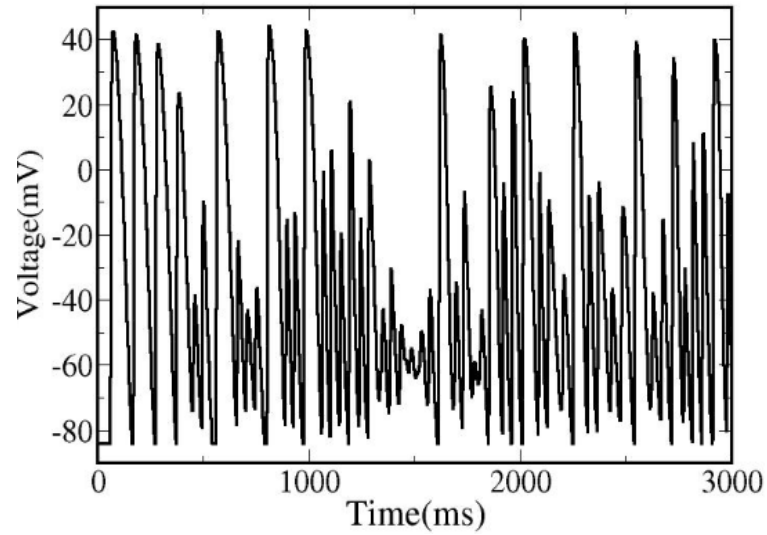


Figure 4.4: Image of our model with recording at a site in tissue simulation recorded in time series. TOP varies significantly and the time series is chaotic.

When the phase space trajectory of this cell is plotted, shown in figure 4.5, the oscillations have two distinct types, a small and large amplitude oscillation. The bubble-like excitations in tissue take place when the cell is at the state of the large amplitude action potential, and the remainder of the time spent in small amplitude oscillations.

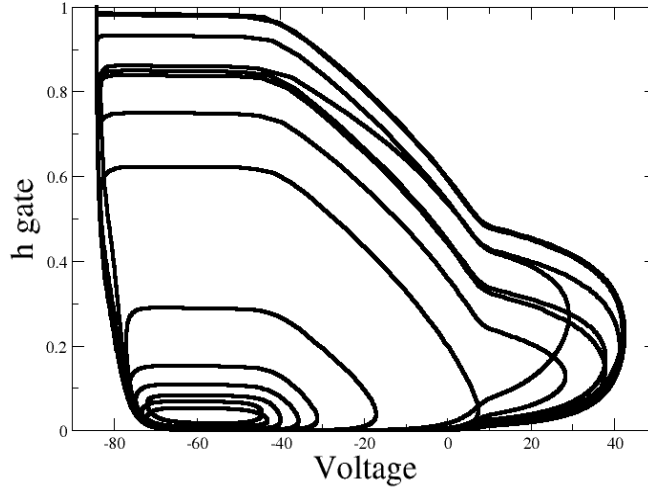


Figure 4.5: Phase space plot of a trajectory of our model from a signal from a location in tissue simulation. Y axis is h gate variable, and the x axis is voltage variable. System shows small amplitude and large amplitude oscillations.

4.3 Model Equations

Our model has two variables, v for voltage, and h for the recovery gating variable of the sodium. There are two currents, sodium and potassium, for the depolarization and repolarization. The parameter sf is a scaling variable to manipulate the APD.

Its sodium current is derived from the Beeler-Reuter model following the standard form of gating variables, with the gates m and h [47][56]. g_{na} is a constant, and e_{na} is the nernst potential. The j gate is removed to simplify the model, and the m gate is reduced to its steady state values. Furthermore, the steady state of the m gate is also reduced to a simpler equation that retains BR behavior. A notable difference between this model and typical cardiac models is that the time constant of the h gate, τ_h , is decoupled from steady state of the h gate, in the style given by the Chapter 3, Take-off potential section of thesis.

The potassium current is a time independent current proportional to voltage. As a simplification, it follows a monotonic relationship to voltage and it sets the baseline of

the resting potential to be -84mV . Through these reductions, the resulting model has two variables and easily manipulated, analyzed, and simulated.

$$\begin{aligned}
\frac{dh}{dt} &= sf\left(\frac{h_\infty - h}{\tau_h}\right) \\
\frac{\partial V}{\partial t} &= sf\left(D\frac{\partial^2 V}{\partial x^2} - I_{na} - I_k\right) \\
e_{na} &= 50 \\
g_{na} &= 3 \\
sf &= 0.38328 \\
I_{Na} &= g_{na}m_\infty^3 h(V - E_{na}) \\
I_K &= 5(1 - e^{-10(V+84)}) \\
m_\infty &= 1 - e^{-0.07(V+84)} \\
\alpha_h &= 0.126e^{(-0.25)(V+77)} \\
\beta_h &= \frac{1.7}{(e^{(-0.082)(V+22.5)} + 1)} \\
h_\infty &= \frac{\alpha_h}{\alpha_h + \beta_h} \\
\tau_h &= \begin{cases} 60e^{-(V+62.5)^2/98} + 0.7, & V \leq -15\text{mV} \\ 0.7 + \frac{3.8}{(1+e^{-1(V-10)})}, & \text{otherwise} \end{cases}
\end{aligned} \tag{4.1}$$

4.4 Phase Space Analysis of Excito-Oscillatory behavior

With a two variable model, we analyze trajectories in phase space. In the figure 4.6, we plot the nullclines of the two variables, voltage versus h . From the image, we observe that there are three fixed points in the system, a rest, saddle, and unstable oscillatory fixed point. We confirmed the nature of the fixed points by linearizing in the near neighborhood. The stable rest point identifies the system as an excitable system.

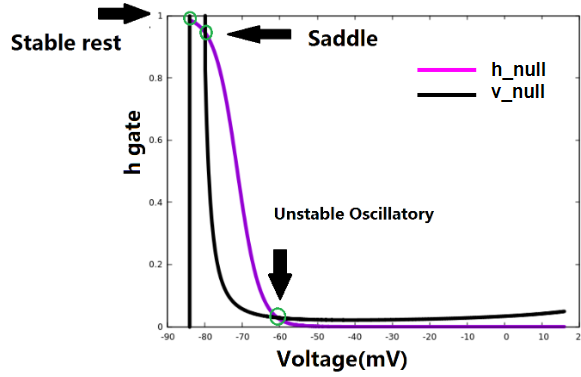


Figure 4.6: Image of the phase space and nullclines of our model, h gate versus voltage. The black line is the voltage equation nullcline, and the purple line is the h gate nullcline. The points circled in green are the fixed points of the system, including a stable rest, saddle, and unstable oscillatory fixed point.

A unique phase space behavior is the trajectories near the unstable oscillatory fixed point. Without pacing, when the initial condition is relatively close to the unstable point, the trajectory recovers, then self-excites once, and recovers to the rest if undisturbed. This trajectory is plotted in red in figure 4.7. When the initial conditions are farther away from the unstable oscillatory fixed point, the sequence of events where the system recovers then self excites does not occur.

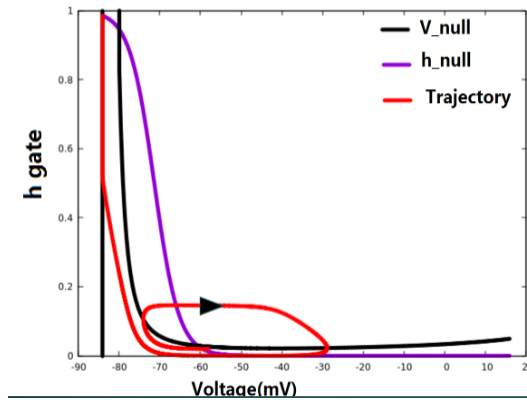


Figure 4.7: The trajectory of the system when initialized near the unstable oscillatory fixed point. This trajectory occurs with no stimulus, and it proceeds to recover, then self-excite once.

Even at the single cell, we note the coexistence of excitable and oscillatory behavior, and its effects are discussed in the following sections. In the following section, we will also

discuss two models, the Fitzhugh-Nagumo model and the Gray-Scott model. All three of the models, the bubbly model, FN, and GS have two variables and three fixed points under certain parameters[57][58][38]. Their behavior has striking similarities.

4.4.1 Ubiquity of 3 fixed points and Excito-Oscillatory behavior

Under certain parameter regimes, the Gray-Scott model, Fitzhugh-Nagumo and our model all have 3 fixed points of saddle, rest, and unstable oscillatory. Correspondingly, all have both excitable and oscillatory behavior in tissue simulations. The existence of the rest stable insures an excitable system, but the oscillatory fixed point adds complexity to phase space.

The Fitzhugh Nagumo model is a commonly used excitable model in cardiac research. While phenomenological, it reproduces properties of cardiac tissue such as spiral wave, refractory period, and alternans[58][38]. The Gray-Scott model is a widely used reaction-diffusion model of two diffusing species. Created in the 1980s, it is a flexible model capable of diverse phenomena such as waves, Turing patterns and repetitive moving patterns[57]. This model is widely used in various fields, such as chemical diffusing systems, and its ample variety of behavior is well documented in literature. Yet despite its complex spatial behavior, the model only contains two variables, which allows for nullcline and phase space analysis. This model is typically not used in cardiac dynamics. Yet, it is capable of small and large amplitude oscillations and tail ignition, like that of our bubbly cardiac model.

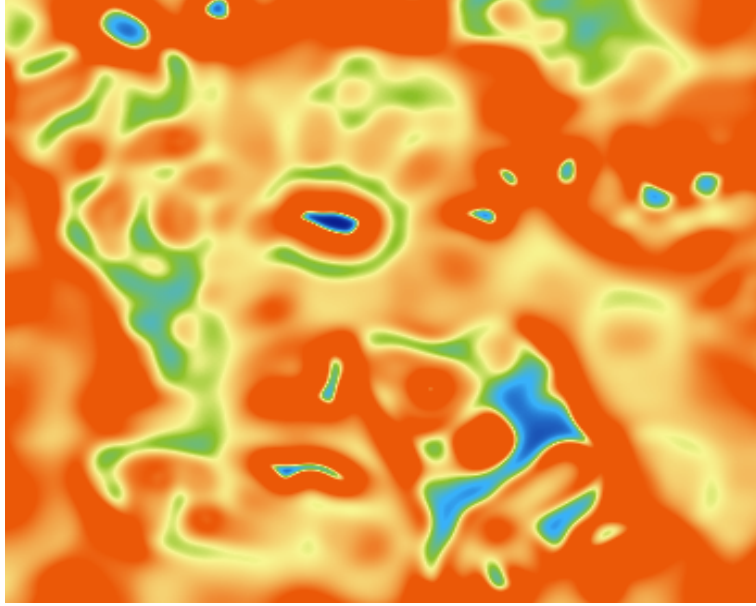


Figure 4.8: Tissue simulation of the Gray-Scott model with specific set of parameters. Dynamics show similar qualities to our bubbly model[59]. Simulations begins with an excitation from the left bottom corner

4.5 Elevated Take-off Potential

During fibrillation, the resting potential of electrical signals vary chaotically, shown in figure 4.9. In spite of this, a majority of cardiac models do not reflect this property, such as the Beeler-Reuter rabbit ventricular model and the complex Ten-Tusscher model, both of which have a relatively constant baseline even during VF[35], shown in 4.10. The contention with low TOP is that restricting the amplitude of oscillations to a large value reduces the complexity of solutions in phase space. By allowing for higher TOP, we allow for small amplitude oscillations and thus richer behavior in phase space.

For the bubbly model, the source of high TOP is the unstable oscillatory fixed point and its influence on its neighborhood in phase space. The sphere of influence of the unstable oscillatory fixed point is near all the trajectories that recover to rest. Slight perturbation from electrotonic effects in tissue simulation can change a recovering AP to a small amplitude excitation

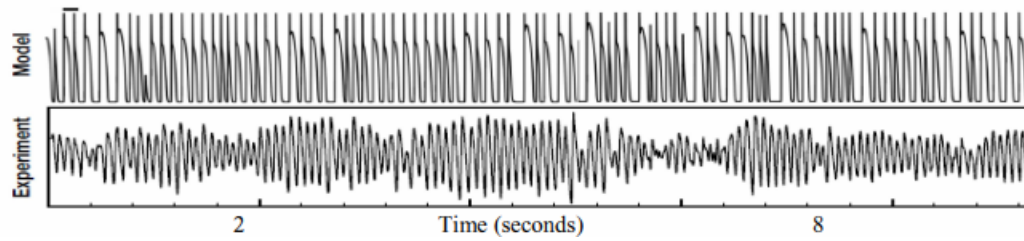
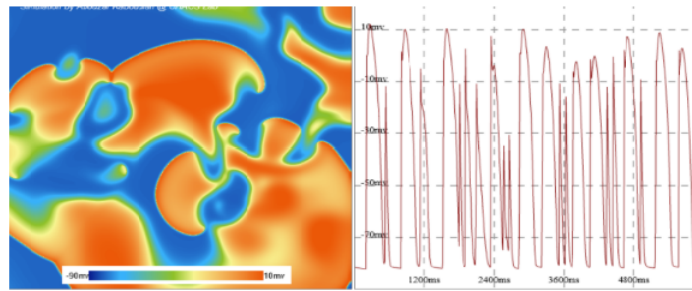


Figure 4.9: [50]An image showing Fenton-Karma four variable model in VF in above panel and experimental data showing VF in the bottom panel. A distinct difference is the lack of variation in the model's take off potential even during VF.

Beeler-Reuter



TNNP

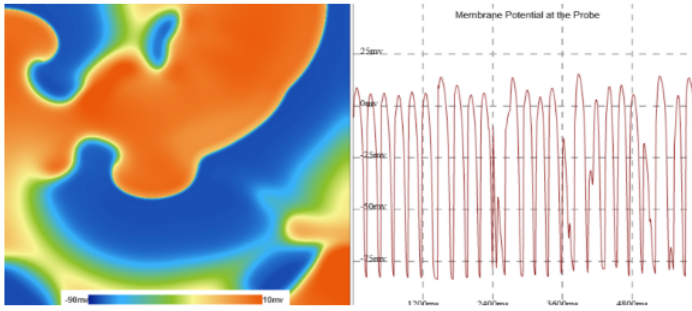


Figure 4.10: Top panel: left image is of tissue simulation of BR model in VF, right image is the electrical signal recorded at a site showing low take-off potential. Right image is of Ten-Tusscher tissue simulation in VF, the electrical signal is recorded at a site and shows low take off potential.

For a specific set of parameters for the Fitzhugh Nagumo model in tissue simulations, the author Gray notes that the presence of the unstable oscillatory point destabilizes the system and allows for not only high take-off potential, but also chaos[60]. In Gray's manuscript, the author notes that when the nullclines of FN are adjusted such that only

a stable rest point exists, spiral waves are stable in tissue simulations. When the nullclines are adjusted so that they match our model in number and type of fixed points, circular oscillations, high resting potential, and chaos ensues[60]. An image showing an example of high TOP is shown in figure 4.11.

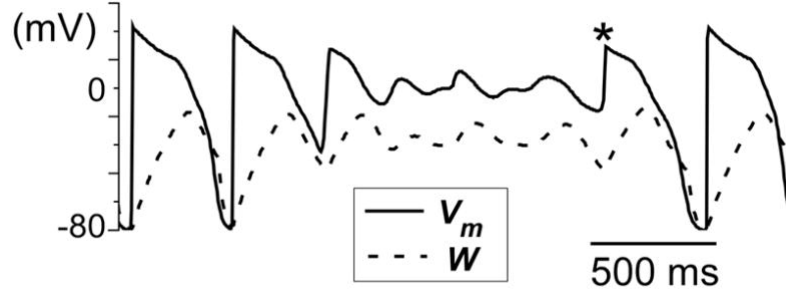


Figure 4.11: Solid line is the voltage and dashed line is the slow variable in FN model when simulated in tissue and undergoing chaos. The nullclines adjusted such that 3 fixed points exists[60].

The Gray-Scott model, when adjusted such that it contains an unstable oscillatory fixed point, has elevated and varying TOP when simulated in tissue as well. When the diffusion constant of the u variable is lowered, its behavior is strikingly similar to our model. In phase space, we observe unstable oscillatory behavior around the fixed points.

For all three models, we take note of the stability of the system in absence of the unstable oscillatory fixed point and instability when it appears.

4.6 Tail-ignition

A striking behavior of our model that typically precedes chaotic behavior is tail-ignition of the waveback. This phenomena ensures that even with regular pacing chaos will appear in a cable or tissue simulation of our model. We pace the model in a cable form at 99.5ms with no flux boundary conditions. The stimulus site are the first 100 discrete units. Initially, the system responds with steady pulses at first. Then, after the 3th or 4th pulse, the back of the wave ignites and re-excites the pacing site, as shown in 4.12 and 4.13, which are snapshots of the simulation in time progression. All subsequent pulses all ignite in both directions,

and the dynamics eventually becomes chaotic.

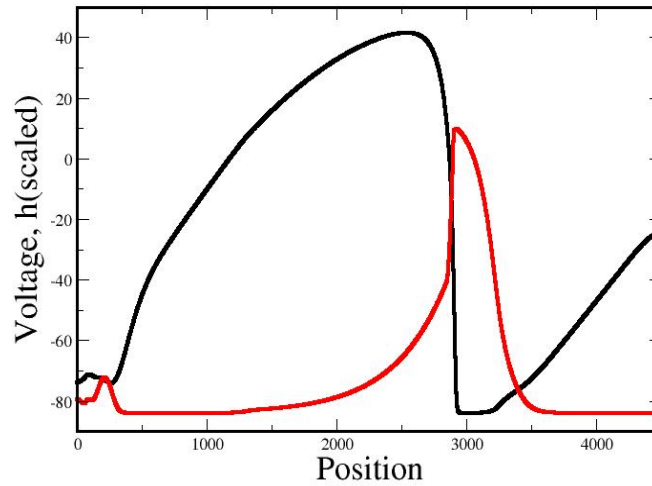


Figure 4.12: Our model in cable form with the x axis as position and y axis as voltage and h variable scaled. Image shows the conditions before tail-ignition. The focus is on the position between 100 and 500.

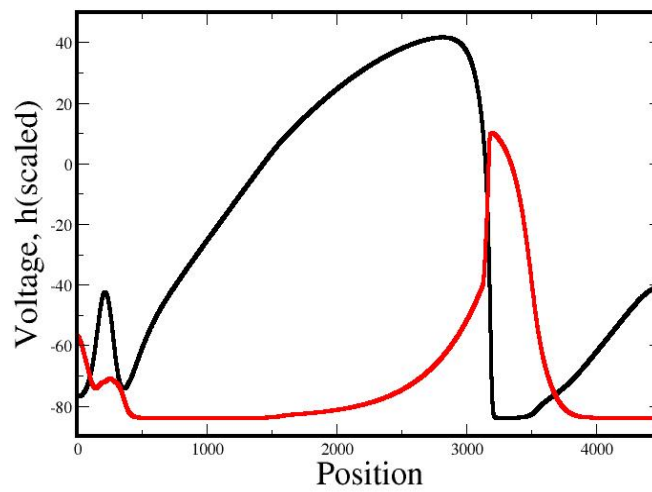


Figure 4.13: Our model in cable form with the x axis as position and y axis as voltage and h variable scaled. Image shows the conditions 10 ms after tail-ignition. The voltage signal between position 10 and 500 fires without a pacing stimulus.

This waveback behavior, when plotted in voltage time series, can appear to be Early-Afterdepolarizations or Delayed After-depolarizations in typical cardiac simulations. EADs and DADs are triggered responses following during the plateau or recovery phase of an AP. As a single AP passes, during recovery the window calcium or sodium current is strong enough to reverse recovery and re-excite. Here, we note that our model's behavior, while seemingly EAD-like, is not an EAD. For an EAD to occur, a preceding AP will trigger a secondary response. In our model, a single AP is incapable of triggering an EAD or DAD in single cell or in tissue simulations. Waveback ignition appears when the pacing period moves subsequent pulses closer to preceding ones. At threshold, it is the interaction of neighboring pulses precedes waveback propagation.

Both FN model and Gray-Scott model can produce wave-back propagation as well under certain parameter regimes[58][61]. When the GS model has similar nullcline behavior, a pacing site in the same region as our tissue simulation will produce a tail-ignition after the first few beats. Very similar to our model, subsequent waves propagate forward and backward and cover the tissue with bubble-like oscillations, shown in figure 4.14.

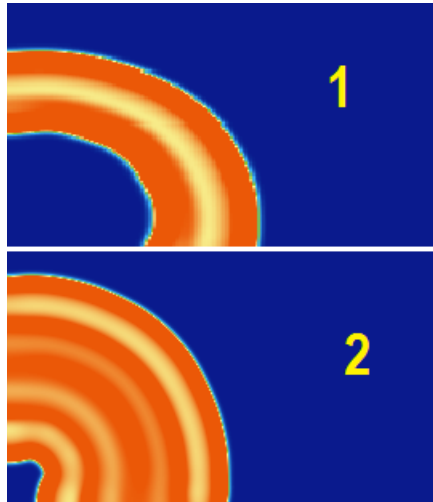


Figure 4.14: Image shows time snapshots of the Gray-Scott model paced in with a steady rate from corner. Initial pulse propagates[59], After initial pulse propagates, the waveback tail-ignites, similar to bubbly model[59].

For the FN model, Cytrynbaum notes the tail ignition behavior when the cable system is

tuned to a specific initial condition, an intrinsic unstable periodic orbit[61]. As the system is tuned closer to the unstable periodic orbit, it fires action potentials in both forward and backward indefinitely[61]. The difference between FN and our model is that while FN model can ignite backwards, the initial conditions must be acutely met to produce such behavior. For the bubbly model and GS, the tail-ignition behavior can be relatively easily produced, through regular or ectopic pacing[57].

4.7 Multistability

Our model is notably capable of multistable solutions when coupled in cable form. Without varying parameters except initial conditions, the bubbly model in cable can support multiple states of solutions, including a traveling wave or chaotic solutions.

To demonstrate the multistability of our model, we begin with a cable simulation with no flux boundaries conditions in a cable size of 3500 gridpoints, or 3500 cells. In the first case which produces chaotic solutions, we begin with asymmetrical initial conditions of the fast and slow variable, schematically illustrated 4.15. The cable is at rest except for explicit sections, where the V and h are not at equilibrium and symmetry is broken.

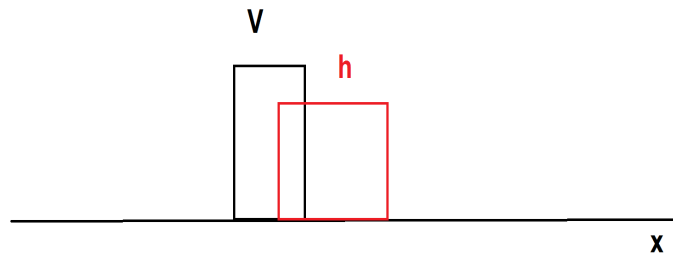


Figure 4.15: Initial condition of our cable, where the two variables are assymetrically profiled, thus resulting in chaotic solutions in the cable. This style of initial conditions is the same style of initial conditions as Cytrynbaum et.al.[61].

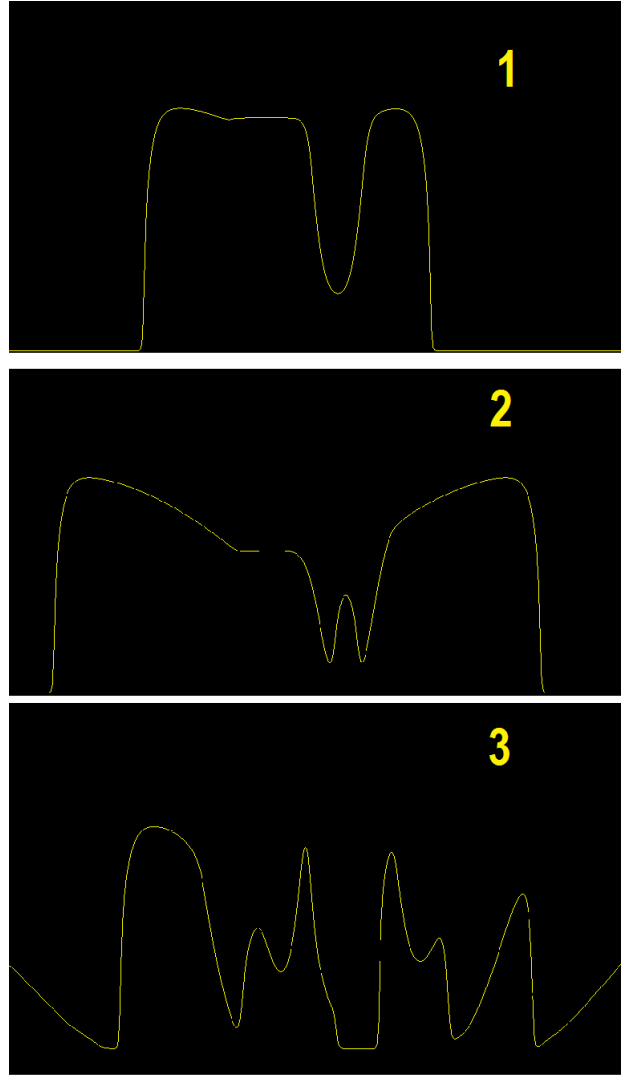


Figure 4.16: Time progression plot of the our model in cable form with the Cytrybaum initial conditions. Yellow lines indicate the voltage value at cable position. At the first time interval, the system produces two waves in opposite directions. In the second time interval, the wavebacks ignite, and by the third time interval chaos ensues.

When the initial conditions are evolved in time, two waves in opposite propagate initially, but then tail ignite in opposite direction, exciting the stimulus site. The stimulus site sends two waves in opposite directions, which in turn back propagates again. Eventually, cable system degenerates into a chaotic state, shown in 4.16.

In the second case, we begin the simulation with the following initial conditions, shown in figure 4.17.

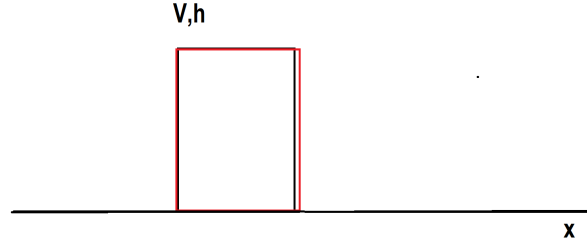


Figure 4.17: Initial condition of our cable, where the two variables are more symmetrically profiled, thus resulting in steady action potential solutions in the cable. This style of initial conditions is the same style of initial conditions as Cytrynbaum et.al.[61].

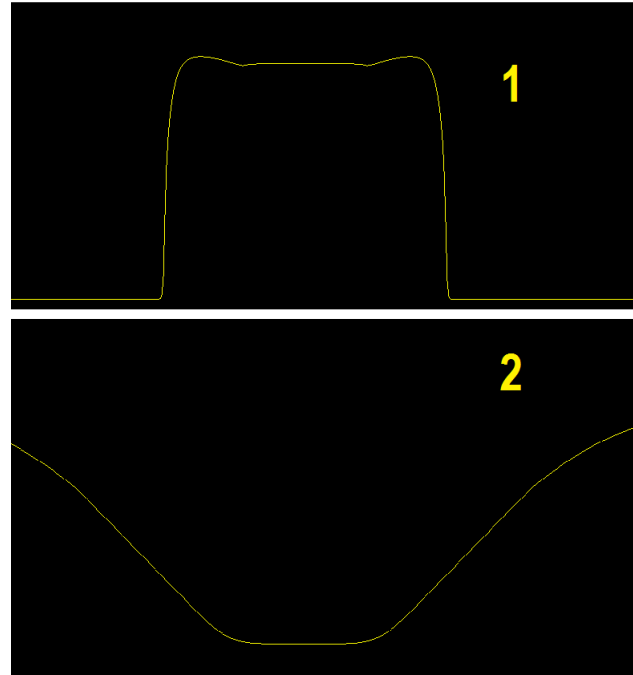


Figure 4.18: Our model's time progression in a cable with the same parameter values as previous trial except with symmetrical initial conditions. At the first time interval two waves propagate into opposite directions and by the second interval, they are sufficiently apart and non-interacting . No wavebacks take place, and the solutions remain steady traveling waves.

The system, with exactly the same parameters as the first case, produces stable traveling waves traveling in opposite directions with no back propagation, depicted in figure 4.18.

The two qualitatively different behavior with the exact same model and parameter values indicate the multi-stable nature of our excito-oscillatory model.

4.8 Chaotic Nature of our Model

In single cell simulations with periodic pacing, the bubbly model demonstrates chaotic behavior, and in this section we confirm the chaotic nature through poincaré section analysis.

4.8.1 Homoclinic Tangle

At the single cell level, we discern that chaotic behavior is apparent when we pace the cell at a decreasing period, plotted in figure 4.19.

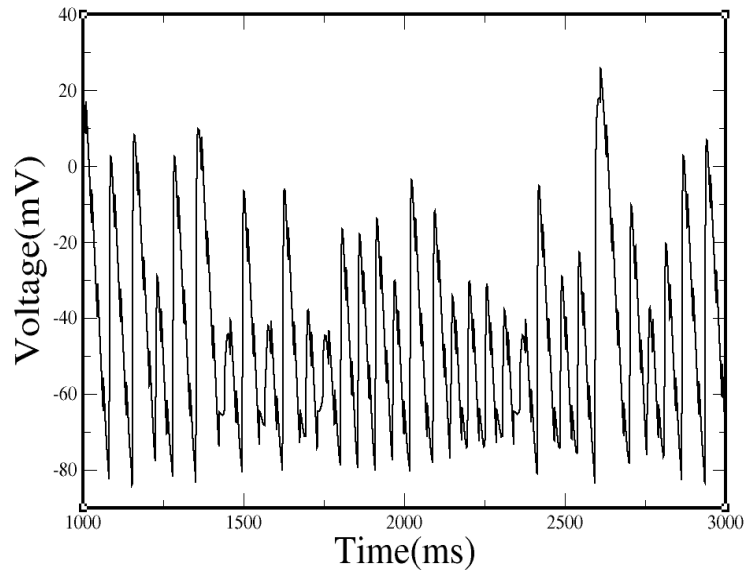


Figure 4.19: Our model paced model at single cell with $T = 18\text{ms}$. The image shows the voltage values in time series. A notable characteristic is the varying TOP, chaotic behavior time, very similar to voltage time series recorded in tissue simulations.

We note that for particular pacing periods at around 20ms and 50ms, the signal becomes chaotic.

In the image 4.20, we exhibit the APD value versus pacing period. For the model, chaotic behavior occurs at around 50ms.

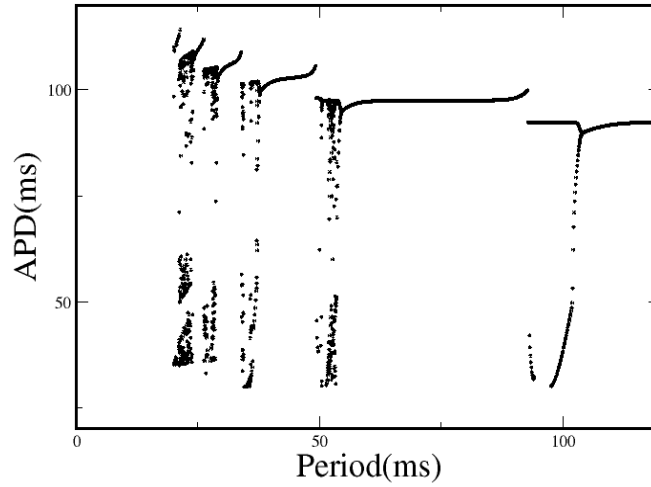


Figure 4.20: Our model in single cell is paced at different periods. The resulting APD is plotted against the corresponding period. Model shows multiple regions where the APD value becomes chaotic.

To further inspect the chaotic nature of our model, we search for periodic orbits in phase space and analyze their stability. The 3 time dependent variables are voltage, h , and periodic time due to pacing.

For pacing period 18ms , we next used a newton solver to search for periodic orbits, plotted in the image 4.21.

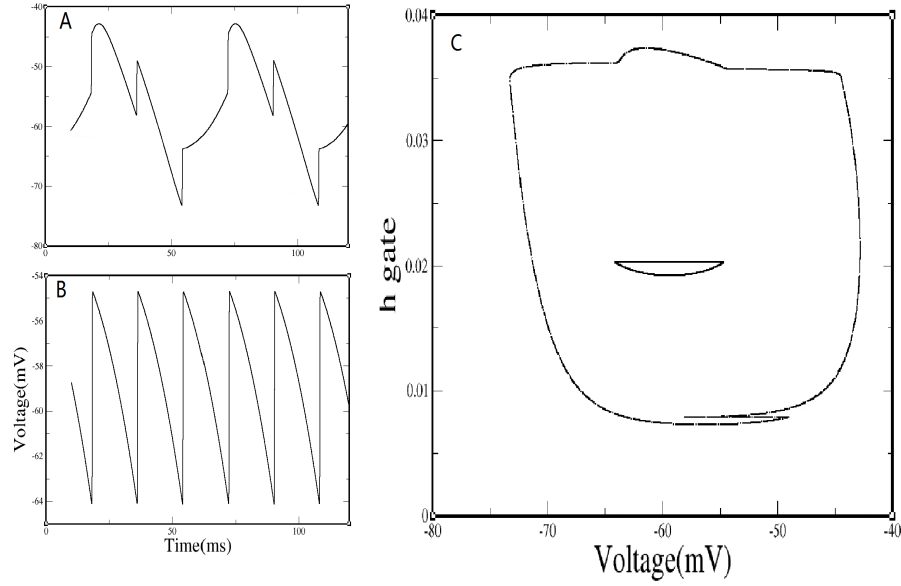


Figure 4.21: Panel A and B: periodic orbits in our paced single cell system, at 18ms, found through Newton root search with the top being a 3 cycle and the bottom being a 1 cycle. Panel C: the periodic orbits plotted in phase space.

Using poincaré section analysis, we insert a poincaré section at time = 10ms. The periodic orbit depicted in panel A of 4.21 is a fixed point on the section.

From our calculations we obtain the eigenvalues, $[31.6, 0.06]$, which indicate that the periodic orbit is a saddle on the poincaré section. Next we used newton solver to calculate the stable and unstable eigendirections and manifolds. In our model, the stable and unstable manifolds cross transversally in homoclinic orbits, shown in figure 4.22. This implies that the manifolds will cross infinite number of times and that there are an infinite number of periodic orbits within the system, which strongly indicates the presence of a chaotic saddle.

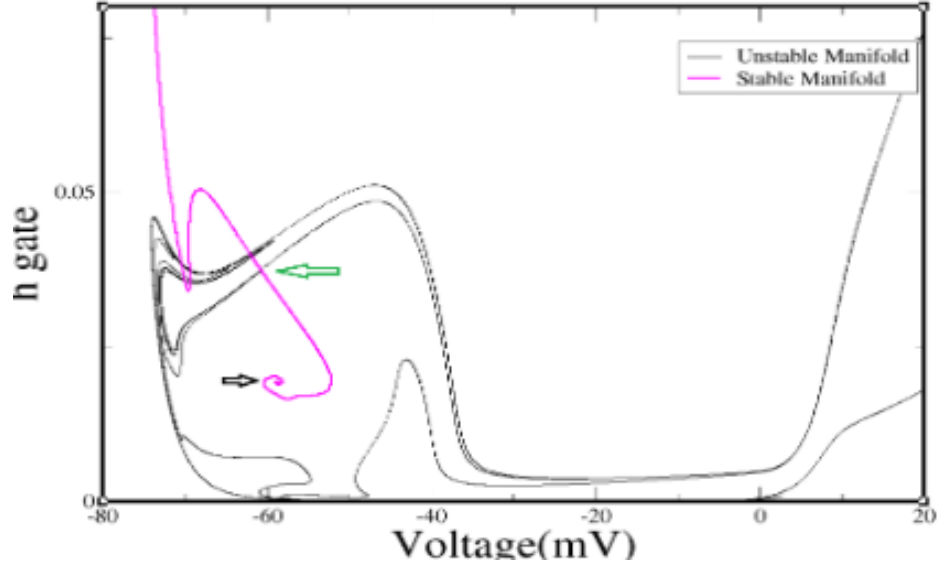


Figure 4.22: Poincaré section plot of a periodic orbit and its stable and unstable manifolds. Green arrow indicates the periodic orbit on the section, the magenta line is the stable manifold and black line is unstable manifold. Black arrow indicates a second periodic orbit on the Poincaré section.

4.9 Solutions in a Traveling Wave

We observe that the tail ignition behavior befalls when the pacing frequency is high and the distance between pulses shortens. At a certain threshold of pacing, the traveling pulse becomes unstable through tail ignition. To investigate the mechanisms for this instability, we numerically solve for the traveling wave solutions in periodic boundary conditions. To mimic a faster pacing frequency, we decrease the domain length with periodic boundary conditions, numerically calculate the pulse solution, and find its stability eigenvalues.

Using a Newton-Krylov solver, we calculated solutions for a domain size of 3500 cells in a cable with $dx = 0.00125$ and $dt = 0.001$. The solution is visualized in the figure 4.23.

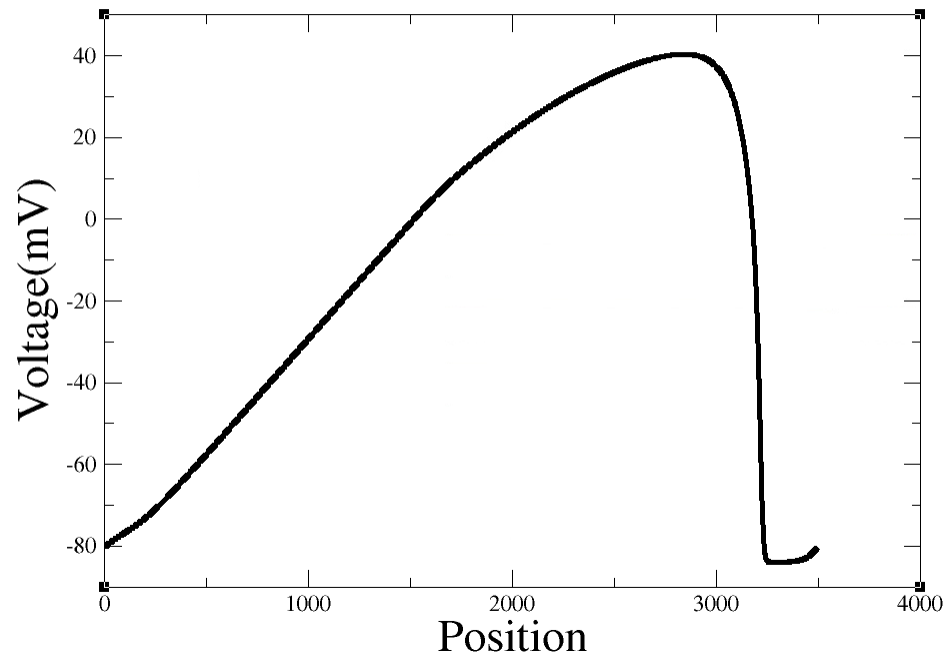


Figure 4.23: Figure shows the voltage versus position plot of the calculated traveling wave solution. Cable has 3500 discrete units with $dx = 0.00125\text{cm}$

When time integrated, the solution remains a steady traveling wave indefinitely, plotted in time series in figure 4.24.

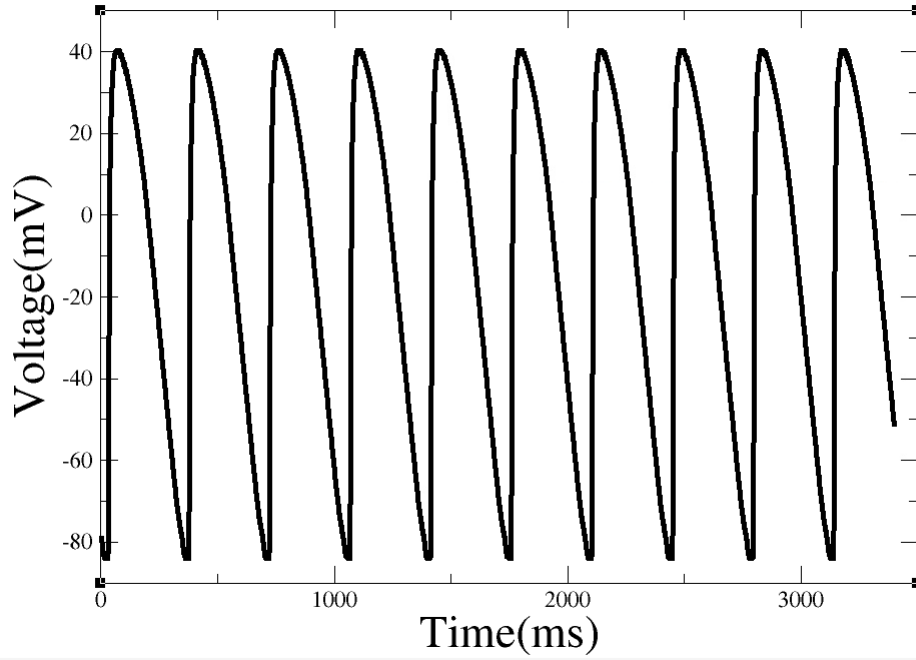


Figure 4.24: Figure shows the voltage time series of the calculated traveling wave solution with cable size at 3500 discrete units and $dt = 0.001$ ms. Image demonstrates the stability of the solution in time. Solution form persists without instability.

In the process of calculating the solution, we extract the stability of the pulse by constructing the upper Hessenberg matrix through the Arnoldi iteration. From this matrix, we calculate the eigenvalues to discern the stability of the solution. For the cable size 3500, the eigenvalues with the largest magnitude are smaller than 1, with real and imaginary parts, $[0.767 + 0.585i, 0.767 - 0.585i]$, which indicates a stable solutions.

4.9.1 Hopf Bifurcation of Traveling Wave Solution

As we decrease the cable size of the simulation during our calculation for the traveling wave solution, at a threshold domain size of 3400 discrete units, we calculate the solution and depict it in figure 4.25.

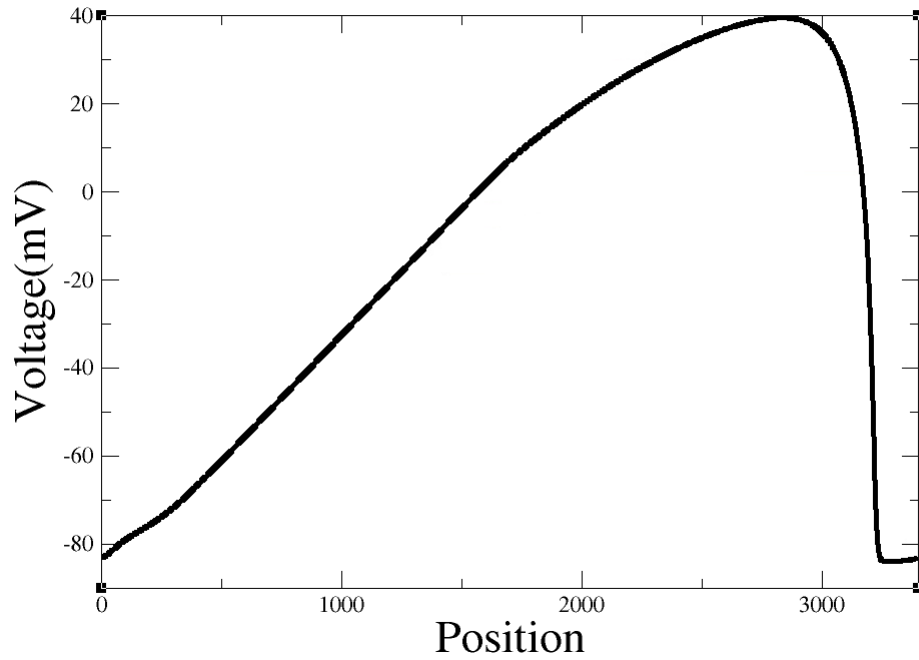


Figure 4.25: Image visualizes the voltage versus position of the calculated solution. Cable size is 3400 discrete units at $dx = 0.00125\text{cm}$. Y axis is the voltage, and the x axis is the position.

Using the upper Hessenberg matrix, we calculate the eigenvalues of the matrix, and we observe that the largest magnitude of the eigenvalues are now greater than 1, being $[0.793 + 0.641 i, 0.793 - 0.641 i]$

In a time integration of this solution, the dynamics indeed are unstable for the traveling wave. After a train of pulses, the traveling wave becomes unstable and a relative periodic orbit appears, visualized in time series in figure 4.26.

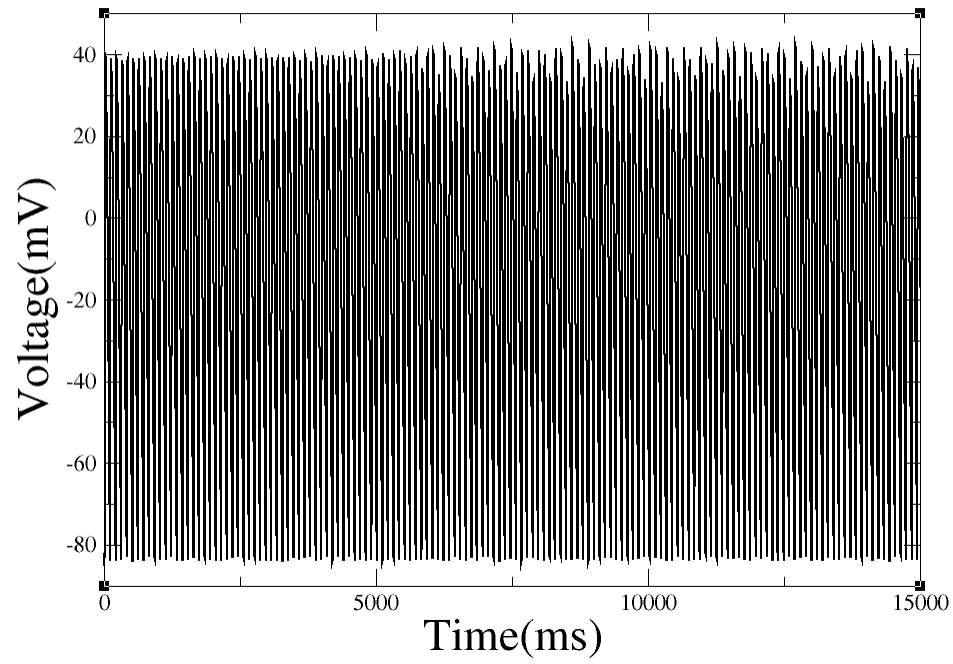


Figure 4.26: Plot shows time series of the action potential of a location in the cable with domain size 3400. $Dx = 0.00125\text{cm}$, $dt = 0.001\text{ms}$ Pulse evolves from stable traveling wave to a relative periodic orbit.

From the eigenvalues, we note that the values are complex conjugate pair, and the bifurcation is a Hopf bifurcation.

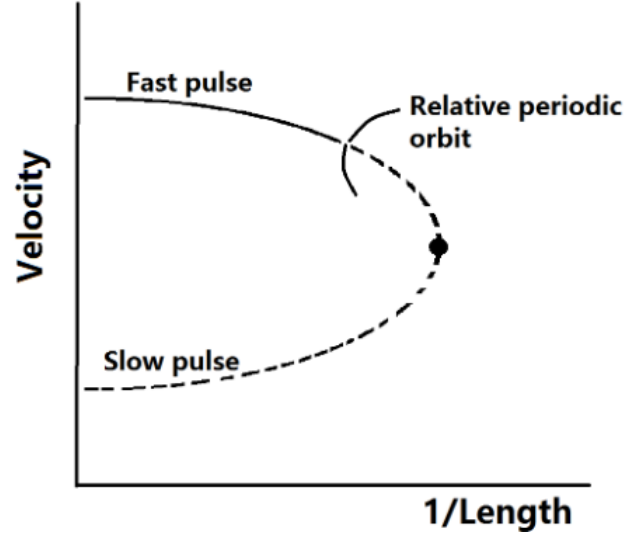


Figure 4.27: Image is of a schematic bifurcation diagram of the spatial solutions of our model in a cable form. Y axis is the velocity of a solution, and x axis the inverse of the length. Initially at relatively larger cable lengths, the solution is a pair of traveling waves. After the cable lengths decrease to a certain threshold, the traveling solution becomes unstable and evolves into an RPO.

In the image 4.27, we plot a schematic diagram of the cable behavior. Initially at a large cable size, the solution describes a fast, steady pulse. At the threshold domain size, the pulse solution becomes unstable and a relative periodic orbit appears.

4.10 Future Work

The transition from steady state to chaos travels through moving pulse to relative periodic orbit to turbulence. The next step in our research is to calculate the relative periodic orbit through Newton-Krylov solver and find its stability.

As a connection to electrophysiology, we observe that the relative periodic orbit appearance corresponds to spatially discordant alternans, or alternans with a traveling node, in cable form. As mentioned in the introductory section, SDA is arrhythmogenic in that the tissue becomes a substrate for unidirectional block and the initiation of arrhythmia.

4.11 Applications to Ohara-Rudy Human Ventricular Model

The Ohara-Rudy model is a relatively advanced human ventricular model with a large number of variables[36]. It is useful in simulations of drug effects on the human cardiac tissue. We observe that for cases where its I_{kr} , the potassium recovery current, is reduced, the model is capable of similar behavior such as tail ignition and bubble-like oscillations. Snapshots in image 4.28 depict a tail ignition behavior and oscillations instead of the typical spiral wave dominating the dynamics.

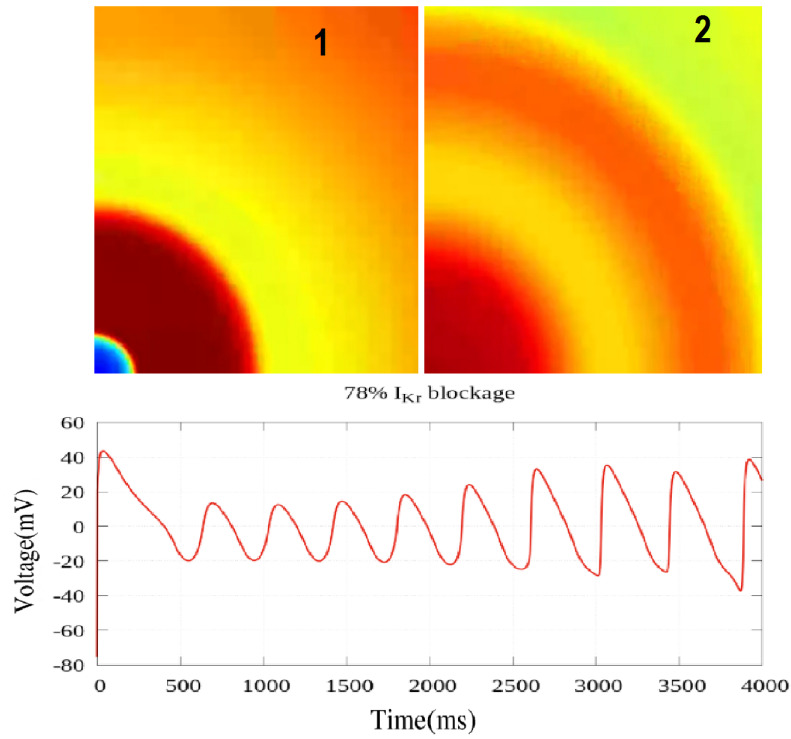


Figure 4.28: Image shows a progression in time of the O'hara-Rudy model of human ventricles with I_{kr} current at 78 percent of full magnitude. The progression of the model in tissue from left to right echoes similar characteristics as our model, the tail propagation and bubbles like oscillations[36]. The system is paced from the left bottom corner. Image 1 shows a wave that is moving in the forward direction towards the upper right hand corner. Image 2 shows the same wave firing in the reverse direction. Bottom panel is a signal recorded at site in tissue simulation. Data courtesy of Dr. Abouzar Kaboudian.

The O'hara-Rudy model is far more complex in structure and variable size than our

bubbly model. Thus, because our 2 variable model is computationally efficient and easily analyzed, we can use our model to understand fundamentals of tail-ignition and apply it to more complex models such as the O'hara Rudy model.

4.12 Discussion

We introduce a model which produces chaotic behavior without spiral waves or spiral wave breakup. Current cardiac research heavily emphasizes spiral waves, however, we demonstrate alternate routes to turbulence. Moreover, our model captures realistic aspects of fibrillation in figures shown in introductory section.

In tissue simulations, our model show tail-ignition behavior that induces a state where seemingly random circular excitation shapes appear. Even at the single cell level, our model produces chaotic behavior through regular pacing, and we confirm this through poincaré section analysis. We attribute the unique characteristics of our model, such as high take-off potential and tail-ignition, to the coexistence of excito-oscillatory behavior. Our model, like version of Gray-Scott and Fitzhugh Nagumo has both a stable rest and an unstable oscillatory fixed point, which together renders the system sensitive to perturbations. Our work can be applied to cardiac dynamics through its striking similarities to the O'hara Rudy ventricular model. For future work, we will calculate the relative periodic orbit that appears in a cable and find the threshold at which it becomes unstable.

CHAPTER 5

CALCIUM ALTERNANS

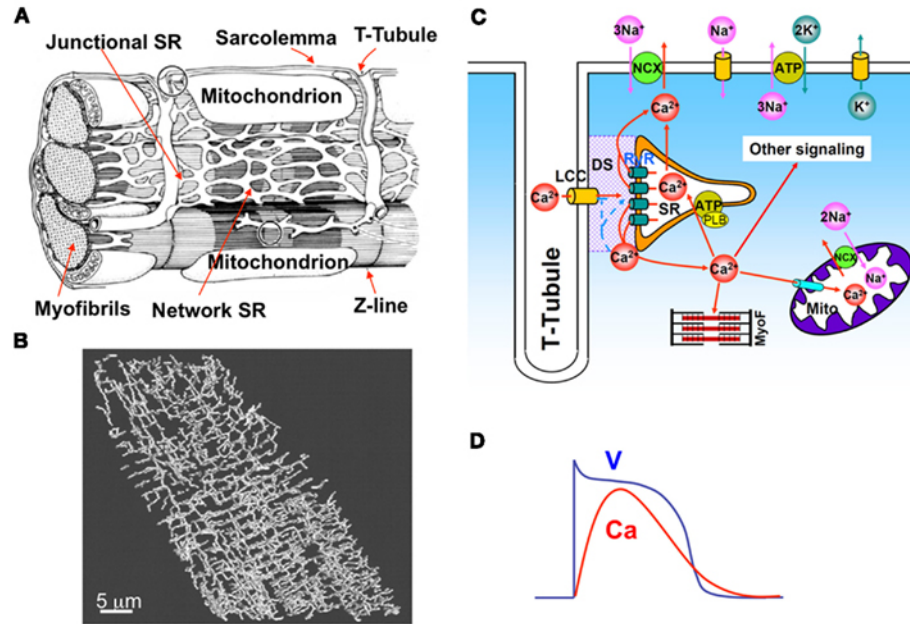


Figure 5.1: [62]Panel A is a detailed diagram of the contractile system in a cardiomyocyte, showing sections of the SR and T-tubules, alongside myofibrils that contract for the heart to pump blood. Panel B visualizes the T-tubules structure in a rat ventricle, showing the intricate and three dimensional structure. Panel C is a schematic diagram of the local calcium release unit. Panel D is an example time series of the action potential and calcium release amplitude, showing the approximate time scales for each event.

Acute regulation of the calcium system is vital to the function of the heart[12]. Excitation-contraction coupling, in which an action potential elicits calcium release which in turn binds to troponin protein complex and allows for the initiation of contraction, is one of the fundamental cardiac relationships. For ventricular non-pacemaker cells, the majority of calcium is released intracellularly, which allows the cell to contract and then relax back to equilibrium[17]. Therefore, timed coordination between adjacent myocytes, calcium release units, and the action potential currents is essential[12].

The calcium cycling system mirror the electrical system in that the two systems are capable of alternans and chaotic dynamics. Under clamped voltage conditions, experiments convincingly demonstrate calcium alternans independent from the voltage system[63]. Furthermore, the two systems can synergistically induce instability bidirectionally[33]. If an instability originates in one system, it can be amplified through the interaction with the other. During arrhythmia, this property leads to difficulty in pinpointing the source of arrhythmia.

Growing evidence indicates that a majority of arrhythmia may be due to the calcium cycling instability rather than voltage, especially when alternans occur when the APD restitution is flat[64]. Unlike the voltage system, however, the calcium cycling has greater complexity spatially within one cell[39]. While a cardiac myocyte may be approximated as a single voltage unit, within one cell there are thousands of localized calcium release units[39].

A multitude of calcium models exist. However, phenomenological calcium models that capture salient characteristics such as graded release, mechanism of calcium instability, and calcium bidirectional coupling are few[65]. In this section, we introduce a minimal phenomenological calcium model capable of the key properties of calcium dynamics, most specifically in calcium alternans and its effects on voltage. We fit this model to experimental data and demonstrate its utility for analyzing the origin of cardiac instability.

5.1 Calcium Release Unit and Calcium Cycling

A typical ventricular calcium release unit(CRU) is schematically pictured in figure 5.1, panel C. In a CRU, bundles of actin and myosin fibers are striated periodically. During calcium release, calcium ions bind to the contractile machinery that causes the fibers to move in a criss-crossed fashion to contract the cell[17].

Wrapping around the fibers are sarcolemmal membrane invaginations into the cell, called T-tubules, which serve as even distributors of calcium currents, shown in figure 5.1

panel B. In the cell next to a T-tubule, a section of the SR of the cell stores the calcium ready for release[17]. The junction between the T-tubule and the SR is termed the dyadic space, where calcium currents interact with receptors on the SR[17].

A ventricular calcium cycle begins with the action potential raising the transmembrane voltage, and during the plateau phase, the L-type calcium(LCC) current enters the cell through the T-tubule channels. As this occurs, the dyadic junction's free calcium concentration increases, which opens the Ryanodine receptor gates, or Ryr gates, on the JSR terminus[66][67]. As these clusters of gates open, relatively large amounts of calcium is released into the cytoplasm, a phenomena termed calcium induced calcium release, or CICR[68]. The sum of the clusters of release is termed the calcium transient, and the timing of the AP and the calcium release are depicted in figure 5.1 panel D.. As the cytoplasmic calcium concentration rises, it binds to the contractile machinery of the sarcomere, and precipitates shortening the cell. Following the release current, the SERCA pump removes calcium from the cytoplasm and return them to the SR. The sodium-calcium exchanger protein in the cell membrane removes the L-type calcium ions.

5.1.1 Calcium Sparks

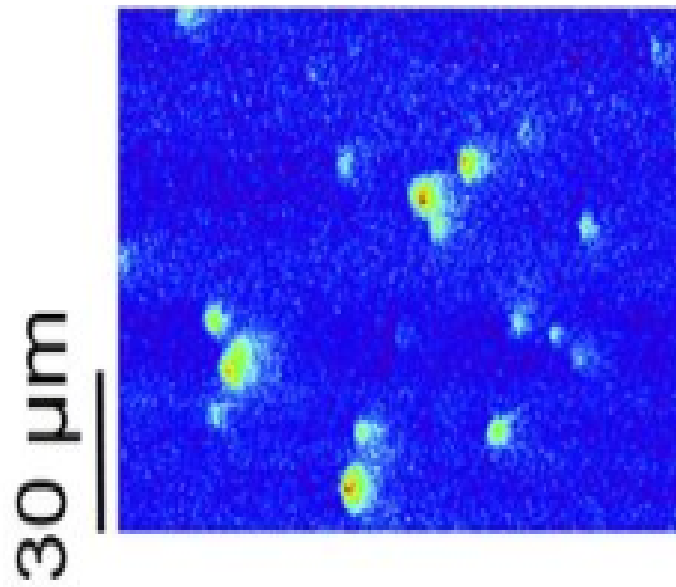


Figure 5.2: Illustration of spark phenomena through a line scan of a cardiomyocyte that is producing calcium sparks. Bright yellow and red spots represent these local excitations while the rest of the system is at rest [69].

The ventricular calcium system in one myocyte is estimated to consist of 20,000 discrete units of release, also known as CRUs[70]. Calcium is released from each CRU, they are buffered relatively quickly and locally, resulting in a phenomenon which researchers term a calcium "spark"[71][72], or a local spike in free calcium concentration, shown in figure 5.2. Sparks are generally elicited both by LCC induction and spontaneous firing. Free calcium ions in high concentration are toxic to the cell, thus, when calcium is released in the cytoplasm, they are buffered relatively quickly, resulting in slow diffusion of ions across the cytoplasm and the localized nature of calcium dynamics.

Unlike the voltage system, which has a nonlinear response to stimulus, the calcium system is graded in release due to its localized nature of sparks. In general cases, the larger the LCC current, the more sparks, and the result is graded release of calcium into the cytoplasm.

5.2 3 Important Properties for Calcium Alternans

Multiple mechanisms lead to instability within the calcium cycling system. In the past, the different mechanisms seemed to contradict one another, but was ultimately summarized in the unified theory of calcium alternans by Qu et al[70]. Qu named this theory the "3R theory", where the three major properties of calcium dynamics are discussed and related to calcium alternans[70], and also derived a comprehensive return map to unify the major mechanisms of calcium alternans.

5.2.1 Randomness

Calcium release units fire stochastically with a probability constant. Because of the randomness of the sparks, the system can be approximated into a one-body problem with mean field theory, where the amount of CRUs firing in our model is proportional to the probability of firing. These sparks are termed "alpha sparks"[70].

5.2.2 Recruitment

An alpha spark is generally localized to its own CRU. However, in cases where the release from a CRU is relatively large, the calcium release can diffuse to neighboring CRUs and elicit "secondary sparks"[17]. A major factor in secondary sparks is the increase in SR calcium level before the next release, also known as the load, as it leads to a larger local release. The amplitude of calcium release per spark is related to the gradient between the SR calcium load and dyadic calcium concentration. If the load is larger, the release flux will be larger and is more likely to diffuse to surrounding CRUs and recruitment for secondary firing[70].

5.2.3 CRU Refractoriness

Subsequent to a CRU firing, a period of refractoriness follows. Ryanodine receptor gates(Ryr) that let calcium through, though they are sensitive to SR calcium alternans, are observed to have their own opening probability and time constant for recovery. Though their role in calcium release is still unclear, it is known that manipulating sensitivity to SR luminal calcium affects the opening and closing of Ryr gates[73][74][75], or in other words, the higher the SR load the higher probability of Ryr gates opening, and the more quickly the time constant of recovery. Depending on the pacing period, the fraction of Ryr that are ready to fire vary before the next beat. The larger the fraction, the greater the release[73].

5.3 Mechanisms of Calcium Alternans

Two main mechanisms of calcium alternans are generally accepted in the cardiac community currently. The first is the release-load relationship concluded experimentally by Diaz et.al.[76][45], which is a return relationship between the previous load(SR) value and the subsequent release. The second mechanism is founded on the refractory period of the CRU after spark release.

5.3.1 Release-Load Mechanism of alternans

Diaz et. al. produced experimental data that demonstrated the nonlinear dependence of calcium release per beat on the load prior to release[76][45]. In the image shown in figure 5.3, the release's functional relationship is initially steady, but then sharply increases at high load. This property is due to the recruitment characteristic of calcium. Though sparks are generally local phenomena, if the spark release is large enough and the coupling distance between CRU's is sufficiently close, secondary sparks can follow primary sparks. Moreover, mini-waves of calcium release can take place if the load is high enough[77]. Because of this nonlinear relationship, if the load is at a very high value, the release can

be abnormally large. The next beat, however, will have a small release because the uptake machinery did not return a large fraction of the calcium back into the SR, shown in figure 5.4. However, after this beat, a large release will occur again because the system will have had two beats to recover the SR load again. Depending on the pacing period, this alternation can perpetuate and induce instability.

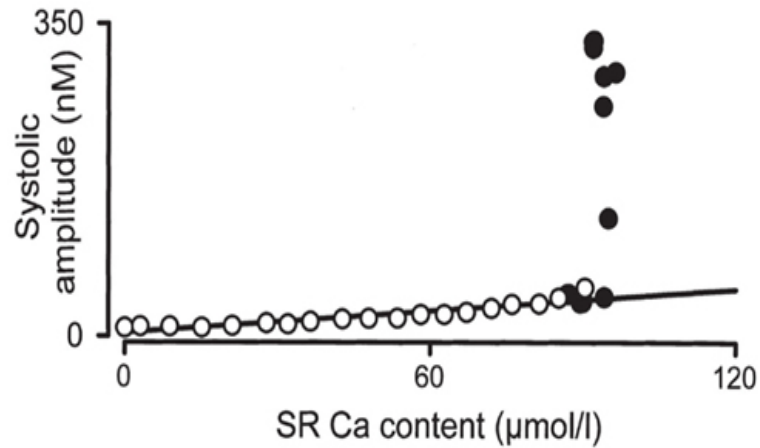


Figure 5.3: Figure depicts the highly nonlinear release-load relationship that is a mechanism for calcium transient alternans. The y axis is the calcium transient amplitude and the x axis is the SR calcium load before the release. For a larger SR load, the following release current will be exponentially larger[45].

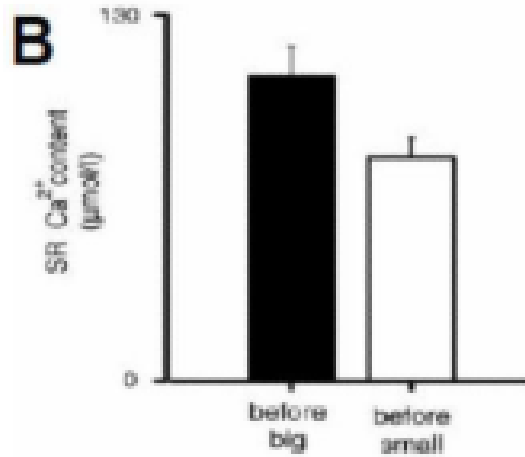


Figure 5.4: Experimental evidence from Diaz et. al. shows the relationship between cytoplasmic calcium release amplitude and SR load before large and small release beats. Before a large release, it has been shown that the load is large. On the other hand, before a small cytoplasmic calcium release, the SR load is measured to be small[45].

5.3.2 Calcium Release Unit Refractoriness

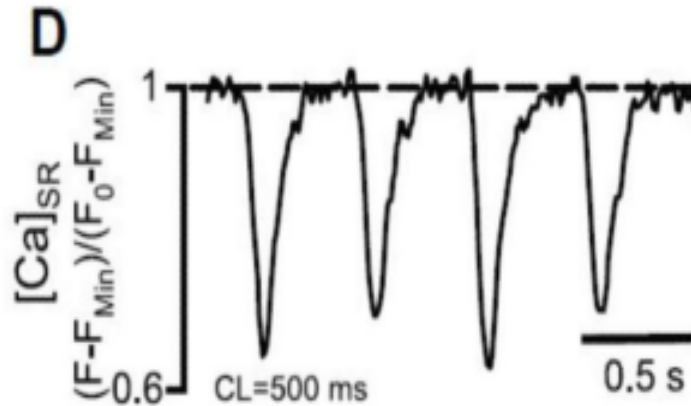


Figure 5.5: [73][78]Experimental data of SR calcium concentration demonstrating that alternans in calcium cycling can occur despite lack of alternans in the loading value before the next release. Y axis is SR calcium content, and x axis is time in seconds.

This mechanism lies in the refractoriness of the CRU after firing[73]. Depending on the length of the refractory period, a CRU may enter alternans mode if for the pacing period the fraction of RyR recovered alternates as well. For a particular beat, if the pacing cycles shortens, the RyR only partially recover, which results in a smaller release in the subsequent beat. After this, a larger fraction of RyR recover, which will lead to a larger release. The beat after this will have a smaller release due to a large number of unrecovered RyR, and so on in alternating form.

In early studies of calcium alternans, the mechanism seemingly contradicted the accepted release-load mechanism because load is not necessarily alternating in this case[70]. Experimental data exhibited in figure 5.5 have shown that alternans in calcium transient amplitude can occur despite lack of alternation in load.

5.3.3 Bidirectional Coupling

In cardiac systems, the transmembrane voltage is coupled to the calcium system through the L-type and sodium calcium exchanger currents. Voltage can influence calcium through APD prolongation, and the inverse can occur as well. This bidirectional coupling is a source of mutual influence and creates difficulty in investigating the origin of cardiac arrhythmia[79].

In the voltage to calcium direction, graded release coupling is present. If the previous APD is long, the current DI is short and the recover of L-type channel gates is less than the previous beat. The subsequent beats L-type magnitude is smaller, and thus the calcium release is smaller, shown in figure 5.6 top panel. On the other hand, the calcium system can influence the voltage in two main manners, positive and negative coupling. If the calcium transient is large, the sodium calcium exchanger will flow inward with sodium and outward with calcium leading to a net inflow of positive charge, which can lengthen the APD. For negative coupling, the calcium transient is large and it inactivates the L-type calcium current, which shortens the APD, visualized in figure 5.6 bottom panel. Depending

on which current's effect is stronger, the calcium coupling favors positive or negative.

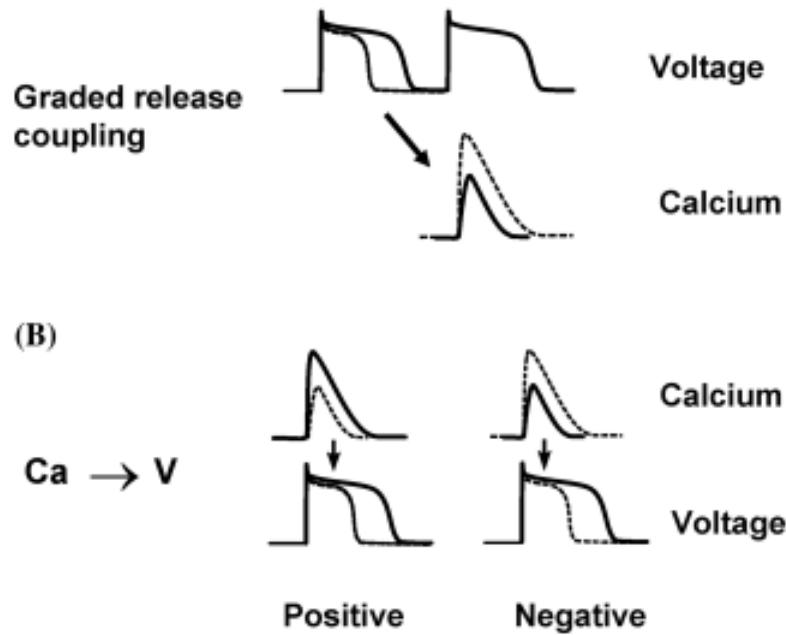


Figure 5.6: [79]An illustration of the bidirectional coupling between voltage and calcium systems. Voltage affects the calcium through the graded release mechanism. If the system has a longer DI, the L-type calcium current will be larger, the calcium release will be correspondingly increased. Calcium couples and influences the APD of voltage through the transmembrane calcium currents. If the calcium transient is large in amplitude, the L-type calcium current will be inactivated earlier calcium sensitive gates. On the other hand, if the calcium transient is large, the sodium calcium exchanger will remove a calcium ion for 3 sodium ions, which increases the inward current and thus the APD.

5.4 Calcium Modeling

Models for calcium cycling diverge in dimension size and character. Early versions of calcium modeling, prior to the discovery of the spark phenomena, depicted a "common pool" version of modeling, where the calcium system is not discrete units in one cell but one pool of calcium that releases currents due to a stimulus. Following stern the sparks phenomena is more readily captured in models[72]. In the following section, we describe prototypical examples of qualitatively different calcium models.

5.4.1 Luo-Rudy model

The Luo-Rudy model was published in 1991 and again 1994[53][80]. Its calcium cycling system consists of the LCC calcium current, sodium calcium exchanger, and its SR is compartmentalized into two sections. This model is a common pool model and does not capture graded release, the release-load, and CRU refractoriness. While this model can be tuned to fit experimental data, the fundamental principles in which it is created is not accurate[53][80], especially with the the lack of graded spark release.

5.4.2 The Shiferaw model

The shiferaw model published in 2003 is a relatively minimal model that captures graded release, release load mechanism, and transmembrane and intracelulluar calcium dynamics. Unlike the Luo-Rudy 1994 model, it captures graded release through a phenomenological current, I_{rel} , that is directly proportional to the L-type calcium current. This proportionality mimics the spark phenomena, in which the more L-type calcium current enters, the more sparks release calcium into the cytoplasm[65].

$$\frac{dN(t)}{dt} = gI_{ca}A(c(j')) \quad (5.1)$$

In the equation above, N is the number of calcium sparks occurring at time t , and the rate that N changes is proportional to the I_{ca} , the l type calcium current. The release current I_{rel} , the sum of all the sparks, is proportional to $\frac{dN(t)}{dt}$ [65].

Furthermore, Shiferaw divides the cellular space into 4 distinct areas, JSR for the SR membrane near the T-tubules, NSR for the bulk SR, Cs for submembrane and dyadic space, and Ci for cytoplasm calcium concentration, which correctly mirrors the large difference in concentration of calcium between different areas of the cell.

One notable characteristic that Shiferaw does not explicitly highlight is the CRU refractoriness of the cell. Experimental data demonstrate alternans even when the load is not

changing. This property is important for alternans bifurcation, and we will include this in our model.

5.4.3 The Nivala model

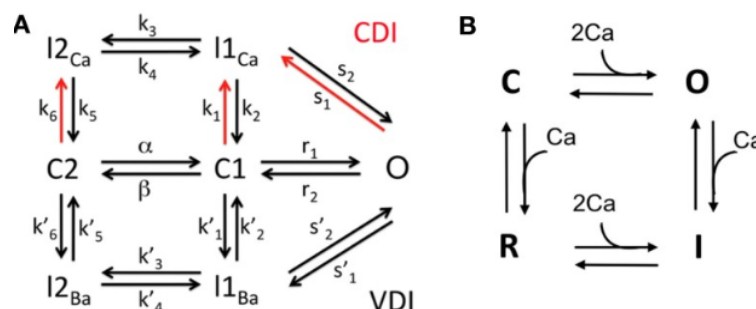


Figure 5.7: [62] A diagram of the markovian style of modeling in Nivala 2012. LCC variable(A) and RyR(B) transition between various states with certain rates. The k 's indicate transition rates, while "C" and "O" indicate closed and open states for the gating variables.

The Nivala model is a 3 dimensional, compartmentalized, and stochastic model which carries the major characteristic of calcium dynamics[62]. The model equations have both Hodgkin-Huxley and Markovian forms. The L-type calcium channels are no longer represented as gates that are either "open" or "closed", but rather as a gate transitioning between multiple conformations with probabilistic rate constants, shown in figure 5.7. The stochasticity is implemented through Gillespie's Method, a variant of Monte Carlo[62]. Because of the high number of equations and parameters. Simulations of voltage is difficult in itself in large scale, and the calcium dynamics only add to the complexity. Furthermore, in a cardiomyocyte there are on the order of 10^4 junctions[81]. With the numerous Markovian equations and stochastic methods, computation on a large scale with hundreds of cells is not practical nor is it useful for understanding the overall dynamics of the system during VF.

5.4.4 Minimal Model of Calcium Alternans

We propose a minimal phenomenological model of calcium instability that captures the main mechanisms of alternans, bidirectionally couples to voltage, and captures salient properties such as graded release. Additionally, our model is relatively easy to understand and computationally tractable. We aim to capture different forms of calcium and voltage alternans as well. Our model draws inspiration from the Shiferaw calcium model[65].

We divide the CRU into two compartments, cytoplasm and SR, and give calcium concentration variables to each, C_{cyto} and C_{sr} . Two variables represent the two alternans mechanisms, r for CRU refractoriness, and q , for the release-load mechanism. To capture sparks leading to graded release, we define a variable, n , that denotes the number of spark occurring at time t . Our last calcium variable is the inactivation gate f in the L-type calcium current. In the figure 5.8, we schematically delineate our model. Four currents, of which the equations are combinations of the variables, influence the dynamics. I_{rel} and I_{up} change the calcium concentration in the SR, and the I_{ca} and I_{naca} change the cytoplasmic calcium concentration. Finally, we simplify the L-type calcium and I_{naca} greatly into intuitive forms.

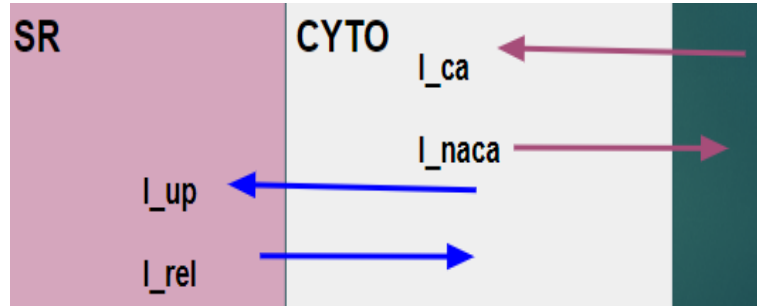


Figure 5.8: Schematic diagram of our two compartment model. The two compartments are the sarcoplasmic reticulum(SR) and cytoplasm(CYTO). The currents that affect each compartment are also visualized above. Uptake and release contribute to the SR calcium concentration, and the L-type calcium current and Sodium calcium exchanger affect the cytoplasmic calcium transient concentration.

5.4.5 Model Equations

The model equations are given below: For the calcium system, there are 6 state variables. R and q gates for the two main mechanisms of calcium alternans, C_{cyto} and C_{sr} for the SR and cytoplasm calcium concentrations, and f gate for the L-type calcium current I_{ca} .

$$G_{rel} = 0.005 \quad c_{up} = 0.003$$

$$b_{ncx} = 0.83636 \quad m_{ncx} = -0.02182$$

$$m_{ca} = -0.4 \quad b_{ca} = 13$$

$$k = 1/26 \quad g_{ca} = -200$$

$$c_{an} = 0.0001 \quad \tau_q = 30$$

$$d_{\infty} = \frac{1}{1 + e^{\frac{-V-20}{6.24}}}$$

$$f_{\infty} = \frac{1}{1 + e^{\frac{V+40}{8.6}}}$$

$$q_{\infty} = \begin{cases} 0, & C_{sr} \leq 0.3 \\ 0.6(C_{sr} - 0.3), & C_{sr} \leq 0.8, C_{sr} > 0.3 \\ 5C_{sr} - 3.7, & \text{otherwise} \end{cases}$$

$$\frac{dq}{dt} = \frac{q_{\infty} - q}{30}$$

$$r_{\infty} = \frac{1}{1 + e^{\frac{-C_{sr}+0.7}{0.01}}}$$

$$\tau_r = \begin{cases} \tau_{r1}, & C_{sr} \leq C_1 \\ \tau_{r2}, & \text{otherwise} \end{cases}$$

(5.2)

$$\frac{dr}{dt} = \frac{r_{\infty} - r}{\tau_r}$$

$$a_n = 0.0001 I_{ca} q$$

$$n_{\infty} = r \frac{a_n}{a_n + b_n}$$

$$\tau_n = \frac{1}{a_n + b_n}$$

$$\frac{dn}{dt} = \frac{n_{\infty} - n}{\tau_n}$$

$$\frac{dc_{cyto}}{dt} = I_{rel} - I_{up} + c1 * I_{ca} + c2 * I_{naca}$$

$$\frac{dc_{sr}}{dt} = -I_{rel} + I_{up} \quad 84$$

$$\begin{aligned}
I_{rel} &= g_{rel}nC_{sr} \\
I_{up} &= \frac{0.003C_{cyto}^2}{C_{cyto}^2 + 0.001} \\
E_{naca} &= \log\left(\frac{Na_o^3C_{cyto}}{Na_i^3C_{ao}}\right) \\
I_{naca} &= C_{naca}(0.83636 - 0.02182V)C_{cyto}(e^{(V-E_{naca})k} - 1)
\end{aligned} \tag{5.3}$$

$$I_{ca} = g_{ca}d_{\infty}f(-0.4V + 13)$$

5.5 Variables

5.5.1 C_{cyto} [uM/L]

C_{cyto} is the free concentration of calcium in the cytoplasm. In Shiferaw 2003, the free concentration of calcium in the cytoplasm is of order 1 microMolar/L, which is our units in the model. Four currents affect the changes in the cytoplasm: I_{rel} , I_{up} , I_{naca} , and I_{ca} [65].

5.5.2 C_{sr} [uM/L][v_{sr}/v_{cyto}]

C_{sr} is the concentration of free calcium in the SR. Its concentration is affected by the I_{rel} current and the I_{up} current. Since the release and uptake are scaled in terms of the cytosol, a scaling factor of v_{sr}/v_{cyto} is needed. The order of the C_{sr} is scaled to 1 [uM/L].

5.5.3 r [dimensionless]

Qu et. al. unified theory calcium alternans denotes the recovery time as an exponentially increasing function dependent on the period, T [70]. The r variable indicates the fraction of the CRUs in the cell that have recovered and available to fire. This variable is time dependent with a steady-state relationship r_{∞} function of C_{sr} . As C_{sr} recovers, the r gate will recover due to its opening probability increasing[74][75]. The steady state dependence of

r is directly proportional to C_{sr} , and the time constant of r directly determines how quickly the CRUs recover to resting state. we simplify this calcium alternans mechanism to a Hodgkin-Huxley variable to capture the minimum properties of time constant of recovery, and a dependence on load.

$$r_{\infty} = F[C_{sr}] \quad (5.4)$$

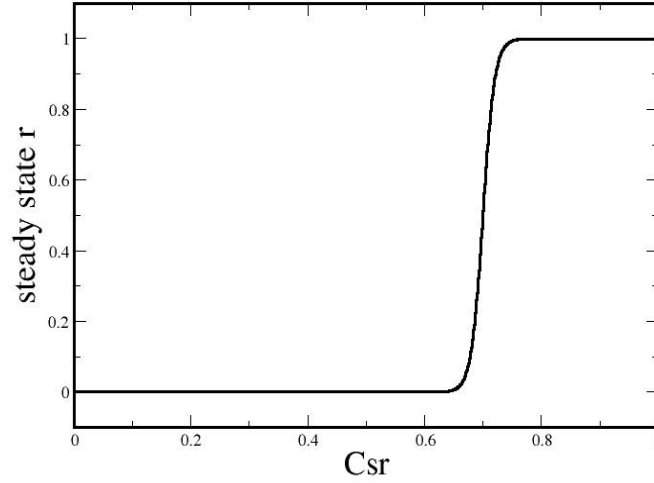


Figure 5.9: Plot demonstrating the steady state of the r gate variable, R_{∞} , versus C_{sr} for our model. At high SR content, the r gate has a higher probability of recovering to its resting values, indicating that a large portion of the CRUs are available to fire.

5.5.4 q [dimensionless]

This variable denotes the release versus load relationship variable. Q is the fraction of the available CRUs that are releasing at a time t . The release-load signifies that the larger the load, the larger fraction of CRUs will release. This variable is time-dependent with a steady-state relationship that is a function of C_{sr} . As C_{sr} recovers, the q gate will recover

as well to full value. Below in figure 5.10, we plot the relationship between the q steady state and the C_{sr} . For further simplification, we depict this nonlinear relationship in simple, linear functions.

$$q_{\infty} = G[C_{sr}] \quad (5.5)$$

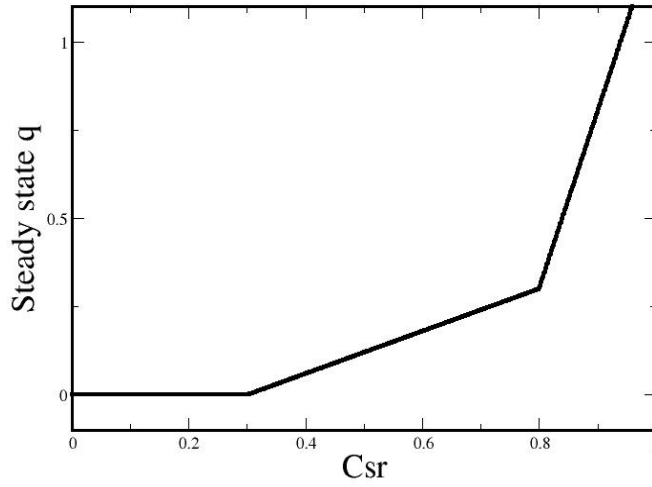


Figure 5.10: Plot visualizing the steady state of the q gate variable of our model and its dependence on the SR calcium concentration. The relationship is determined by 3 piecewise linear functions. This relationship is a major source of the nonlinear relationship between calcium release into the cytoplasm and SR load.

The q variable is very similar to Shiferaw's $Q(Cj_{sr})$, which also indicates the fraction of release depending on load. However, our variable has a time constant because the relationship between q and C_{sr} is not instantaneous, unlike Shiferaw model. In his model, the fractional release relationship $Q(Cj_{sr})$ is dependent on the JSR, not the NSR. Our C_{sr} variable is the equivalent of the NSR concentration in Shiferaw's model, so we have a time constant to indicate the delay between the NSR and JSR compartments.

5.5.5 n [dimensionless]

n is the number of sparks in the cell at time t . For a minimal model, we make its formulation analogous to standard Hodgkin-Huxley gating variables since the CRUs have an intrinsic recovery time constant.

Here, we derive the n variable in the same manner as an HH variable, starting with rate kinetics. We define α_n and β_n , which are the opening and closing rate constants, and they have units of $[1/[ms]]$. For an interval of time Δt , the n variable rate kinetics are

$$n(t + \Delta t) = n(t) + \alpha_n(N - n)\Delta t - n\beta_n\Delta t \quad (5.6)$$

Where N is the number of available CRUs, which is on the order of thousands within a cardiac myocyte,

$$N = N_o r \quad (5.7)$$

Where N_o is the total junctions in the cell, and r indicates the proportion that is recovered by time t .

α_n is the proportional of the available CRU's sparking in an interval, and β_n is the proportion of sparks stopping their release in an interval Δt .

The equation 5.6 can be rewritten in the Hodgkin Huxley style with a steady state equation.

$$n_\infty = N_o r \frac{a_n}{a_n + b_n}$$

,

For our model, we scale N and n by N_o to unity and absorb its value into the release constant g_{rel}

$$n_{\infty} = r \frac{a_n}{a_n + b_n}$$

,

5.5.6 f gate [dimensionless]

Inactivation gate for the L-type calcium current. This variable's steady state is voltage dependent, and is therefore sensitive to APD alternans.

5.6 Derivations of equations

5.6.1 Currents

The units of current are uM/ms. Since the volume of the cytosol and the SR are significantly different, the concentration is divided by the volume of cytosol, so all currents in each compartment are of same value.

5.6.2 Release current

$$I_{rel} = g_{rel} n C_{sr} \quad (5.8)$$

The release current is directly dependent on the the number of sparks, n. n variable is the number of sparks at time t, n(t), and proportional to the recovery variable r and the fraction of release q, and the L-type calcium to denote graded release. The amplitude of a spark is proportional to the gradient between the SR and the cytoplasm calcium concentrations. However, since the C_{cyto} is so much smaller physiologically, the term is neglected and C_{sr} is left.

5.6.3 Uptake current

$$I_{up} = \frac{0.003 C_{cyto}^2}{(C_{cyto}^2 + 0.001)} \quad (5.9)$$

The uptake current is the standard LR94 form used in Luo-Rudy and Shiferaw 2003[53][80][65].

5.6.4 Sodium Calcium Exchanger

For the I_{naca} , we simplify the equation significantly through making a few assumptions and rearranging the format of the equations. The Standard sodium calcium exchanger current in LR94 and Shiferaw 2003 is [80]

$$I_{naca} = g_{naca} \frac{1}{kmNa^3 + Na_o^3} \frac{1}{KmCa + C_{ao}} \Rightarrow \frac{e^{sVk} Nai^3 C_{ao} - e^{(s-1)Vk} Na_o^3 C_{ai}}{1 + k_{sat} e^{(s-1)Vk}} \quad (5.10)$$

$g_{naca}, kmNa, KmCa, k_{sat}, s$ are the sodium calcium exchanger constant, half-maximal response concentration constant for sodium and calcium, saturation constant, and energy barrier constants respectively. For Shiferaw's model, $s = 0.35$, $k_{sat} = 0.25$, and $k = 1/26mV$. Na_o, C_{ao}, C_{ai} , and Na_i are the external sodium, external calcium, internal calcium, and internal sodium concentrations respectively. While Na_i, C_{ao} , and Na_o can vary, we noted that their variance has less of an effect on the qualitative shape of the the sodium-calcium exchanger than the internal calcium concentration changes[17]. For our model to minimize the amount of necessary variables, we assume the Na_i, C_{ao} , and Na_o concentrations to be constants. The remaining C_{ai} is the dynamical calcium variable that the current depends on. In our model, we define C_{ai} as C_{cyto}

The section

$$\frac{e^{sVk} Nai^3 C_{ao} - e^{(s-1)Vk} Na_o^3 C_{cyto}}{1 + k_{sat} e^{(s-1)Vk}} \quad (5.11)$$

is the dynamical portion of the current.

we define the nernst potential of sodium calcium exchanger as

$$E_{naca} = \log \frac{Na_o^3 C_{cyto}}{Na_i^3 C_{ao}} \frac{1}{k} \quad (5.12)$$

The dynamical portion of the current as now be written as

$$\frac{e^{(s-1)vk}}{1 + k_{sat}e^{(s-1)vk}} Na_o^3 C_{cyto} (e^{(V-E_{naca})k} - 1) \quad (5.13)$$

Next, we show that the fraction

$$\frac{e^{(s-1)vk}}{1 + k_{sat}e^{(s-1)vk}} \quad (5.14)$$

can be simplified to a linear dependence. $s - 1 = -0.65$, and $-0.65/26mV = -0.025$

Plotting the following equation over the range [-90,20]mV

$$\frac{e^{-v/40}}{1 + 0.25e^{-v/40}} \quad (5.15)$$

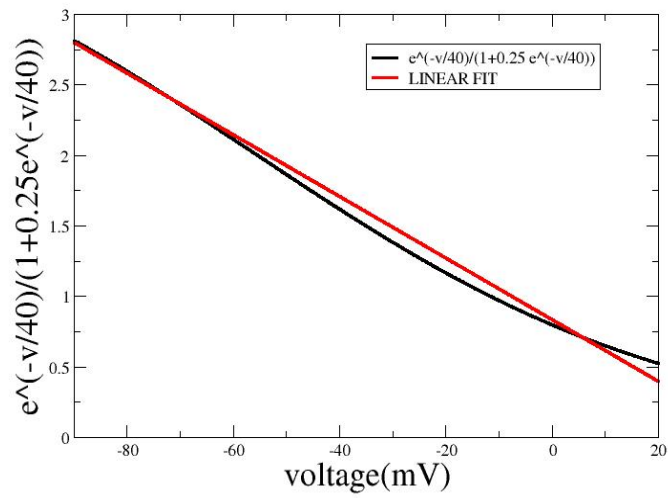


Figure 5.11: Equation 49 in plotted form. The value of equation versus voltage can be fitted with a line.

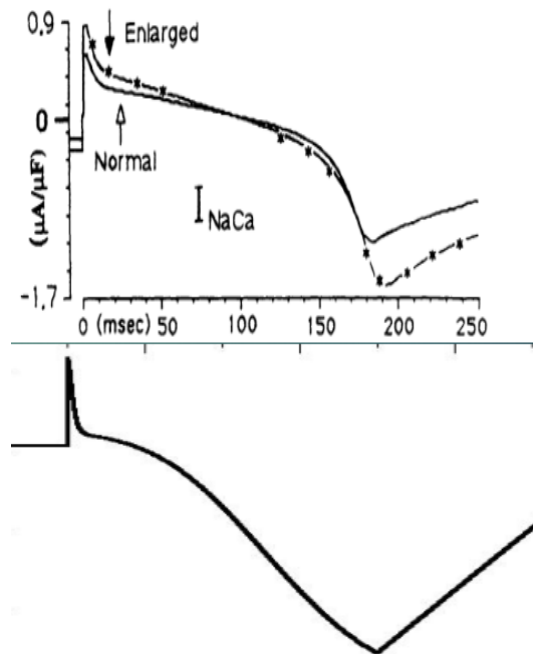


Figure 5.12: Comparison of sodium calcium exchanger current. Top: LR sodium calcium exchanger current and bottom: our model's sodium calcium exchanger current [80].

The current can now be redefined as

$$I_{naca} = g_{naca}(a - bV)C_{cyto}(e^{(V-E_{naca})k} - 1) \quad (5.16)$$

In figure 5.12 above we exhibit our simplified I_{naca} equation and compare it to the standard LR I_{naca} , and we observe that the form is qualitatively similar. We can see from this simplified form the direct effect of calcium alternans on the sodium exchanger. Moreover, the equation are more intuitive and easier to manipulate.

The linear fit of the voltage dependence shows deviation at high voltage values of the action potential. However, the sodium-calcium exchanger's main effect manifests at values less than 0mV.

5.6.5 L-Type Calcium current

Like the I_{naca} , we make similar reductions to the I_{ca} current and rearrange the form to create a minimal simplified equation. The Shiferaw L-type calcium current is[65]:

$$I_{ca} = g_{ca}d_{\infty}fqi_{ca} \quad (5.17)$$

With the single channel i_{ca} current as:

$$i_{ca} = \frac{V}{e^{2vk} - 1}(c_{sub}e^{2vk} - 0.341Cao) \quad (5.18)$$

The c_{sub} is 1000 times smaller than Cao . The order the term multiplying C_{sub} is less than 1 for most values of voltage and at largest around 8 when the voltage is at its peak.

Thus, the term

$$c_{sub}e^{2vk} \quad (5.19)$$

will be omitted from the model. The remaining small channel current is proportional to

$$i_{ca} = g_{ica} \frac{V}{e^{2vk} - 1} \quad (5.20)$$

It is possible to reduce this fraction further by linearly fitting the relationship. During relatively normal AP conditions, the L-type calcium current is non-zero for a certain interval of voltage. The linear fit needs to be accurate for this interval only.

Thus, the full current can be reduced to

$$I_{ca} = g_{ca}d_{\infty}f(aV + b) \quad (5.21)$$

In the figure 5.13, we compare the typical I_{ca} equation to our simplified form.

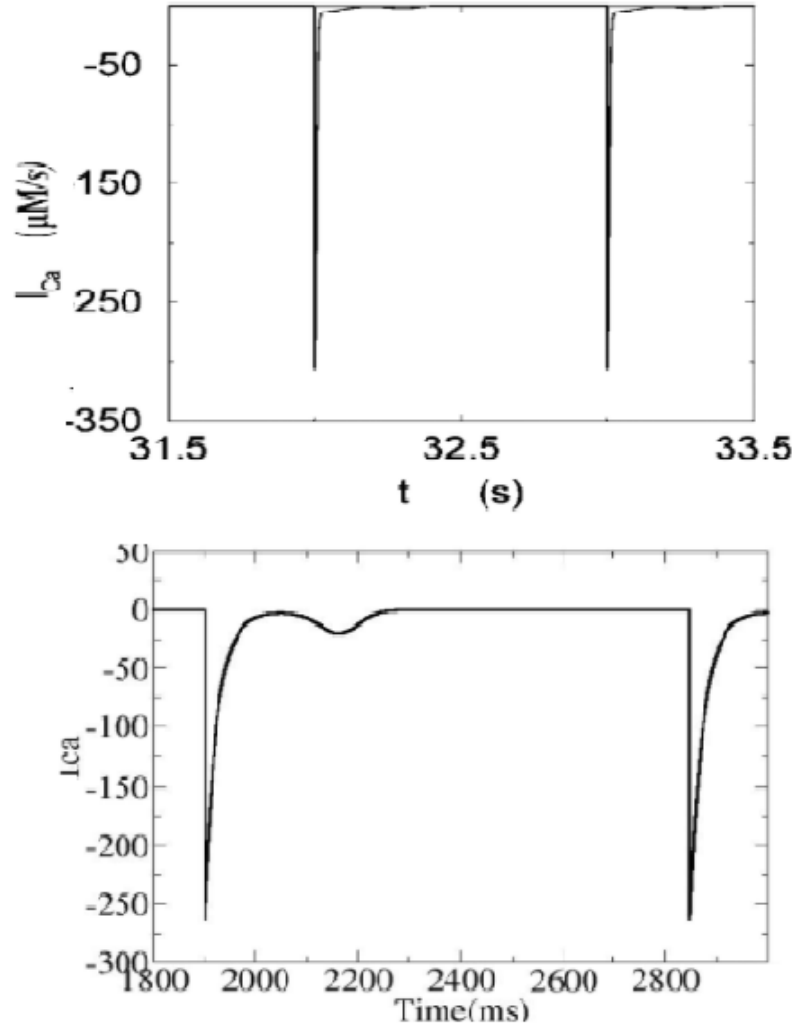


Figure 5.13: Time series plot showing comparison of L-type calcium currents of the Shiferaw 2003 model and our minimal calcium model.[65] Top: Image of Shiferaw L-type calcium current. Bottom: Image of our simplified L-type calcium current. Both models' L-type calcium current has shark peaks and a small late current.

5.7 Results

To test the validity of our model, we aim to reproduce experimental results. A main focus of our model is the variables that contain mechanisms for alternans. To investigate each aspect of the alternans variables, we isolated each mechanism to test its ability to produce calcium alternans independent of electrical instability. At this stage, the model is voltage

clamped with an action potential-like waveform, plotted in figure 5.14, and the total calcium is unchanging. We simulate our minimal model in a single cell with $dt = 0.001\text{ms}$. See Appendix for modeling parameters.

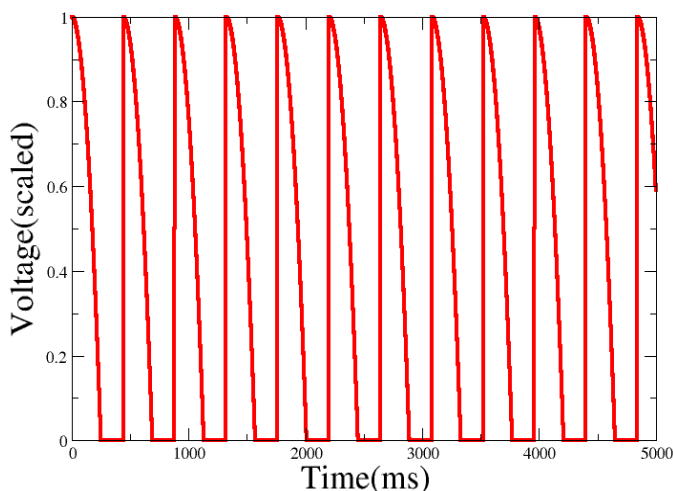


Figure 5.14: Image visualizes the clamped voltage waveform used in both scenarios of calcium alternans and no calcium alternans. Clamped waveform demonstrates that voltage does not contain the source of alternans and is not necessary for calcium transient to alternate independently.

5.7.1 Alternans from Q

The release load mechanism is captured in the variable q and is a distinct mechanism from the refractoriness of the CRU's, captured in r . For the release load mechanism, the load (C_{sr}) alternates every beat, resulting in alternating release. We assume that the total calcium in the cell is relatively constant beat to beat, or varies slowly, and the resting calcium concentration will vary as well. To isolate this mechanism so that the r gate is not the culprit in alternans, we change the time constant of r gate such that it recovers very quickly to the same value despite changes in pacing period, shown in figure 5.15, and we adjust its steady state function so that it begins recovering relatively early. In addition, we clamp the voltage to a steady action potential waveform.

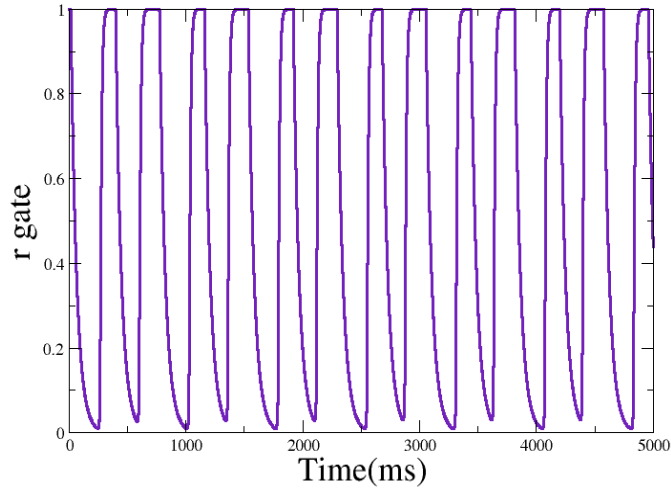


Figure 5.15: Time series plot illustrating the r gate of the system in the previous two scenarios of both alternans and no alternans in cytoplasmic calcium concentration. The r gate recovers fully to the value of 1 before each beat, indicating that it is not the source of alternans.

Next, we tested two cases of q gate. Since the release load mechanism depends on the nonlinear relationship between release fraction and load, captured in the steady state value of q , we change steady state function of q from nonlinear to linear and observe its effects on the appearance of alternans.

In case 1, the steady state q is nonlinear, shown in figure 5.17, and alternans appear in calcium, shown in time series in figure 5.16.

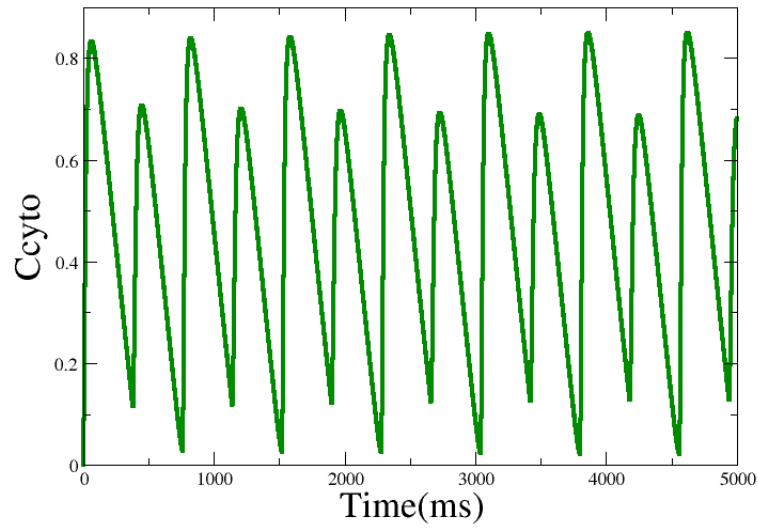


Figure 5.16: Figure depicts the cytoplasmic calcium concentrations plotted in time series showing distinct alternans due to q gate steady state's nonlinear dependence on SR calcium concentration. For this scenario, both the peak and the end-diastolic calcium values alternate.

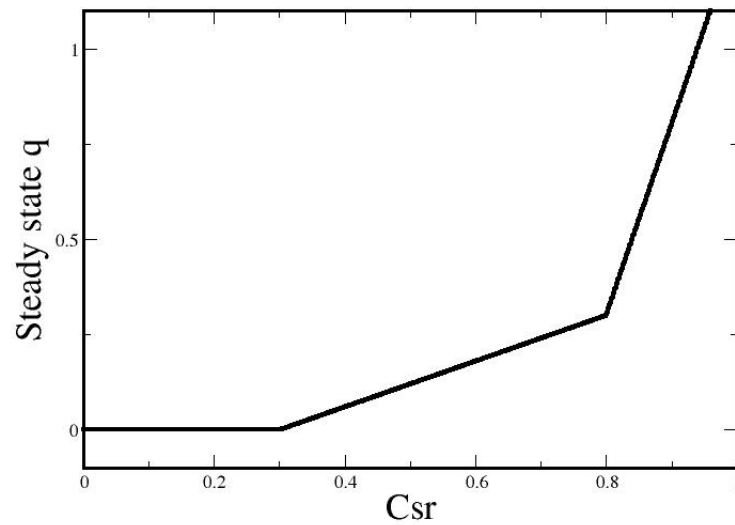


Figure 5.17: Image depicts the Q gate steady state relationship with SR calcium concentration. 3 piecewise functions contribute to the shape of the relationship. If the relationship is nonlinear, as shown in the image, the resulting calcium transient is capable of producing alternans.

In case 2, the steady state of the q gate variable is adjusted such that it is a linear function of the SR calcium concentration, shown in 5.18. Now, when the model is simulated and paced in a steady period in single cell, the calcium transient alternans disappear, plotted in time series in 5.19.

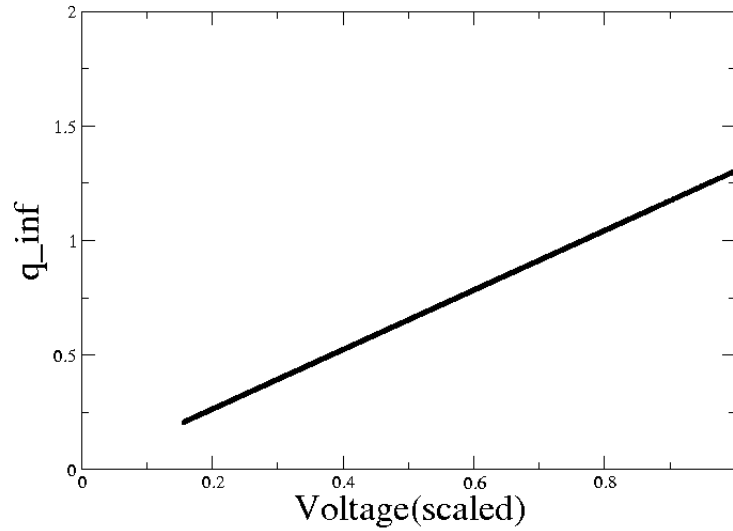


Figure 5.18: Image depicts the Q gate steady state relationship with SR calcium concentration. A linear function determines the shape of the relationship. If the relationship is linear, as shown in the image, the resulting calcium transient is incapable of producing alternans.

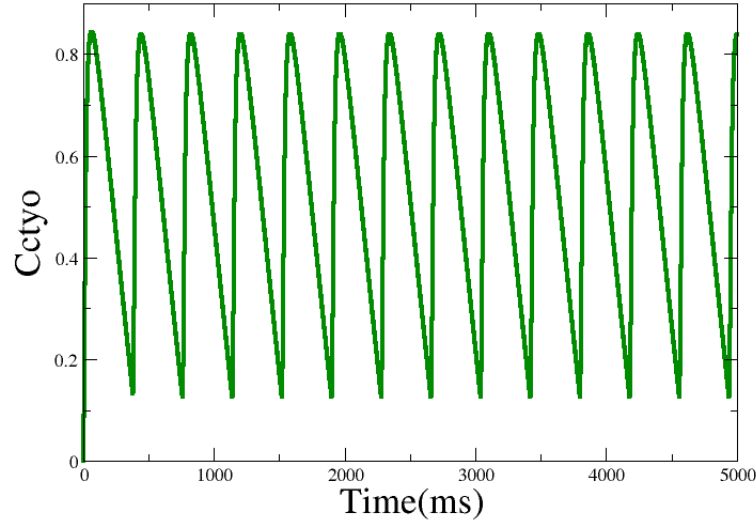


Figure 5.19: Cytoplasmic calcium concentration plotted in time series. The calcium transient is not alternating, due to the manipulations in the q gate equations.

5.7.2 Alternans from R

The r gate captures the intrinsic refractoriness of a CRU. To isolate this mechanism, we first construct the q gate so that it is incapable having alternans in manner of the previous section, by making the steady state of q a linear function of calcium. In addition, we increase the pacing period of the voltage significantly such that the system no longer alternates.

Next, we adjust the steady state values of r such that it begins recovering after the load has almost recovered to full value. Below, we compare two cases of r gate phenomena. In case 1, the time constant of the r gate is relatively large at 200ms. In the figure 5.21, we plot the clamped waveform, C_{cyto} , and r gate.

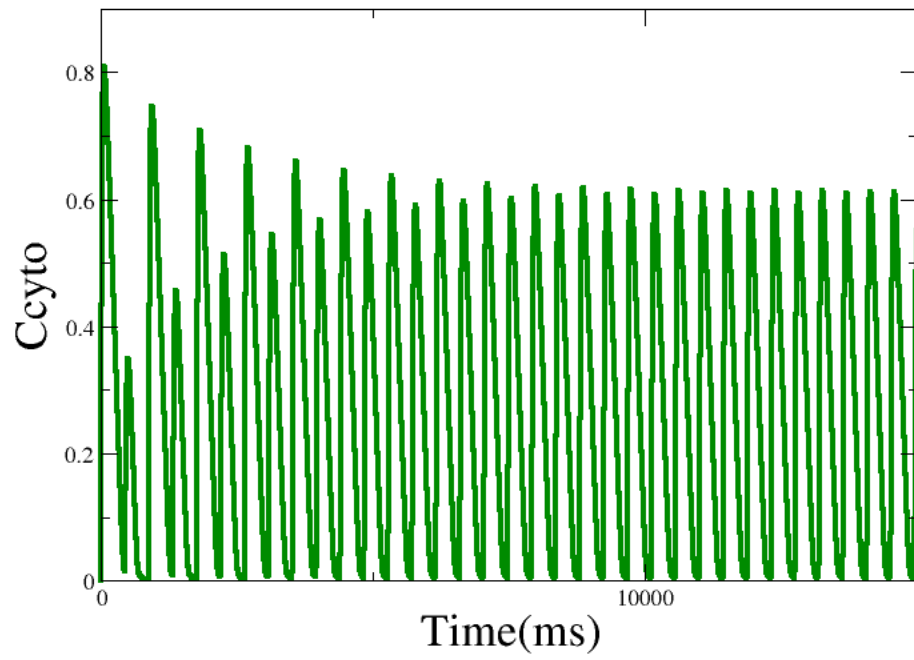


Figure 5.20: Cytoplasmic calcium concentration in time series, showing no alternans due to r gate dynamics.

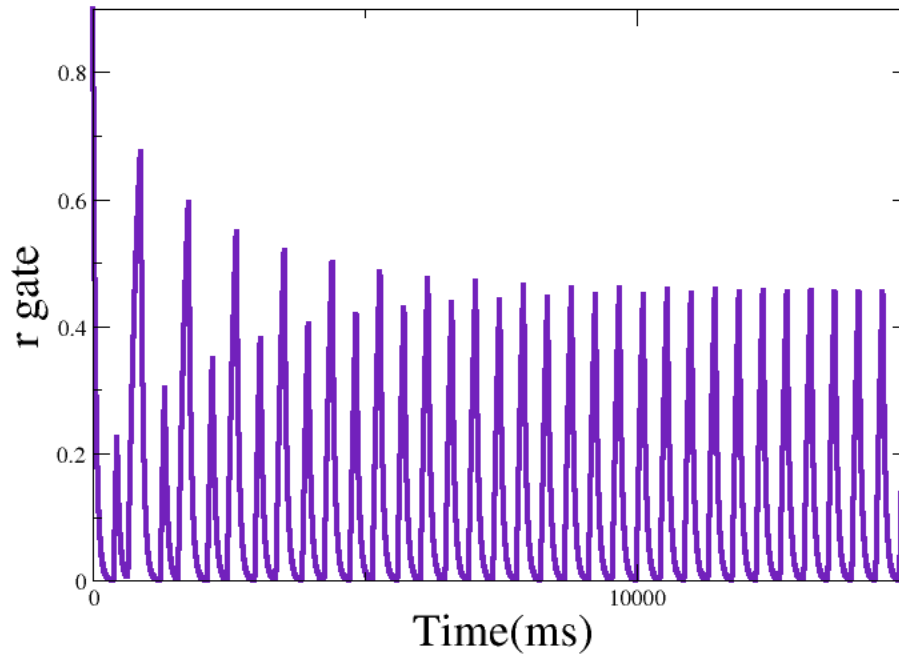


Figure 5.21: R gate variable in the corresponding time series to figure 5.22 showing no alternans.

Next, we maintain the same values of parameters but increase the r gate's time constant to 50ms.

Even with load recovering to almost full value before each beat, q steady state being linear, and voltage being clamped, the r gate, shown in figure 5.21, alternates every beat, resulting in calcium alternans. In this case, the calcium resting state concentration does not vary greatly and neither does the load. Thus, this mechanism is distinct from the release-load mechanism.

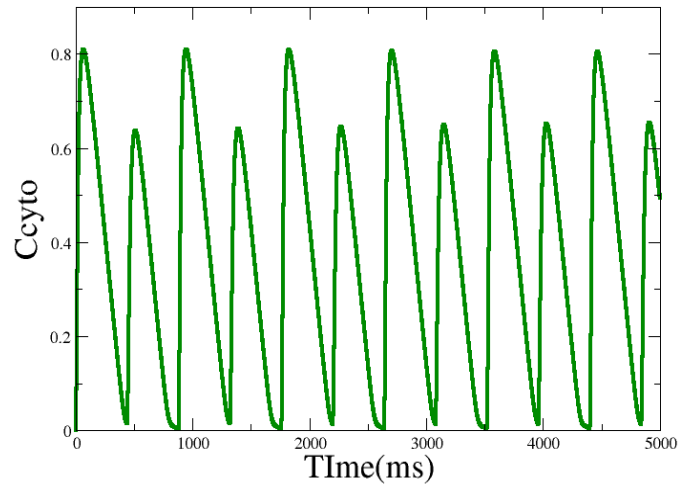


Figure 5.22: Cytoplasmic calcium concentration in time series showing alternans due to r gate dynamics. For this scenario, the peak of the cytoplasmic calcium concentration is alternating significantly, but the end-diastolic value is alternating relatively less.

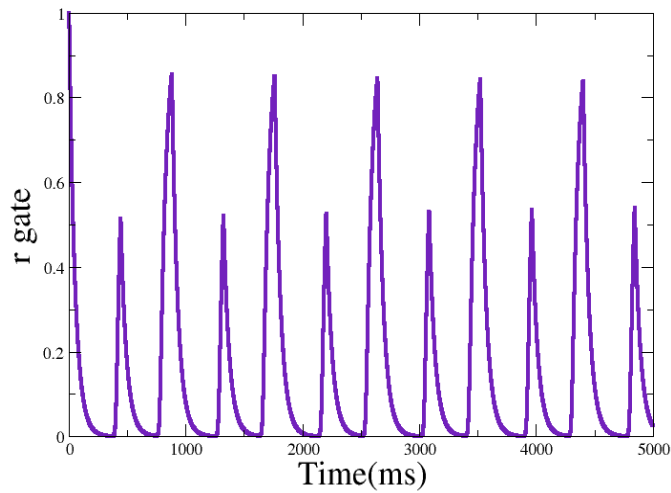


Figure 5.23: R gate variable in time series showing distinct alternans, indicating that it is the cause of alternans. Figure corresponds to cytoplasmic calcium concentration plot in figure 5.22

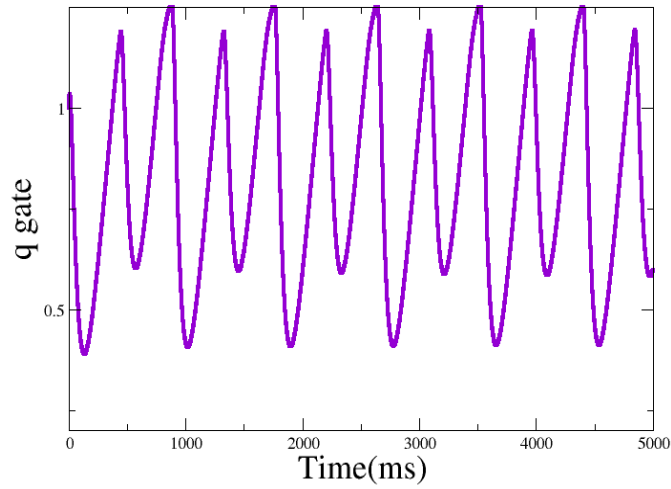


Figure 5.24: Q gate variable in the corresponding time series to figure 5.22, showing relatively less variation in value before each beat than the r gate variable time series in figure 5.23

To note, there are structurally two types of calcium alternans captured in figure 5.25. The value of the cytoplasm calcium concentration before the next beat is the end-diastolic calcium concentration. This value can experimentally vary beat to beat.

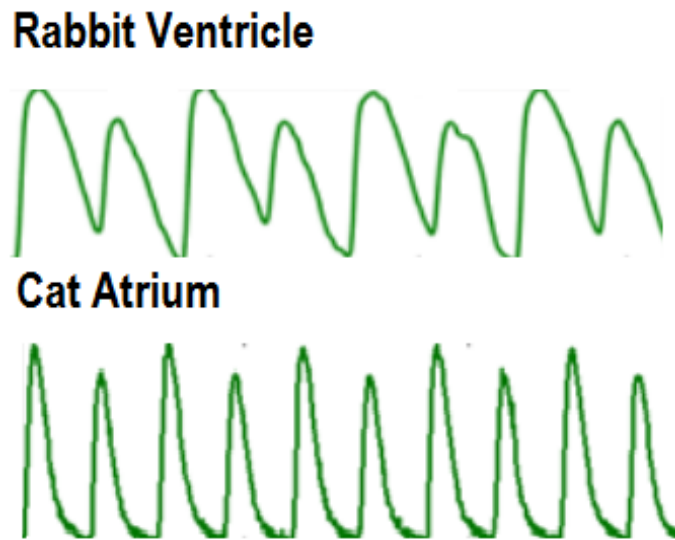


Figure 5.25: Image above depicts two different types of cytoplasmic calcium alternans in time series in two different animals, rabbit ventricle and cat atrium tissue. The resting calcium value after each beat varies in rabbit ventricle, but not in cat atrium, giving evidence of different sources for calcium alternans.

We note that when the end-diastolic calcium concentration varies, the release-load mechanism is a likely culprit of alternans due to the SR load variation. If the end-diastolic calcium is not varying greatly, the load is not varying as well, then we observe that the CRU refractoriness is a likely culprit of alternans. A limitation to our hypothesis may occur if the total calcium entering and leaving the cell changes significantly, especially during arrhythmia.

5.7.3 Driven Alternans from Bidirectional Coupling

Since calcium and voltage are coupled physiologically, we construct the action potential waveform so that it produces action potential alternans so observe its effects on calcium dynamics. The calcium system is made unable to have alternans in this instance. R gate time constant is 200ms and the q gate steady state is a linear function of load.

In the figure 5.26, we give the action potential a period of 500ms, and its alternans drive

the calcium system to alternans despite the calcium alternans mechanisms inactive.

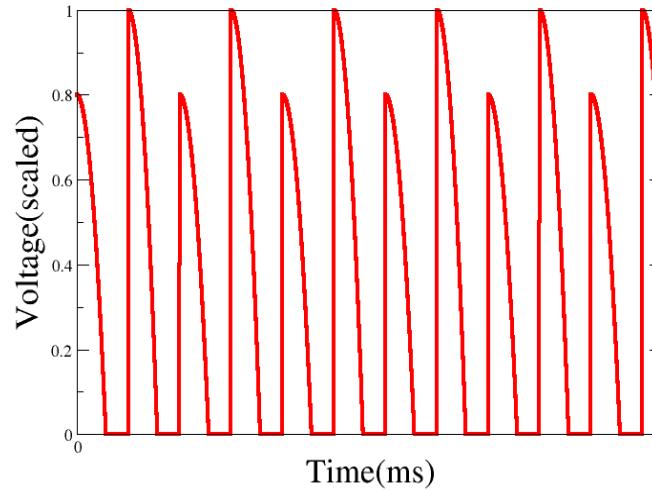


Figure 5.26: Figure plots the clamped action potential waveform in time series that is coupled to our minimal calcium model. The action potential is tuned to have alternans every other beat and in turn produces alternans in calcium transient.

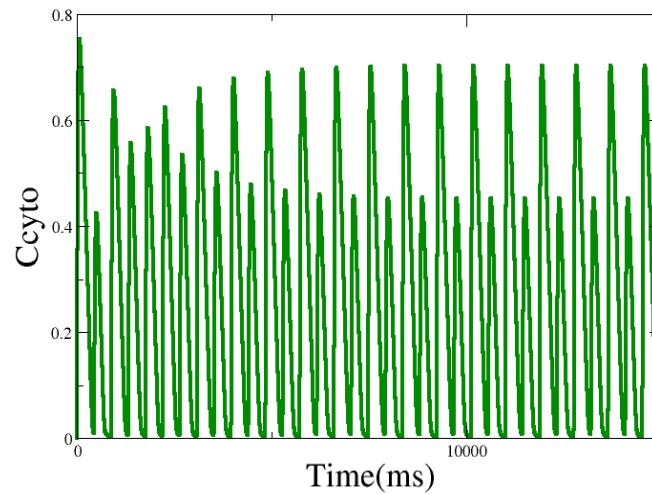


Figure 5.27: Plot demonstrating the resulting cytoplasmic calcium concentration corresponding to 5.26. Y axis is cytoplasmic calcium concentration and x axis is time. The calcium system is tuned to be incapable of alternans independently, but the voltage system drives the calcium system to alternans nonetheless.

Next, with the same parameters for the calcium model, we clamp the action potential waveform to a periodic state for the same period. The calcium alternans disappear.

5.7.4 Application to Experimental Data

We test our bidirectionally coupled calcium by applying it to laboratory experimental data. First, we unclamp the voltage and add I_{naca} and I_{ca} to the cytoplasm calcium concentration, which varies the total calcium slightly. Unlike the previous sections, we now replace the action potential waveform with a minimal two variable model. Details of models parameters contained in appendix sections. From our laboratory experiments, we obtain simultaneous voltage and calcium alternans for the rabbit ventricles and cat atria.

The cat atrium data time series, given in figure 5.28, is shown with voltage series in the top panel and calcium in the bottom. The voltage signal does not appear to alternate, but the calcium signal is. An observation to note is that the diastolic calcium concentration before each release is relatively similar. Moreover, the peak calcium release is relatively steady, so we deduce that in this case, the SR load is not alternating before each beat.

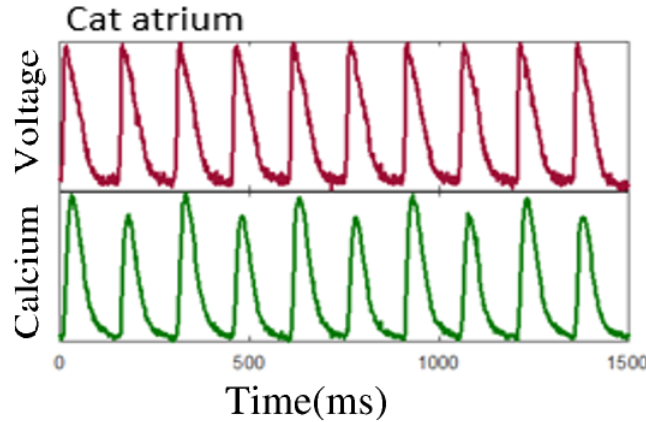


Figure 5.28: Laboratory experimental voltage and cytoplasmic calcium cat atrium time series. Voltage is in red in top panel and calcium is in green bottom panel. The voltage system is not visibly showing alternans, but the calcium transient is demonstrating alternans in peak amplitude.

To fit such data, we tune our model such that the release-load variable q is not alternating and the refractoriness variable r gate is. To fit the r gate, we change the time constant

such that it recovers with 50ms, and furthermore adjust the steady state so the r gate begins its recovery after the load(C_{sr}) has recovered to almost its full value. This ensures that the load does not vary beat to beat. The result, shown in figure 5.29, is qualitatively similar to the experimental data in voltage and calcium form. Its diastolic calcium is steady, but the peak release varies beat to beat. To prevent the calcium system from bidirectionally influencing the voltage system to alternans, we decrease the strength of the sodium calcium exchanger current, as it affects the APD.

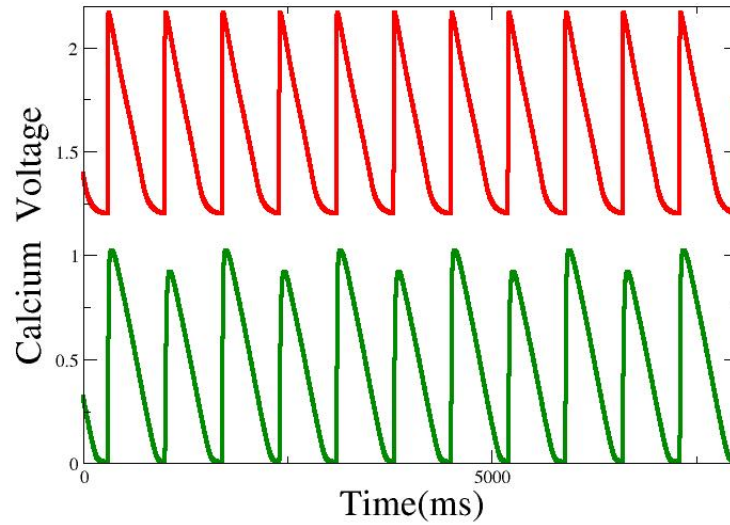


Figure 5.29: Our model tuned to mimic experimental cat atrium data in figure 5.28. Top panel is voltage in red and bottom panel is cytoplasmic calcium concentration in green. Note, like the cat atrium data, the voltage system is not alternating visibly but the calcium transient is alternating in peak amplitude. The end-diastolic calcium level is not changing significantly.

For the rabbit ventricular time series, shown in figure 5.30 , we tune our model to capture both voltage and calcium alternans.

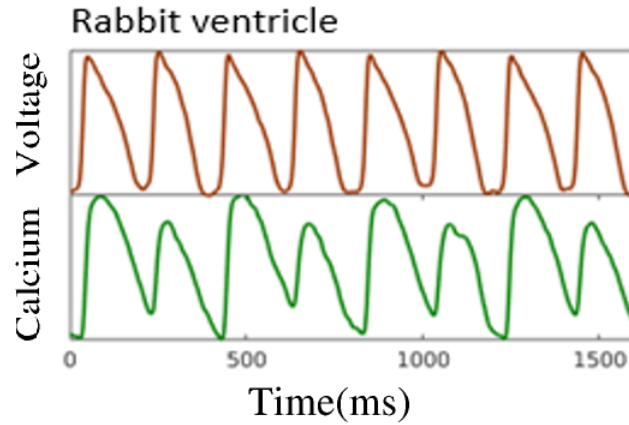


Figure 5.30: Figures gives experimental laboratory data of rabbit ventricles showing simultaneous voltage and cytoplasmic calcium signals in time series. Red line is the voltage time series and Green line is the calcium time series. Calcium shows distinct alternans in both peak and end-diastolic values, while voltage shows relatively less alternans.

For the rabbit ventricular voltage calcium data, we note that the resting calcium varies greatly with each beat. Moreover, while the action potential is alternating in APD, its alternans gradient is relatively small compared to the calcium system. Thus we hypothesize that the SR load release mechanism is affecting the calcium alternans and is the source of the voltage alternans.

Since both systems are alternating, we first adjust the parameters in our calcium model to reproduce SR calcium alternans to match the shape of the signal, shown in figure 5.31. Action potential is clamped to a periodic waveform.

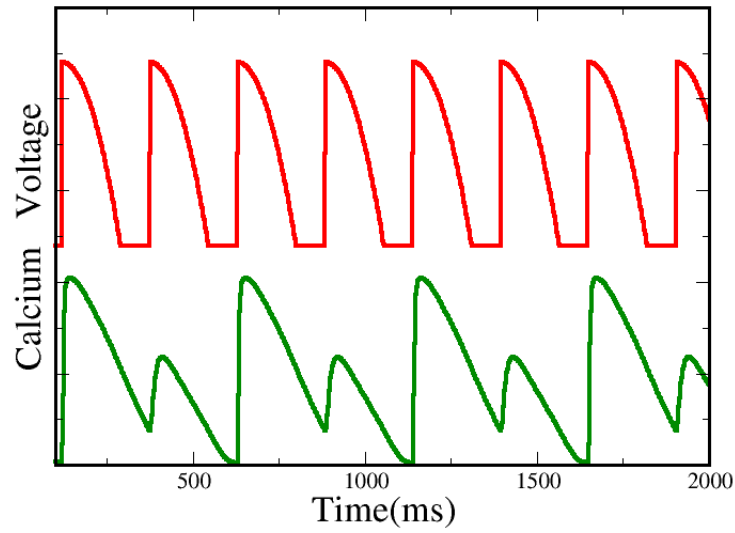


Figure 5.31: We plot the single cell paced system's voltage(red) and cytoplasmic calcium concentration(green) in time series. Voltage is clamped to a periodic action potential waveform, and cytoplasmic calcium persists in alternans mode due to q gate parameters.

Next we bidirectionally couple this model to a simple voltage system that mimics the shape of the experimental voltage data, and result is alternans in voltage time series, shown in figure 5.32. In this case, we increase the effect the transmembrane currents on the voltage.

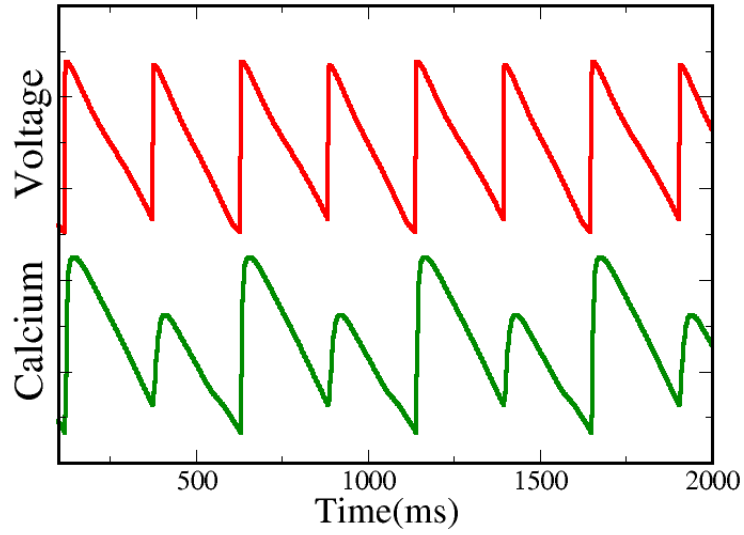


Figure 5.32: Image gives plot in time series showing our model in single cell with the q gate manipulated such that the calcium cycling system produces alternans. Red line is voltage system in time series and green line is cytoplasmic calcium concentration in time series. Because we adjusted the steady state of the q gate such that dependence on the cytoplasmic calcium concentration is nonlinear, the resulting cytoplasmic calcium concentration and voltage system are both alternating.

When we tune the calcium system such that the q gate is no longer capable of alternans, shown in figure 5.33, the voltage alternans disappear.

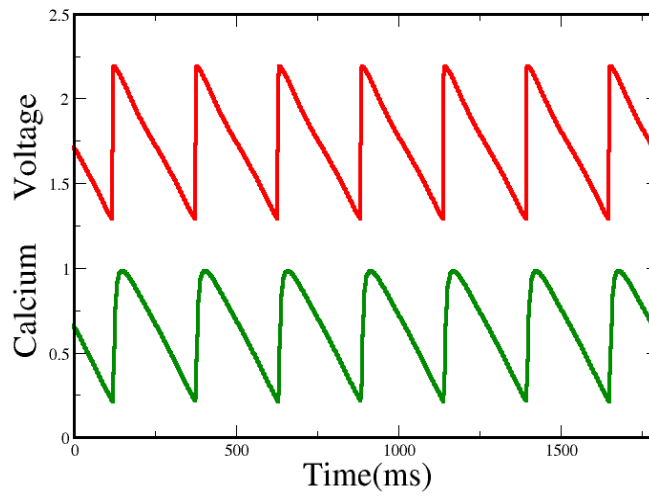


Figure 5.33: Image gives plot in time series showing our model in single cell with the q gate rendering system incapable of alternans. Red line is voltage system in time series and green line is cytoplasmic calcium concentration in time series. Because we adjusted the steady state of the q gate such that dependence on the cytoplasmic calcium concentration is linear, the resulting cytoplasmic calcium concentration and voltage system are not alternating.

To confirm that calcium is the source of alternans, we clamp the calcium and note that alternans in voltage disappear, in figure 5.34.

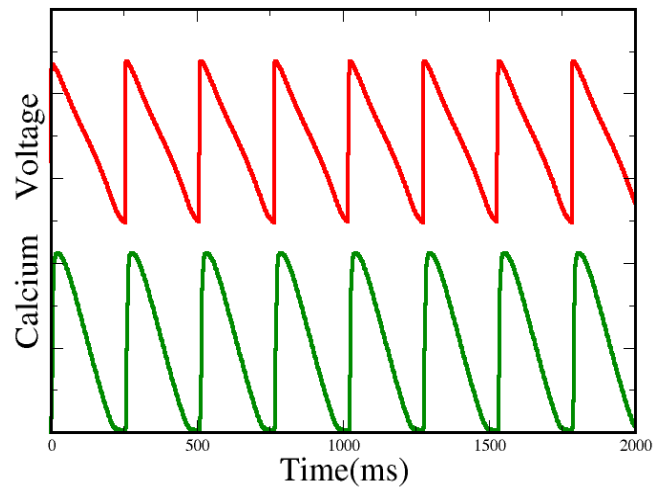


Figure 5.34: Image illustrates a time series plot, in single cell, of voltage signal in red and calcium transient in green. The cytoplasmic calcium system is clamped to a steady form and coupled to the voltage system. The result shows no alternans in the electrical system.

Finally, in the figure 5.35 we compare the voltage system with calcium alternans and no calcium alternans, and conclude that the voltage alternates due to calcium.

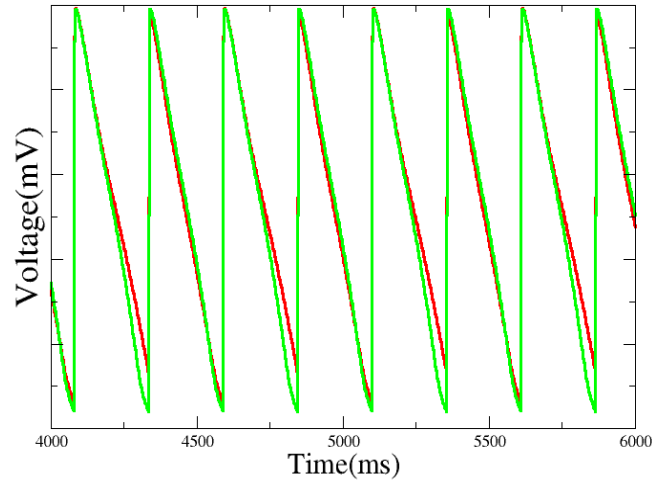


Figure 5.35: Image visualizes a plot of voltage time series before and after clamping the calcium cycling system. The green signal is the voltage system when the cytoplasmic calcium is clamped and is not alternating, and the red signal is the voltage system when cytoplasmic calcium is clamped. This comparison gives evidence to the fact that the calcium system is the source of instability.

From this type of fitting and testing, we can hypothesize the origin of alternans through fitting and clamping.

5.8 Limitations

Several important limitations are apparent for our model. Firstly, minimal modeling carries the disadvantage of most phenomenological models in that it reproduces behavior but not necessarily the specific ionic mechanism from realistic experiments. Our model, while capable of alternans, is a dynamical reduction to the most salient properties for alternans. Normally in physiology, the two alternans mechanisms are coupled. but here, we decouple them.

5.8.1 Spark Lifetime

In Shiferaw's 2003 model, the author characterizes sparks as transient release that have a lifetime[65]. In our model, the sparks are phenomenologically represented but they do not have a lifetime. However, we believe that this lack of lifetime does not have a large effect on the release because the release current is relatively short in duration.

5.8.2 Buffers

A limitation to our phenomenological model is the lack of calcium buffering equations in our model. Calcium is highly buffered in the myocyte due to its potential toxicity. For example, in the SR, calsequestrin bind free calcium and affects the rate of release and for uptake, the SERCA protein binds calcium to the SR. Our model does not capture the intricacies of calcium buffering and is thus a dynamical model meant to understand the causes of alternans. However, Shiferaw's 2003 paper reduces its dynamic buffering to instantaneous buffering, and our model is capable of doing this as well. Furthermore, our model is simple and flexible enough to add further complexities such as buffering dynamics.

5.8.3 Total calcium variation

The total calcium in a cell can vary beat to beat. However, this limitation is physiologically grounded because typically the net change in total calcium in a cell is small compared to total release of calcium, unless the cell is in an arrhythmogenic state[65]. Our model thus far does not include this feature, and it may affect the release load mechanism. However, it is possible to add an equation that scales the total calcium in the cell to fit to realistic parameters.

5.8.4 Contraction

Our model is a calcium release model and does not include contraction modeling, which is the fundamental process for the hearts pumping of blood. However, we note that it is

possible to add a contraction model to our phenomenological model.

5.8.5 Reduction in Compartmentalization

A significant reduction of our model is the compartmentalization of the calcium system. In Shiferaw 2003, the submembrane space is a necessary compartment to capture the dramatic local rise in calcium concentration[65]. The cytoplasm calcium concentration is significantly different than the submembrane concentration, which affects the dynamics of the transmembrane calcium currents. Yet, to create a phenomenological model that reproduces calcium signaling that mimics experimental data, we did not need the submembrane space compartment. For future work, it is possible to add this variable to reproduce realistic dynamics. A second reduction in compartmentalization is the absorption of the JSR calcium concentration variable from Shiferaw's model into our SR calcium concentration. Between the two compartments, a delay of transfer of calcium occurs, but we accounted for this delay in the q variable time constant.

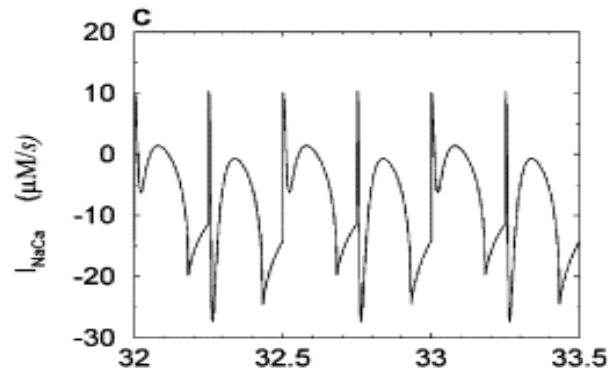


Figure 5.36: Plot illustrates the sodium calcium exchanger current in time series from Shiferaw 2003 model due to the compartmentalization of spaces[65]. Because the concentration rise in the submembrane space is sharp and the sodium-calcium exchanger equation is dependent on its value, the shape of the resulting time series differs from our model.

5.9 Customization of Calcium Modeling

In this project, we constructed a minimal calcium model for alternans inspired by Shiferaw's 2003 calcium model. We focus on two main mechanisms for calcium alternans, the release load relationship, and the refractoriness of CRUs. For each mechanism, we assigned a Hodgkin Huxley style variable to capture the fundamental properties of alternans. As a result, our model is capable of reproducing graded release, independent alternans with both mechanisms separately, and bidirectional influence. Furthermore, our model's equations, especially those of the I_{ca} and I_{naca} currents, are significantly simplified. While there are several limitations to our phenomenological model, the model itself is computationally tractable and intuitive for understanding. In addition, the model is flexible in expansion for more detail and less phenomenology. Currents such as troponin, buffering can be added. More importantly, contraction models can be used to create a complete model for cardiac contraction. Here with our model, we provide a flexible framework for the study of the calcium system by allowing for adjustment and customization.

CHAPTER 6

CONCLUSION

In this thesis, we investigated the mechanisms for arrhythmia through studies of minimal models for both the voltage and calcium systems. I developed several simplified and minimal models, and these models were used to investigate and uncover new mechanism that can destabilize cardiac dynamics. Because these models are minimal, they can now be used by others researchers to guide the construction of more complex models and investigate other arrhythmic mechanisms.

6.1 Action Potential Amplitude Alternans

APD alternans, in the past, was a widely accepted path towards instability. However, both literature search and experimental laboratory data show that the appearance of APD alternans does not necessarily indicate the onset of fibrillation. From experimental data, we observe that the appearance of APA alternans is more conducive to the likelihood of conduction block and therefore fibrillation. In the first project introduced, we used a two-variable model to produce a novel stability return map that predicted the onset of action potential amplitude alternans instead of action potential duration. By examining the model, we extracted three key relationships between APD, DI, h gate, and voltage amplitude. With analogous derivations to the APD return map, we formed the APA return map and derived that stability equation that if met, will result in APA alternans in the model. From our derived APA return map, we successfully predict the occurrence of APA alternans in our 2 variable model. Furthermore, we related the parameters of the simple model to the stability condition for amplitude alternans and gave a more intuitive understanding of the underlying mechanisms. This new mechanism could be now used to further investigate how conduction block initiation and prevention can be enhanced or suppressed in models

and experiments.

6.2 Take-off Potential

For the take-off potential project, we observed a key deficiency in current models because a majority of the models do not reproduce the varying TOP during VF. This deficiency creates qualitatively different solutions in models compared to recorded experimental data, even when models were fitted to experimental restitution curves. From a dynamical perspective, unvarying TOP restricted the complexity of solutions in phases space significantly. We targeted the source of low take-off potential, the sodium current gating variables and their time constant functions. We fitted the equations with simpler forms and adjusted the equations so that the take-off potentials are raised. An important observation from this project is that simpler equations are useful and should be used for future minimal modeling. In fact, simplified equations led to our third project, which demonstrated that not only minimal models reproduce observed phenomena, it can also reproduce novel occurrences as well.

6.3 Excito-Oscillatory Behavior

In the third project, we introduced a novel, two-variable model that produces chaotic behavior without spiral waves or spiral wave breakup. Furthermore, by the tuning of various parameters, this model can produce a spectrum of behavior ranging from distinct spiral waves to circular oscillations. Experimentally, our model's behavior is validated because during VF, the electrical waves are not perfect spiral waves, but rather globular oscillations. For this model, we analyzed the nullclines in the phase space and observed three fixed points. Through literature reviews, we also connected this model to other simple two variables models with the same type of fixed points. In the three models, we observe behavior such as tail-ignition of a wave, chaos without SWB, and high TOP. For all three models, we also detect both excitable and oscillatory behavior. Despite the fact that the models are

from different fields of research, they have striking similarities, which suggests that further studies should be done on models with nullclines of this type. From this project, we conclude again that minimal models are useful in producing a variety of behavior and are easily manipulated. In addition, we note that the combination of excitable and oscillatory behavior produces richer dynamics in space.

6.4 Minimal Calcium Alternans Model

In experiment, calcium alternans and voltage alternans can occur in various combinations and forms. Using the current complex calcium models to fit to such data can be detrimental to the understanding of underlying mechanisms for instability. For the last project, we introduce a minimal calcium model that is bidirectionally coupled to voltage. We focus on two main mechanisms for calcium alternans and constructed a minimal calcium model that is capable of alternans even when the voltage is clamped. In addition, we simplify transmembrane calcium currents to simplified forms and still retained their main characteristics. Next, we couple this calcium model to a minimal voltage model and reproduce experimental results. By fitting the model to the laboratory data, we were able to hypothesize on the origin of alternans in both voltage and calcium systems in different mammals.

6.5 Limitations

In general with minimal modeling, the main limitation with such practice is that the equations are less physiologically based than realistic, and more complex models with significantly more variables. For example, the Bubbly model has 1 potassium current to recover the system to rest, but in reality multiple time dependent potassium currents exists, which dramatically affects the dynamics of the system because the nullclines of the system will no longer give the 3 types of fixed points that lead to the excito-oscillatory behavior. For the APA alternans project, the stability condition predicted the onset of alternans with the simple two variable model, but for models with 10 times as many variables, the condition

may break down because the voltage amplitude is not only dependent on the h gate. For the calcium minimal modeling, the spatial dynamics of calcium cycling, even within one cell, are neglected. While our model produces alternans, the foundation of the variables are due to a mean-field averaging of the system.

6.6 Future Work

For our future work, we will continue with the bubbly model and calculate the stability of the traveling wave solution in a cable system. As of now, we show through calculations that the traveling wave destabilizes into a relative periodic orbit. The next step is to calculate the stability matrix of the RPO. For the calcium system, we will fit the model to more animals in laboratory settings. Furthermore, we will fit the model to restitution curves derived from experiment to validate our model.

Appendices

APPENDIX A

CONTRIBUTIONS IN EXPERIMENT AND SIMULATIONS

Experimental laboratory data used in this thesis are extracted from published peer-reviewed research manuscripts, or are conducted through the author's laboratory experimental researchers. A majority of the data from the author's laboratory were produced by other researchers. However, the author did contribute to extraction of mammalian hearts from test subjects. Simulations in this thesis were done by the author unless specified otherwise. Mathematical derivations and equations were also done by author under the guidance of members of the thesis committee. For the APA alternan and TOP papers, the author was guided by Professor Flavio Fenton and Dr. Richard Gray. For the Bubbly excito-oscillatory model paper, the research was heavily guided by Professor Roman Grigoriev. For the minimal calcium model, the author was guided by Professor Yohannes Shiferaw.

APPENDIX B

NUMERICAL METHODS AND SIMULATIONS

For all projects and models, we simulated the ordinary and partial differential equations with Fortran 77 and Fortran 95. In addition, the method used for simulations was forward Euler method for dt ranging from 0.01 to 0.0001ms. The main exception was the excito-oscillatory "Bubbly" model in chapter 4, where Runge-Kutta 4 was used to integrate forward in time. In addition, for the excito-oscillatory model's cable solutions in 1D, we used a semi-implicit backward Euler method to calculate the solution.

For chapter 4, where simulations were done in square lattice tissue, OpenAcc and WebGL were both utilized to enhance the speed. OpenAcc is a programming language for parallel computing with GPUs and is developed by Cray, Nvidia, and PGI.

A significant benefit of OpenAcc is that it allows for parallelization by slight modifications to the original code. To use OpenAcc, we installed the PGI fortran compiler. In addition, we inserted several lines of code into the sections of the simulation program that are loopable. The structure of the parallelization code is as follows:

1. **\$acc data copyin(variable1, variable2)**

This line of code copies the variables on the CPU to the GPU. Line must be inserted into the code before any other calculations.

2. **\$acc kernels**

[Loopable code]

\$acc end kernels

This section of code runs the loopable code in the GPU. For example, if the code has a do loop, the do loop section will have the first line inserted before its run, and the second line after its run in the original code. The result is that the loop will be parallelized in the GPU

3. **\$acc update host(variable1, variable2)**

This line updates the results from the loop in the GPU and sends the variables values back into the host, or the CPU

4. **\$acc end data**

This last line signifies the end of the GPU computations.

WebGL also utilizes GPU to produce simulations, but is compatible with any web browser, allowing the user real-time simulations alongside simultaneous changes in the model parameters as long as a device is connected to a web browser.

An example code is given below:

```
USE DISLIN
implicit real*8(a-h,o-z)
parameter(nx=200,ny=200,nz=1)
integer i,k,p,ntime1
integer cellnumx, cellnumy, nstep1
dimension u(0:nx+1,0:ny+1)
dimension ut(0:nx+1,0:ny+1)
dimension h(0:nx+1,0:ny+1)
cellnumx=100
cellnumy=100
ena=50d+0
gna=3d+0
duf=0.076656d+0*5d+0
xamp=200d+0
xtime=0.4d+0
uinitial = -84d+0
hinitial= 1d+0
dt=0.01d+0
```

```

dx=.02d+0
dx2=dx**2
dif=0.001d+0
time1=1000000d+0
period=99.3d+0
nstep1=time1/dt
!$acc data copyin(u,ut,h)
!$acc kernels
! closed do loop
do k=0,ny+1
do i=0,nx+1
u(i,k)=uinitial
ut(i,k)=uinitial
h(i,k)=hinitial
enddo
enddo

!$acc end kernels

t=0d+0
do ntime1=0,nstep1
pacet=dmod(t,period)
xistim=xamp*exp(-(pacet-0.3d+0)**2d+0/
(2d+0*0.05d+0**2d+0))
!$acc kernels
do i=0,nx
u(i,ny+1)=u(i,ny-1)
u(i,0)=u(i,2)
enddo

```

```

do k=0,ny
u(nx+1,k)=u(nx-1,k)
u(0,k)=u(2,k)
enddo

!$acc end kernels

!$acc kernels!parallel loop

! closed do loop

do k=1,ny
do i=1,nx
ah = (0.126d+0 *exp((-0.25d+0 )*(u(i,k)+77d+0 )))
bh = 1.7d+0 /(exp((-0.082d+0)*(u(i,k)+22.5d+0 ))+1d+0)
ssh = (ah/(ah+bh))
ssm=1d+0-exp(-0.07d+0*(u(i,k)+84d+0))
if(u(i,k).le.(-15d+0) )then
tauh=60d+0*exp(-(u(i,k)+62.5d+0)**2d+0/
(2d+0*7d+0**2d+0) ) + 0.7d+0
else
tauh1=0.7d+0
tauh2n=3.8d+0
tauh2=tauh2n/(1d+0+exp(-1d+0*(u(i,k)-10d+0)))
tauh=tauh1+tauh2
endif
xina = (gna*(ssm**3d+0)*h(i,k))*(u(i,k)-ena)
dh = duf*(ssh-h(i,k))/tauh
h(i,k)=h(i,k)+dh*dt
gk=5d0
if(u(i,k).ge.(-82d+0))then

```

```

xik = gk
else
xik = (gk/2d+0)*u(i,k)+(gk/2d+0)*84d+0
endif
xlap=(u(i+1,k)+u(i-1,k)+u(i,k-1)+
u(i,k+1)-4d+0*u(i,k))/dx2
if((i.ge.0).and.(i.le.10).and.(k.ge.0).and.(k.le.10))then
du= duf*(-xina-xik+xistim+dif*xlap)
else
du= duf*(-xina-xik+dif*xlap)
endif
ut(i,k)=u(i,k)+du*dt
enddo
enddo
!$acc end kernels
t=t+dt
!$acc kernels
! closed do loop
do k=1,ny
do i=1,nx
u(i,k)=ut(i,k)
enddo
enddo
! closed do loop
!$acc end kernels
if(mod(ntime1,100).eq.0)then
! update cpu

```

```

!$acc update host(u(1:nx,1:ny),h(1:nx,1:ny))
write(1000,*)t,u(cellnumx,cellnumy),
h(cellnumx,cellnumy)
! Dislin plotting
CALL METAFL('GL')
CALL DISINI()
CALL PAGERA()
!CALL HWFONT()
CALL TITLIN('2-D model',2)
!CALL TITLIN('F(X,Y) = 2 * SIN(X) * SIN(Y)',4)
!CALL NAME('X-axis','X')
!CALL NAME('Y-axis','Y')
CALL NAME('Voltage','Z')
CALL INTAX()
CALL AUTRES(nx,ny)
CALL AXSPOS(600,1850)
CALL AX3LEN(1500,1500,1500)
CALL GRAF3(0.,REAL(nx),0.,100.,1.,REAL(ny),0.,140.
,-90.,50.,-80.,10.)
CALL CRVMAT(real(u),nx+2,ny+2,1,1)
CALL HEIGHT(50)
CALL TITLE()
CALL ENDGRF()
CALL ERASE()

endif
enddo

```

!\$acc end data

end

APPENDIX C

POINCARÉ SECTION ANALYSIS

In chapter 4, we use a poincaré section analysis to find the periodic orbits existing in the system. Time is periodic since the stimulus paces the system periodically, so we use the section time = 10ms.

The periodic orbit is a fixed point on the section and satisfies

$$x^* = F(x^*) \tag{C.1}$$

or

$$0 = F(x^*) - x^* = P(x^*) \tag{C.2}$$

To find the periodic orbit, we use a newton solver on the equation equaling 0 above, to solve for x^* , or in our case \vec{x}^* is a vector consisting of v^* and h^* .

I estimate the general location of the periodic orbit and sample three points on the section near this general location. The first point is a chosen estimate point. The second and third points are separately deviated from the first point by δv and δh respectively. The values for δv and δh are generally order of 10^{-7} . I integrate the 3 fixed points forwards in time till the section is crossed and record the crossing values on the poincaré section. Let us denote the initial points as $\vec{x}_1, \vec{x}_2, \vec{x}_3$, and their crossing after integration as $F(\vec{x}^1), F(\vec{x}^2), F(\vec{x}^3)$. Depending on the periodic orbit, some orbits repeat after multiple crossings of the section.

Now, since the 3 points are in the neighborhood of the periodic orbit, they can be approximated as $x^* + \vec{dx}$ and the points satisfies

$$P(x^* + \vec{dx}) = P(x^*) + \frac{dP}{dx}\vec{dx}|_{x^*} \quad (\text{C.3})$$

$$P(x^* + \vec{dx}) = 0 + \frac{dP}{dx}\vec{dx}|_{x^*} \quad (\text{C.4})$$

Now, I select \vec{x}^1 and designate that as $x^* + \vec{dx}$. To solve for the \vec{dx} correction, which is composed of corrections on v and h , we find the matrix $\frac{dP}{dx}\vec{dx}|_{x^*}$, which we will name A , by calculating:

$$A = \left(\frac{P_2 - P_1}{\delta v} \middle| \frac{P_3 - P_1}{\delta h} \right) \quad (\text{C.5})$$

Now, the newton equation for the first point is:

$$P(x^1) = 0 + A\vec{dx} \quad (\text{C.6})$$

If we multiply both sides by the inverse of A , we can solve for .

$$A^{-1}P(x^1) = \vec{dx} \quad (\text{C.7})$$

This , which is composed of dv and dh , can be used to correct the guess.

APPENDIX D

CHAPTER 5: CALCIUM MODEL PARAMETERS

D.1 alternans from Q

$$\begin{aligned}
 \frac{dc_{cyto}}{dt} &= I_{rel} - I_{up} \\
 \frac{dc_{sr}}{dt} &= -I_{rel} + I_{up} \\
 I_{rel} &= g_{rel} n C_{sr} \\
 \frac{dn}{dt} &= \frac{n_{\infty} - n}{\tau_n} \\
 n_{\infty} &= r \frac{a_n}{a_n + b_n} \\
 \tau_n &= \frac{1}{a_n + b_n} \\
 a_n &= c_{an} I_{ca} q \\
 q_{\infty} &= \begin{cases} 0, & C_{sr} \leq 0.1 \\ 0.6(C_{sr} - 0.1), & C_{sr} \leq 0.8, C_{sr} > 0.1 \\ 7C_{sr} - 5.18, & \text{otherwise} \end{cases} \quad (D.1) \\
 \frac{dq}{dt} &= \frac{q_{\infty} - q}{\tau_q} \\
 r_{\infty} &= \frac{1}{1 + e^{\frac{-C_{sr} + 0.6}{0.01}}} \\
 \tau_r &= \begin{cases} \tau_{r1}, & C_{sr} \leq 0.7 \\ \tau_{r2}, & \text{otherwise} \end{cases} \\
 \frac{dr}{dt} &= \frac{r_{\infty} - r}{\tau_r} \\
 I_{up} &= \frac{c_{up} C_{cyto}^2}{C_{cyto}^2 + 0.001}
 \end{aligned}$$

$$\begin{aligned}
I_{ca} &= g_{ca} d_{\infty} f V \\
d_{\infty} &= \frac{1}{1 + e^{\frac{-V-20}{6.24}}} \\
f_{\infty} &= \frac{1}{1 + e^{\frac{V+40}{8.6}}} \\
\frac{df}{dt} &= \frac{f_{\infty} - f}{30}
\end{aligned}
\tag{D.2}$$

G_{rel}	0.45	c_{up}	0.0025
m_{ca}	-0.4	b_{ca}	13
g_{ca}	-160	c_{an}	0.0001
τ_q	50	τ_{r1}/τ_{r2}	10

D.2 alternans from R

$$\begin{aligned}
\frac{dc_{cyto}}{dt} &= I_{rel} - I_{up} \\
\frac{dc_{sr}}{dt} &= -I_{rel} + I_{up} \\
I_{rel} &= g_{rel} n C_{sr} \\
\frac{dn}{dt} &= \frac{n_{\infty} - n}{\tau_n} \\
n_{\infty} &= r \frac{a_n}{a_n + b_n} \\
\tau_n &= \frac{1}{a_n + b_n} \\
a_n &= c_{an} I_{ca} q \\
q_{\infty} &= 1.3 C_{sr} \\
\frac{dq}{dt} &= \frac{q_{\infty} - q}{\tau_q} \\
r_{\infty} &= \frac{1}{1 + e^{\frac{-C_{sr} + 0.95}{0.01}}} \\
\tau_r &= \begin{cases} \tau_{r1}, & C_{sr} \leq 0.7 \\ \tau_{r2}, & \text{otherwise} \end{cases} \\
\frac{dr}{dt} &= \frac{r_{\infty} - r}{\tau_r} \\
I_{up} &= \frac{c_{up} C_{cyto}^2}{C_{cyto}^2 + 0.001}
\end{aligned} \tag{D.3}$$

$$\begin{aligned}
I_{ca} &= g_{ca} d_{\infty} f V \\
d_{\infty} &= \frac{1}{1 + e^{\frac{-V - 20}{6.24}}} \\
f_{\infty} &= \frac{1}{1 + e^{\frac{V + 40}{8.6}}} \\
\frac{df}{dt} &= \frac{f_{\infty} - f}{30}
\end{aligned} \tag{D.4}$$

G_{rel}	0.45	c_{up}	0.0025
m_{ca}	-0.4	b_{ca}	13
g_{ca}	-160	c_{an}	0.0001
τ_q	50	τ_{r1}/τ_{r2}	50

D.3 alternans for cat atrium

Our voltage model is phenomenologically at the order of 1. Therefore, to fit to realistic values, we scale the voltage. We will denote the unscaled voltage as V and scaled voltage as v . The scaled v is used in the calcium model.

$$\begin{aligned}
\frac{\partial V}{\partial t} &= D \frac{\partial^2 V}{\partial x^2} - I_{na} - I_k - c_1 I_{ca} - c_2 I_{naca} \\
I_{Na} &= \begin{cases} -h(V - V_C)(1 - V)/\tau_{Na}, & V \geq V_C \text{mV} \\ 0, & \text{otherwise} \end{cases} \\
v &= V * 100 - 84 \\
I_K &= \begin{cases} 1/\tau_{K1}, & V \geq V_C \text{mV} \\ V/\tau_{K2}, & \text{otherwise} \end{cases} \\
\tau_h^- &= \begin{cases} \tau_{h1}^-, & V \leq V_h \text{mV} \\ \tau_{h2}^-, & \text{otherwise} \end{cases} \\
\frac{dh}{dt} &= \begin{cases} -h/\tau_h^+, & V \geq V_C \text{mV} \\ (1 - h)/\tau_h^-, & \text{otherwise} \end{cases}
\end{aligned} \tag{D.5}$$

τ_{NA}	0.6729	D	0.001
T_{k1}	405	T_{k2}	241
T_{h1}^-	40	T_{h1}^-	40
T_h^+	3.5	c_1	0.000007
c_2	0.0056		

$$\begin{aligned}
\frac{dc_{cyto}}{dt} &= I_{rel} - I_{up} + c_3 I_{ca} + c_4 I_{naca} \\
\frac{dc_{sr}}{dt} &= -I_{rel} + I_{up} \\
I_{rel} &= g_{rel} n C_{sr} \\
\frac{dn}{dt} &= \frac{n_{\infty} - n}{\tau_n} \\
n_{\infty} &= r \frac{a_n}{a_n + b_n} \\
\tau_n &= \frac{1}{a_n + b_n} \\
a_n &= c_{an} I_{ca} q \\
q_{\infty} &= \begin{cases} 0, & C_{sr} \leq 0.3 \\ 0.6(C_{sr} - 0.3), & C_{sr} \leq 0.8, C_{sr} > 0.3 \\ 5C_{sr} - 3.7, & \text{otherwise} \end{cases} \tag{D.6} \\
\frac{dq}{dt} &= \frac{q_{\infty} - q}{\tau_q} \\
r_{\infty} &= \frac{1}{1 + e^{\frac{-C_{sr} + 0.97}{0.01}}} \\
\frac{dr}{dt} &= \frac{r_{\infty} - r}{\tau_r} \\
I_{up} &= \frac{c_{up} C_{cyto}^2}{C_{cyto}^2 + 0.001}
\end{aligned}$$

$$\begin{aligned}
I_{naca} &= C_{naca}(m_{ncx}v + b_{ncx})C_{cyto}(e^{(v-E_{naca})k} - 1) \\
E_{naca} &= \log\left(\frac{Na_o^3 C_{cyto}}{Na_i^3 C_{ao}}\right) \\
I_{ca} &= g_{ca}d_{\infty}f(-0.4v + 13) \\
d_{\infty} &= \frac{1}{1 + e^{\frac{-v-20}{6.24}}} \\
f_{\infty} &= \frac{1}{1 + e^{\frac{v+40}{8.6}}}
\end{aligned} \tag{D.7}$$

G_{rel}	1.2	c_{up}	0.0018
c_3	-0.000008	c_4	0.004
c_{an}	0.0001	τ_q	30
C_{naca}	0.1	τ_r	50
b_{ncx}	0.83636	m_{ncx}	-0.02182
Na_o	140000	Na_i	10000
Ca_o	1800	g_{ca}	-40
k	1/26		

D.4 alternans rabbit ventricles

Our voltage model is phenomenologically at the order of 1. Therefore, to fit to realistic values, we scale the voltage. We will denote the unscaled voltage as V and scaled voltage

as v . The scaled v is used in the calcium model.

$$\begin{aligned}
\frac{\partial V}{\partial t} &= D \frac{\partial^2 V}{\partial x^2} - I_{na} - I_k - c_1 I_{ca} - c_2 I_{naca} \\
I_{Na} &= \begin{cases} -h(V - V_C)(1 - V)/\tau_{Na}, & V \geq V_C \text{ mV} \\ 0, & \text{otherwise} \end{cases} \\
v &= V * 100 - 84 \\
I_K &= \begin{cases} 1/\tau_{K1}, & V \geq V_C \text{ mV} \\ V/\tau_{K2}, & \text{otherwise} \end{cases} \\
\tau_h^- &= \begin{cases} \tau_{h1}^-, & V \leq V_h \text{ mV} \\ \tau_{h2}^-, & \text{otherwise} \end{cases} \\
\frac{dh}{dt} &= \begin{cases} -h/\tau_h^+, & V \geq V_C \text{ mV} \\ (1 - h)/\tau_h^-, & \text{otherwise} \end{cases}
\end{aligned} \tag{D.8}$$

τ_{NA}	0.6729	D	0.001
T_{k1}	405	T_{k2}	241
T_{h1}^-	40	T_{h1}^-	40
T_h^+	3.5	c_1	0.000007
c_2	0.0056		

$$\begin{aligned}
\frac{dc_{cyto}}{dt} &= I_{rel} - I_{up} + c_3 I_{ca} + c_4 I_{naca} \\
\frac{dc_{sr}}{dt} &= -I_{rel} + I_{up} \\
I_{rel} &= g_{rel} n C_{sr} \\
\frac{dn}{dt} &= \frac{n_{\infty} - n}{\tau_n} \\
n_{\infty} &= r \frac{a_n}{a_n + b_n} \\
\tau_n &= \frac{1}{a_n + b_n} \\
a_n &= c_{an} I_{ca} q \\
q_{\infty} &= \begin{cases} 0, & C_{sr} \leq 0.3 \\ 0.6(C_{sr} - 0.3), & C_{sr} \leq 0.8, C_{sr} > 0.3 \\ 5C_{sr} - 3.7, & \text{otherwise} \end{cases} \tag{D.9} \\
\frac{dq}{dt} &= \frac{q_{\infty} - q}{\tau_q} \\
r_{\infty} &= \frac{1}{1 + e^{\frac{-C_{sr} + 0.7}{0.01}}} \\
\frac{dr}{dt} &= \frac{r_{\infty} - r}{\tau_r} \\
I_{up} &= \frac{c_{up} C_{cyto}^2}{C_{cyto}^2 + 0.001}
\end{aligned}$$

$$\begin{aligned}
I_{naca} &= C_{naca}(m_{ncx}v + b_{ncx})C_{cyto}(e^{(v-E_{naca})k} - 1) \\
E_{naca} &= \log\left(\frac{Na o^3 C_{cyto}}{Nai^3 C_{ao}}\right) \\
I_{ca} &= g_{ca}d_{\infty}fv \\
d_{\infty} &= \frac{1}{1 + e^{\frac{-v-20}{6.24}}} \\
f_{\infty} &= \frac{1}{1 + e^{\frac{v+40}{8.6}}}
\end{aligned} \tag{D.10}$$

G_{rel}	1.2	c_{up}	0.0017
c_3	-0.000008	c_4	0.004
c_{an}	0.0001	τ_q	30
C_{naca}	0.1	τ_r	100
b_{ncx}	0.83636	m_{ncx}	-0.02182
$Na o$	140000	Nai	10000
C_{ao}	1800	g_{ca}	-40
k	1/26		

REFERENCES

- [1] A. J. Moss, W. Zareba, W. J. Hall, H. Klein, D. J. Wilber, D. S. Cannom, J. P. Daubert, S. L. Higgins, M. W. Brown, and M. L. Andrews, "Prophylactic implantation of a defibrillator in patients with myocardial infarction and reduced ejection fraction," *New England Journal of Medicine*, vol. 346, no. 12, pp. 877–883, 2002.
- [2] R. J. Myerburg, K. M. Kessler, and A. Castellanos, "Sudden cardiac death. structure, function, and time-dependence of risk.," *Circulation*, vol. 85, no. 1 Suppl, pp. I2–10, 1992.
- [3] J. Jalife, "Ventricular fibrillation: Mechanisms of initiation and maintenance," *Annual review of physiology*, vol. 62, no. 1, pp. 25–50, 2000.
- [4] D. L. Mann, D. P. Zipes, P. Libby, and R. O. Bonow, *Braunwald's heart disease e-book: A textbook of cardiovascular medicine*. Elsevier Health Sciences, 2014.
- [5] Y. Li, H. Barajas-Martinez, B. Li, Y. Gao, Z. Zhang, H. Shang, Y. Xing, and D. Hu, "Comparative effectiveness of acupuncture and antiarrhythmic drugs for the prevention of cardiac arrhythmias: A systematic review and meta-analysis of randomized controlled trials," *Frontiers in physiology*, vol. 8, p. 358, 2017.
- [6] M. Bohnen, W. G. Stevenson, U. B. Tedrow, G. F. Michaud, R. M. John, L. M. Epstein, C. M. Albert, and B. A. Koplan, "Incidence and predictors of major complications from contemporary catheter ablation to treat cardiac arrhythmias," *Heart Rhythm*, vol. 8, no. 11, pp. 1661–1666, 2011.
- [7] *Anatomy and function of the electrical system*, <https://www.stanfordchildrens.org/en/topic/default?id=anatomy-and-function-of-the-electrical-system-90-P01762>, (Accessed on 03/14/2019).
- [8] J.-B. Kim, "Channelopathies," *Korean journal of pediatrics*, vol. 57, no. 1, p. 1, 2014.
- [9] L. F. Santana, E. P. Cheng, and W. J. Lederer, "How does the shape of the cardiac action potential control calcium signaling and contraction in the heart?" *Journal of molecular and cellular cardiology*, vol. 49, no. 6, p. 901, 2010.
- [10] N. J. Severs, "The cardiac muscle cell," *Bioessays*, vol. 22, no. 2, pp. 188–199, 2000.
- [11] H.-T. Shih, "Anatomy of the action potential in the heart.," *Texas Heart Institute Journal*, vol. 21, no. 1, p. 30, 1994.

- [12] D. M. Bers, “Calcium cycling and signaling in cardiac myocytes,” *Annu. Rev. Physiol.*, vol. 70, pp. 23–49, 2008.
- [13] M. S. Martínez, A. García, E. Luzardo, M. Chávez-Castillo, L. C. Olivar, J. Salazar, M. Velasco, J. J. R. Quintero, and V. Bermúdez, “Energetic metabolism in cardiomyocytes: Molecular basis of heart ischemia and arrhythmogenesis,” *Vessel Plus*, vol. 1, pp. 230–41, 2017.
- [14] D. A. Goodenough and D. L. Paul, “Gap junctions,” *Cold Spring Harbor perspectives in biology*, vol. 1, no. 1, a002576, 2009.
- [15] F. H. Fenton and E. M. Cherry, “Models of cardiac cell,” *Scholarpedia*, vol. 3, no. 8, p. 1868, 2008.
- [16] J. J. B. Jack, D. Noble, and R. W. Tsien, “Electric current flow in excitable cells,” 1975.
- [17] D. Bers, *Excitation-contraction coupling and cardiac contractile force*. Springer Science & Business Media, 2001, vol. 237.
- [18] W. Thomson, “Iii. on the theory of the electric telegraph,” *Proceedings of the Royal Society of London*, no. 7, pp. 382–399, 1856.
- [19] C. Antzelevitch and A. Burashnikov, “Overview of basic mechanisms of cardiac arrhythmia,” *Cardiac electrophysiology clinics*, vol. 3, no. 1, pp. 23–45, 2011.
- [20] J. N. Weiss, A. Garfinkel, H. S. Karagueuzian, P.-S. Chen, and Z. Qu, “Early afterdepolarizations and cardiac arrhythmias,” *Heart rhythm*, vol. 7, no. 12, pp. 1891–1899, 2010.
- [21] D. X. Tran, D. Sato, A. Yochelis, J. N. Weiss, A. Garfinkel, and Z. Qu, “Bifurcation and chaos in a model of cardiac early afterdepolarizations,” *Physical review letters*, vol. 102, no. 25, p. 258 103, 2009.
- [22] G. Tse, “Mechanisms of cardiac arrhythmias,” *Journal of arrhythmia*, vol. 32, no. 2, pp. 75–81, 2016.
- [23] L. G. Flavio Fenton Elizabeth Cherry, *Cardiac arrhythmia - scholarpedia*, http://www.scholarpedia.org/article/Cardiac_arrhythmia, (Accessed on 03/11/2019).
- [24] G Bub, “G. bub, a. shrier, and l. glass, phys. rev. lett. 88, 058101 (2002).,” *Phys. Rev. Lett.*, vol. 88, p. 058 101, 2002.

- [25] R. Gray, “Ra gray, am pertsov, and j. jalife, nature (london) 392, 75 (1998).,” *Nature (London)*, vol. 392, p. 75, 1998.
- [26] E. M. Cherry and F. H. Fenton, “Visualization of spiral and scroll waves in simulated and experimental cardiac tissue,” *New Journal of Physics*, vol. 10, no. 12, p. 125 016, 2008.
- [27] R. A. Gray, J. Jalife, A. V. Panfilov, W. T. Baxter, C. Cabo, J. M. Davidenko, A. M. Pertsov, P. Hogeweg, and A. T. Winfree, “Mechanisms of cardiac fibrillation,” *Science*, vol. 270, no. 5239, pp. 1222–1226, 1995.
- [28] P. H. Specialists, *Wolff parkinson white syndrome - pediatric heart specialists*.
- [29] J. Nolasco and R. W. Dahlen, “A graphic method for the study of alternation in cardiac action potentials,” *J Appl Physiol*, vol. 25, no. 2, pp. 191–196, 1968.
- [30] M. Guevara, G Ward, A Shrier, and L Glass, “Electrical alternans and period doubling bifurcations,” *IEEE Comp. Cardiol*, vol. 562, pp. 167–170, 1984.
- [31] J. M. Pastore, S. D. Girouard, K. R. Laurita, F. G. Akar, and D. S. Rosenbaum, “Mechanism linking t-wave alternans to the genesis of cardiac fibrillation,” *Circulation*, vol. 99, no. 10, pp. 1385–1394, 1999.
- [32] Z. Qu, Y. Xie, A. Garfinkel, and J. N. Weiss, “T-wave alternans and arrhythmogenesis in cardiac diseases,” *Frontiers in physiology*, vol. 1, p. 154, 2010.
- [33] J. N. Weiss, A. Karma, Y. Shiferaw, P.-S. Chen, A. Garfinkel, and Z. Qu, “From pulsus to pulseless: The saga of cardiac alternans,” *Circulation research*, vol. 98, no. 10, pp. 1244–1253, 2006.
- [34] M. A. Watanabe, F. H. Fenton, S. J. Evans, H. M. Hastings, and A. Karma, “Mechanisms for discordant alternans,” *Journal of cardiovascular electrophysiology*, vol. 12, no. 2, pp. 196–206, 2001.
- [35] K. Ten Tusscher, D. Noble, P.-J. Noble, and A. V. Panfilov, “A model for human ventricular tissue,” *American Journal of Physiology-Heart and Circulatory Physiology*, 2004.
- [36] T. O’Hara, L. Virág, A. Varró, and Y. Rudy, “Simulation of the undiseased human cardiac ventricular action potential: Model formulation and experimental validation,” *PLoS computational biology*, vol. 7, no. 5, e1002061, 2011.
- [37] D. Noble, “A modification of the hodgkinhuxley equations applicable to purkinje fibre action and pacemaker potentials,” *The Journal of physiology*, vol. 160, no. 2, pp. 317–352, 1962.

- [38] J. Nagumo, S. Arimoto, and S. Yoshizawa, "An active pulse transmission line simulating nerve axon," *Proceedings of the IRE*, vol. 50, no. 10, pp. 2061–2070, 1962.
- [39] Y. Shiferaw and A. Karma, "Turing instability mediated by voltage and calcium diffusion in paced cardiac cells," *Proceedings of the National Academy of Sciences*, vol. 103, no. 15, pp. 5670–5675, 2006.
- [40] D. D. Chen, R. A. Gray, I. Uzelac, C. Herndon, and F. H. Fenton, "Mechanism for amplitude alternans in electrocardiograms and the initiation of spatiotemporal chaos," *Physical review letters*, vol. 118, no. 16, p. 168 101, 2017.
- [41] R. C. Myles, F. L. Burton, S. M. Cobbe, and G. L. Smith, "Alternans of action potential duration and amplitude in rabbits with left ventricular dysfunction following myocardial infarction," *Journal of molecular and cellular cardiology*, vol. 50, no. 3, pp. 510–521, 2011.
- [42] V. Y. Sidorov, I. Uzelac, and J. P. Wikswo, "Regional increase of extracellular potassium leads to electrical instability and reentry occurrence through the spatial heterogeneity of apd restitution," *American Journal of Physiology-Heart and Circulatory Physiology*, 2011.
- [43] E. Cherry, "Em cherry and fh fenton, am. j. physiol. heart circ. physiol. 286, h2332 (2004).," *Am. J. Physiol. Heart Circ. Physiol.*, vol. 286, H2332, 2004.
- [44] E. Tolkacheva, D. Schaeffer, D. J. Gauthier, and W. Krassowska, "Condition for alternans and stability of the 1: 1 response pattern in a memoryi model of paced cardiac dynamics," *Physical review E*, vol. 67, no. 3, p. 031 904, 2003.
- [45] M. E. Díaz, S. C. O'Neill, and D. A. Eisner, "Sarcoplasmic reticulum calcium content fluctuation is the key to cardiac alternans," *Circulation research*, vol. 94, no. 5, pp. 650–656, 2004.
- [46] S. M. Narayan, D. E. Krummen, K. Shivkumar, P. Clopton, W.-J. Rappel, and J. M. Miller, "Treatment of atrial fibrillation by the ablation of localized sources: Confirm (conventional ablation for atrial fibrillation with or without focal impulse and rotor modulation) trial," *Journal of the American College of Cardiology*, vol. 60, no. 7, pp. 628–636, 2012.
- [47] G. W. Beeler and H. Reuter, "Reconstruction of the action potential of ventricular myocardial fibres," *The Journal of physiology*, vol. 268, no. 1, pp. 177–210, 1977.
- [48] A. Hodgkin and A. Huxley, "Propagation of electrical signals along giant nerve fibres," *Proceedings of the Royal Society of London. Series B, Biological Sciences*, pp. 177–183, 1952.

- [49] F. H. Fenton and E. M. Cherry, *Models of cardiac cell*.
- [50] D. D. Chen, R. A. Gray, and F. H. Fenton, "Modelling the take-off voltage of the action potential during fast pacing," in *Computing in Cardiology 2014*, IEEE, 2014, pp. 685–688.
- [51] X. Zhou, P. Guse, P. Wolf, D. L. Rollins, W. M. Smith, and R. E. Ideker, "Existence of both fast and slow channel activity during the early stages of ventricular fibrillation.," *Circulation research*, vol. 70, no. 4, pp. 773–786, 1992.
- [52] F. H. Fenton, S. Luther, E. M. Cherry, N. F. Otani, V. Krinsky, A. Pumir, E. Boddenschatz, and R. F. Gilmour Jr, "Termination of atrial fibrillation using pulsed low-energy far-field stimulation," *Circulation*, vol. 120, no. 6, p. 467, 2009.
- [53] C.-h. Luo and Y. Rudy, "A model of the ventricular cardiac action potential. depolarization, repolarization, and their interaction.," *Circulation research*, vol. 68, no. 6, pp. 1501–1526, 1991.
- [54] F. H. Fenton, E. M. Cherry, and L. Glass, "Cardiac arrhythmia," *Scholarpedia*, vol. 3, no. 7, p. 1665, 2008, revision #121399.
- [55] J. M. Davidenko, A. V. Pertsov, R. Salomonsz, W. Baxter, and J. Jalife, "Stationary and drifting spiral waves of excitation in isolated cardiac muscle," *Nature*, vol. 355, no. 6358, p. 349, 1992.
- [56] A. L. Hodgkin and A. F. Huxley, "Currents carried by sodium and potassium ions through the membrane of the giant axon of loligo," *The Journal of physiology*, vol. 116, no. 4, pp. 449–472, 1952.
- [57] P. Gray, "P. gray and sk scott, chem. eng. sci. 39, 1087 (1984).," *Chem. Eng. Sci.*, vol. 39, p. 1087, 1984.
- [58] R. FitzHugh, "Mathematical models of threshold phenomena in the nerve membrane," *The bulletin of mathematical biophysics*, vol. 17, no. 4, pp. 257–278, 1955.
- [59] J. E. Pearson, "Complex patterns in a simple system," *Science*, vol. 261, no. 5118, pp. 189–192, 1993.
- [60] R. A. Gray and D. J. Huelsing, "Excito-oscillatory dynamics as a mechanism of ventricular fibrillation," *Heart Rhythm*, vol. 5, no. 4, pp. 575–584, 2008.
- [61] E. N. Cytrynbaum and T. J. Lewis, "A global bifurcation and the appearance of a one-dimensional spiral wave in excitable media," *SIAM Journal on Applied Dynamical Systems*, vol. 8, no. 1, pp. 348–370, 2009.

- [62] M. Nivala, E. de Lange, R. Rovetti, and Z. Qu, “Computational modeling and numerical methods for spatiotemporal calcium cycling in ventricular myocytes,” *Front Physiol*, vol. 3, p. 114, 2012.
- [63] E Chudin, J Goldhaber, A Garfinkel, J Weiss, and B Kogan, “Intracellular ca^{2+} dynamics and the stability of ventricular tachycardia,” *Biophysical journal*, vol. 77, no. 6, pp. 2930–2941, 1999.
- [64] J. N. Edwards and L. A. Blatter, “Cardiac alternans and intracellular calcium cycling,” *Clinical and Experimental Pharmacology and Physiology*, vol. 41, no. 7, pp. 524–532, 2014.
- [65] Y Shiferaw, M. Watanabe, A Garfinkel, J. Weiss, and A Karma, “Model of intracellular calcium cycling in ventricular myocytes,” *Biophysical journal*, vol. 85, no. 6, pp. 3666–3686, 2003.
- [66] G. Meissner, “Ryanodine receptor/ ca^{2+} release channels and their regulation by endogenous effectors,” *Annual review of physiology*, vol. 56, no. 1, pp. 485–508, 1994.
- [67] S.-Q. Wang, L.-S. Song, E. G. Lakatta, and H. Cheng, “Ca 2^{+} signalling between single l-type ca^{2+} channels and ryanodine receptors in heart cells,” *Nature*, vol. 410, no. 6828, p. 592, 2001.
- [68] A. Fabiato, “Time and calcium dependence of activation and inactivation of calcium-induced release of calcium from the sarcoplasmic reticulum of a skinned canine cardiac purkinje cell,” *The Journal of general physiology*, vol. 85, no. 2, pp. 247–289, 1985.
- [69] G. Ruiz-Hurtado, L. Li, M. Fernández-Velasco, A. Rueda, F. Lefebvre, Y. Wang, P. Mateo, C. Cassan, B. Gellen, J. P. Benitah, *et al.*, “Reconciling depressed ca^{2+} sparks occurrence with enhanced ryr2 activity in failing mice cardiomyocytes,” *The Journal of general physiology*, vol. 146, no. 4, pp. 295–306, 2015.
- [70] Z. Qu, M. B. Liu, and M. Nivala, “A unified theory of calcium alternans in ventricular myocytes,” *Scientific reports*, vol. 6, p. 35 625, 2016.
- [71] M. D. Stern, L.-S. Song, H. Cheng, J. S. Sham, H. T. Yang, K. R. Boheler, and E. Ríos, “Local control models of cardiac excitation–contraction coupling a possible role for allosteric interactions between ryanodine receptors,” *The Journal of general physiology*, vol. 113, no. 3, pp. 469–489, 1999.
- [72] M. D. Stern, “Theory of excitation-contraction coupling in cardiac muscle,” *Biophysical journal*, vol. 63, no. 2, pp. 497–517, 1992.

- [73] Z. Qu, M. Nivala, and J. N. Weiss, "Calcium alternans in cardiac myocytes: Order from disorder," *Journal of molecular and cellular cardiology*, vol. 58, pp. 100–109, 2013.
- [74] I. Györke and S. Györke, "Regulation of the cardiac ryanodine receptor channel by luminal Ca^{2+} involves luminal Ca^{2+} sensing sites," *Biophysical journal*, vol. 75, no. 6, pp. 2801–2810, 1998.
- [75] D. Terentyev, S. Viatchenko-Karpinski, H. H. Valdivia, A. L. Escobar, and S. Györke, "Luminal Ca^{2+} controls termination and refractory behavior of Ca^{2+} -induced Ca^{2+} release in cardiac myocytes," *Circulation research*, vol. 91, no. 5, pp. 414–420, 2002.
- [76] M. Díaz, "Me díaz, sc oneill, and da eisner, circ. res. 94, 650 (2004).," *Circ. Res.*, vol. 94, p. 650, 2004.
- [77] J. Bassani, W. Yuan, and D. M. Bers, "Fractional sr Ca release is regulated by trigger Ca and sr Ca content in cardiac myocytes," *American Journal of Physiology-Cell Physiology*, vol. 268, no. 5, pp. C1313–C1319, 1995.
- [78] V. M. Shkryl, J. T. Maxwell, T. L. Domeier, and L. A. Blatter, "Refractoriness of sarcoplasmic reticulum Ca release determines Ca alternans in atrial myocytes," *American Journal of Physiology-Heart and Circulatory Physiology*, 2012.
- [79] Y. Shiferaw, Z. Qu, A. Garfinkel, A. Karma, and J. N. Weiss, "Nonlinear dynamics of paced cardiac cells," *Annals of the New York Academy of Sciences*, vol. 1080, no. 1, pp. 376–394, 2006.
- [80] C.-h. Luo and Y. Rudy, "A dynamic model of the cardiac ventricular action potential. i. simulations of ionic currents and concentration changes.," *Circulation research*, vol. 74, no. 6, pp. 1071–1096, 1994.
- [81] L. Cleemann, W. Wang, and M. Morad, "Two-dimensional confocal images of organization, density, and gating of focal Ca^{2+} release sites in rat cardiac myocytes," *Proceedings of the National Academy of Sciences*, vol. 95, no. 18, pp. 10 984–10 989, 1998.